TRANSIENT THERMAL RESPONSE OF HEAVY VEHICLE WHEEL ASSEMBLIES TO FRICTION BRAKING

Joshua Subel

A dissertation submitted to the Faculty of Engineering and the Built Environment, of the University of the Witwatersrand, Johannesburg, in fulfilment of the requirements for the degree of Master of Science in Engineering.

Johannesburg 2018

Declaration

I declare that this dissertation is my own, unaided work, except where otherwise acknowledged. It is being submitted for the degree of Master of Science in Engineering in the University of the Witwatersrand, Johannesburg. It has not been submitted before for any degree or examination at any other university.

Signed this 11th day of October 2018

Joshua Subel

To Mom, Dad, David and Su,
for everything you have taught me.

Acknowledgements

I would like to thank Prof. Frank Kienhöfer for supervising this work, for his ongoing support and guidance and for his unwavering commitment to education. The impact his mentorship has had on me cannot be overstated.

I am grateful to the various sponsors who have enabled this work through generous contributions to Wits University. Thank you to Siemens Southern Africa for donating the motor and gearbox for the custom-built test rig; BPW South Africa for the single and dual axles and aluminium rims; CA Muller for the steel rims; CT Hydraulics, Fluid Power Group, Hydraulic Training and Consultants and Ax. Hydraulics for the hydraulic system, and SKF South Africa for the bearings. In particular I wish to acknowledge Mr. Kersten Grote of BPW South Africa for responding to technical queries, facilitating maintenance of the axles and arranging the donation of the dual, aluminium rims.

This research would not have been possible without the efforts of Mr. Shaun Riekert, Mr. Andrew Heydenrych and the rest of the Wits Mechanical Engineering Laboratory staff who helped to maintain, repair and improve the rolling road.

I would like to thank Mr. Jarren Lange for developing and implementing the control software used to remotely operate the rolling road and for his continued involvement in the betterment of the rig.

Thank you to Mr. Jordin Borer, Mr. Douglas van Niekerk, Mrs. Lorrainne Doherty and Mr. Karsten Haas for their support, guidance and indispensable friendship.

Abstract

Overheating brakes cause brake fade, tyre blowouts and vehicle fires, but no study has investigated the influence of wheel configuration or rim material on these catastrophic failures. Experimental, laboratory measurements of the transient thermal response of heavy vehicle wheel assemblies to $1\ kW - 4\ kW$ of alpine friction braking are presented; comparing brake and tyre temperature when using dual and single wheels with steel and aluminium rims. Lumped mass thermal models were developed and used to interpret the mechanisms by which $2.5\ kW$ of continuous braking heat is dissipated throughout the wheel assembly. The steady state temperature increase of the brake was $3.05\ °C$ (1.9%) higher when using steel versus aluminium rims. The increase in average tyre temperature at steady state was $7.35\ °C$ (30%) higher when using aluminium versus steel rims and $15.8\ °C$ (82%) higher when using single versus dual wheels. The greater thermal conductivity and cross-sectional area of the aluminium rims relative to the steel rims reduce the thermal resistance of braking heat flowing into the tyre; leading to higher tyre temperature when using aluminium rims. Dual rims and tyres have larger surface areas than singles which convect more heat to the air at lower temperatures; leading to cooler tyres when using dual wheels. These results indicate that the risk of tyres overheating, leading to blowout, from extended use of the brakes is increased when using single wheels compared to dual wheels and further exacerbated by using aluminium rims compared to steel rims. Model parameters were estimated for a conceptual carbon fibre reinforced polymer (CFRP)-rimmed wheel and the temperature response to $2.5\ kW$ of alpine braking calculated. The simulated brake temperatures on the CFRP-rimmed wheel were $67.7\ °C - 70.1\ °C$ higher than for the steel and aluminium rims. This is a consequence of the comparatively low thermal conductivity of CFRP, which necessitates that the brake dissipate an average of 42% more heat by convection. These results suggest that improved cooling of the brakes is required if CFRP rims are used on a heavy vehicle.

Contents

List of Figures

List of Tables

List of Symbols

A_1 Maximum temperature region of the tyre $(-)$.

A_2 Average temperature region of the rim $(-)$.

A_c Conductive cross-sectional area (m^2).

A_s Convective surface area (m^2).

C_p Specific heat $({}^{J}/_{kg\,\cdot\,{}^\circ C})$.

F View factor $(-)$.

L_1 Radial temperature line of the tyre $(-)$.

L_e Effective conductive length (m).

P_b Braking power (W).

Q Rate of heat transfer/generation/storage (W).

Q_{ss} Steady state inter-component heat transfer (W).

R Randomly generated real number between 0 and 1 $(-)$.

T Temperature $(^\circ C)$.

T_∞ Ambient temperature $(^\circ C)$.

T_{min} Minimum simulated annealing temperature $(^\circ C)$.

T_{peak} Maximum temperature response to isolated unit step input assuming zero initial conditions and zero ambient temperature $(^\circ C)$.

T_{sim} Simulated annealing temperature $(^\circ C)$.

U Overall heat transfer coefficient $({}^{W}/_{{}^\circ C})$.

V Volume $({}^{kg}/_{m^3})$.

W Fractional weighting factor $(-)$.

$X(s)$ Laplace transform of $X(t)$ $(-)$.

$X(t)$ X is a function of time (context-specific unit).

X_{ba} Thermal interaction between the beam and air (context-specific unit).

X_f Final value of X (context-specific unit).

X_i Initial value of X (context-specific unit).

X_{ra} Thermal interaction between the rim and air (context-specific unit).

X_{rt} Thermal interaction between the rim and tyre (context-specific unit).

X_{sa} Thermal interaction between the shoe and air (context-specific unit).

X_{sb} Thermal interaction between the shoe and beam (context-specific unit).

X_{sr} Thermal interaction between the shoe and rim (context-specific unit).

X_{ta} Thermal interaction between the tyre and air (context-specific unit).

ΔT_{ss} Steady state temperature increase ($^{\circ}C$).

ΔT_{xy} Temperature difference ($^{\circ}C$).

ΔX Change in X (context-specific unit).

$\dot{X}(t)$ The first derivative of X with respect to time (context-specific unit).

$\mathbf{A}$ Matrix of overall heat transfer coefficients ($^{W}/_{^{\circ}C}$).

$\mathbf{B}$ Matrix of thermal capacities ($^{J}/_{^{\circ}C}$).

$\mathbf{C}$ Vector of isolated unit step inputs (W).

$\mathbf{C}(t)$ Matrix of system inputs (W).

$\mathbf{D}$ System matrix (context-specific unit).

$\mathbf{E}$ Control matrix (context-specific unit).

$\mathbf{E}_{\%}$ Overall error matrix containing individual percentage error vectors (%).

$\mathbf{I}$ Identity matrix ($-$).

$\mathbf{P}$ Permutation matrix of weighting factors ($-$).

$\mathbf{T_{exp}}$ Vector of measured temperatures($^{\circ}C$).

$\mathbf{T_{mod}}$ Vector of modelled temperatures ($^{\circ}C$).

$\mathbf{T}(t)$ Matrix of component temperatures ($°C$).

$\dot{\mathbf{T}}(t)$ Matrix of component temperature gradients ($°C$).

$\mathbf{e}$ Vector of percentage errors (%).

$\mathbf{u}(t)$ Input vector (context-specific unit).

$\mathbf{x}(t)$ State vector (context-specific unit).

$\mathscr{L}$ Laplace transform operation ($-$).

$\overline{E}$ Average percentage *RMSE* (%).

$\overline{X}$ Average value of X (context-specific unit).

d Decay factor ($-$).

h Convective heat transfer coefficient ($^{w}/_{m^2 \cdot °C}$).

h_e Combined convective and radiative heat transfer coefficient ($^{w}/_{m^2 \cdot °C}$).

i Number of optimisation iterations ($-$).

k Thermal conductivity ($^{w}/_{m \cdot °C}$).

m Mass (kg).

t Time (S).

v Volume fraction (%).

ϵ Emissivity ($-$).

ρ Density ($^{kg}/_{m^3}$).

σ_r Stephan - Boltzmann constant ($\sigma = 5.68 \times 10^{-8}\ ^{W}/_{m \cdot K^4}$).

σ Standard deviation in percentage *RMSEs* (%).

Acronyms

RMSE root-mean-square error.

CFRP carbon fiber reinforced polymer.

CPU central processing unit.

CSM compact switching module.

DAQ data acquisition centre.

DCV directional control valve.

DoF degree-of-freedom.

FDM finite difference model.

FEA finite element analysis.

FEM finite element model.

GUI graphical user interface.

MCU motor control unit.

PCV proportional control valve.

PID proportional-integral-derivative.

PLC programmable logic controller.

PPR proportional pressure regulator.

VSD variable speed drive.

Glossary

Additivity The output of an additive system to the sum of multiple inputs is equal to the sum of the outputs to each of the individual inputs.

Alpine Braking Prolonged application of constant braking power to maintain a vehicle at a constant speed while descending a slope.

Bead Inner edge of the tyre which contacts the rim.

Brake Fade Decrease in braking power due to heightened temperature lowering the coefficient of friction of the brakes.

Cost Function The metric which must be minimised by an optimisation routine.

Discrete Temperature The temperature of an object measured at a single location.

Driving Power The power drawn by the motor to maintain the wheel at a constant velocity with or without braking.

Driving Power Setpoint The power drawn by the motor required to free-roll the wheel plus the desired braking power.

Dual Wheels A type of wheel configuration where two rims and tyres are mounted to a single axle (duals).

Fatigue Life The useful life of a component before it fails due to repeated use.

Free-Roll Rotation of the wheel without application of the brakes.

Homogeneity The magnitude of the output of a homogeneous system is directly proportional to the magnitude of the input.

Hysteresis Heat Heat generated by internal friction of the tyre rubber as it flexes.

Individual Power Result The result obtained for an individual braking test.

Land Freight Transport of cargo over land by truck or train.

Linearity A linear system is both homogeneous and additive.

Lumped Mass Formulation Distance parameters are neglected such that temperature is only a function of time. These models output average temperature.

Model Error The difference between measured and modelled data.

Percentage Error Model error as a percentage of the measured data.

Power-Averaged Result The curve obtained by taking the average value of the individual power results.

Randomised Optimisation The process of finding unknown parameters by randomly testing values within a specified range.

Sidewall Surface of the tyre forming the vertical walls between the bead and tread.

Single Wheels A type of wheel configuration where one rim and tyre is mounted to a single axle (singles).

Solution Space The range defined by the user wherein an optimisation routine searches for the value of a parameter.

Steady State The final/equilibrium value of a system response.

Temperature Distribution Measurements of temperature and multiple locations such that it can be described as a function of position and time.

Temperature Response Change in temperature as a function of time.

Thermal Gradient Temperature difference across a finite distance.

Thermal Interaction Heat transfer or temperature gradient between components.

Transient Response The time varying response of a system at it moves from one steady state to another due to the action of an input or a change in environment.

Tread Outer surface of the tyre which contacts the road.

Tyre Blowout Bursting of a tyre resulting in sudden and violent release of pressure.

Underdetermined A mathematical case where the number of unknowns is greater than the number of independent equations describing the system.

Wheel The combination of the rim and tyre.

Wheel Assembly The combination of the axle beam, brake, rim and tyre.

Wheel Configuration The use of dual or single wheels with steel or aluminium rims.

1 Introduction

1.1 Background and Motivation

The trucking industry is critical to the global economy, transporting over USD 19 trillion worth of goods worldwide in 2015 [1]. South Africa is especially dependent on heavy vehicles, which accounted for 76% of all land freight (472 billion tons of payload) for the period November 2017 - April 2018 [2].

Truck accidents can result in fatalities, late delivery, and destroyed cargo. The total estimated cost of road freight accidents to the South African public was R15 billion in 2012 [3]. Between January 2013 and May 2016, 131 major truck crashes were reported in South Africa which resulted in 726 injuries and 791 casualties [4]. In 2016, the Road Traffic Management Corporation investigated 36 truck accidents in which 136 people were injured and 143 killed [5]. Of the 131 accidents, vehicle related factors were the second most common cause [4]. This includes tyre blowout/fire and brake failure which are strongly linked to overheating brakes as a potential cause [6, 7]. A research gap exists in determining how the selection of wheel configuration (the use of dual or single wheels with steel or aluminium rims) affects the temperature of the brakes and tyres when the brakes are applied.

An investigation was undertaken to measure, model and compare the transient thermal response of various wheel configurations under extended braking. Better understanding of how the physical properties of the wheel impact on component heating and computational models will facilitate improved design and selection of heavy vehicle wheel assemblies as the effects of varying parameters - such as wheel size or rim material - on temperature response can be readily estimated.

1.2 Literature Survey

1.2.1 Consequences of Brake Overheating

The coefficient of friction of the brakes decreases at temperatures of 120 $^{\circ}C$ [8]. The resulting loss of braking power is termed *brake fade*, and can cause increased and unsafe stopping distances or total loss of control of the vehicle. Under alpine braking conditions, heavy vehicle brakes can exceed 300 $°C$ [9]. Alpine braking is defined as the braking to keep a vehicles speed constant when descending a slope i.e. an approximately constant braking power is dissipated for prolonged periods of time. The surfaces of drum brakes have been measured at 900 $°C$ which drastically increases wear, decreases braking performance and may lead to thermal cracking [10].

At high brake temperatures, proximate components are heated due to the dispersion of braking power. For tyres, exposure to temperatures between 90 $°C - 120$ $°C$ substantially decreases fatigue life [11]. This may result in premature and catastrophic tyre failure, i.e. a blowout [7]. In extreme cases, braking heat can cause the tyre to ignite [6].

1.2.2 Wheel Configuration

Heavy vehicles can be fitted with either dual or single wheels which are compared in Figure 1.1. Single wheels are increasing in popularity owing to their weight saving advantages over dual wheels. Further reduction in mass can be achieved by using aluminium rims in place of the conventional steel rims. The four wheel configurations commonly found on trucks are:

1. Dual wheels with steel rims (dual, steel).
2. Dual wheels with aluminium rims (dual, aluminium).
3. Single wheels with steel rims (single, steel).
4. Single wheels with aluminium rims (single, aluminium).

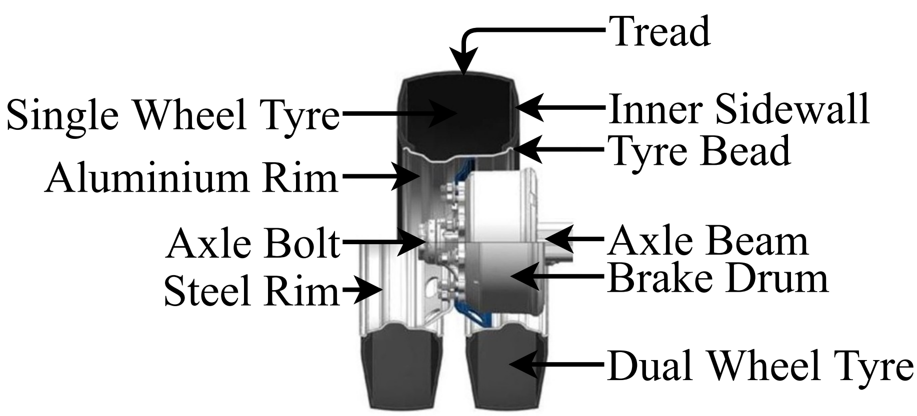

Figure 1.1: Comparison of Dual and Single Wheel Configurations.

The details of the specific materials used to manufacture rims and tyres are not made available by manufacturers. Thermophysical properties for steel, aluminium and rubber were therefore assumed based on data available in literature and listed in Table 1.1. Further information on the rims and tyres used in this study is given in Section 3.3.

Table 1.1: Bulk Material Properties.

Material	Thermal Conductivity k ($^{W}/_{m \cdot {}^{\circ}C}$)	Specific Heat C_p ($^{J}/_{kg \cdot {}^{\circ}C}$)	Density ρ ($^{kg}/_{m^3}$)	Source
Steel	60.50	434.0	7800	[12]
Aluminium	229.0	938.3	2701	[13]
Rubber	0.3113	1381	1310	[12, 14]

Previous research has shown that the thermal response of a dual, steel wheel under alpine braking differs to that of single, aluminium wheel [9, 15]. For 4 kW and 8 kW of continuous braking, the single, aluminium wheel exhibited slightly lower brake temperatures but far higher inner sidewall temperatures than the dual wheel. This was attributed to the increased thermal conductivity of the aluminium rim. The single aluminium rim was concluded to be at an appreciably higher risk of blowout since temperatures in excess of 150 $^{\circ}C$ were observed on the inner sidewall of the tyre, which is a likely location for the tyre to fail. The full range of wheel configurations were not compared since dual, aluminium wheels and single steel wheels were not tested. The degree to which thermal conductivity and surface area of the rim influences the surrounding component temperatures needs to be investigated.

1.2.3 Wheel Component Temperature Modelling

Finite element analysis (FEA) has been used extensively to model the thermal behaviour of mechanical friction brakes [16–30]. This method allows for the full transient temperature distribution of the components to be computed; illustrating the flow of braking heat and highlighting hotspots where failure is likely to occur. FEA requires simulation expertise, extensive computation and detailed knowledge of the wheel geometry, materials and construction. Consequently, FEA is impractical for application engineers or fleet operators who wish to understand the thermal characteristics of a wheel configuration.

FEA has been applied to tyre temperature, however studies have neglected braking effects and focused on self-heating which arises from hysteresis [11, 12, 14, 31–35]. The impact of inflation pressure on tyre overheating is well understood, but FEA has not been used to simulate the transfer of braking heat into the tyre.

Finite difference models (FDMs) are an alternative numerical technique to FEA [16]. The primary difference is that in FDMs the system is discretised into comparatively large elements to which energy balances and heat transfer equations are applied. This method produces less accurate models than FEA as geometry, material and boundary conditions are less rigorously defined.

Fisher [36] used FDMs to model the temperature response of wheels and axles under continuous braking. Initial guesses were made for relevant heat transfer parameters. A randomised optimisation procedure was employed to refine the model parameters. This method requires detailed geometry of the wheel assembly to be defined; which may not be available.

Day [16] details a lumped mass formulation which expresses brake temperature as a function of bulk parameters. This is simpler and uses readily-attainable input parameters. By neglecting distribution of mass and assuming constant physical properties, (average) brake temperature reduces to a first-order, time-invariant system response where braking power is the input function.

Day's model is limited in that it assumes all braking heat is dissipated by convection to the air. The lumped mass approach can be applied to the entire wheel assembly so long as the bulk properties of each component can be estimated. Where parameters are difficult to quantify, parameter ranges which likely contains the true values can be defined and the error between model outputs and experimental data minimised to determine these parameters. A similar approach was used by Fisher when developing FDMs.

1.2.4 Composite Materials in Automotive Applications

Carbon fiber reinforced polymers (CFRPs) have enormous potential in the automotive industry owing to their high strength-to-weight ratio which allows for substantially lighter components [37–40]. CFRP rims are of particular interest as reducing the mass of rotating components also decreases their moment of inertia; which amplifies acceleration and fuel economy improvements [41].

For heavy vehicles, lighter components allow for increased payload and therefore higher profits. CFRP rims have primarily been implemented on motorcycles and sports cars [39–42], while heavy vehicle manufacturers continue to investigate their suitability for trucks.

Insight into the impact of CFRP rims on the likelihood of wheel assembly component overheating is critical to the safe adoption of CFRP as a potential rim material. Lumped mass models can be used to estimate the thermal characteristics of CFRP-rimmed wheel assemblies without complex modelling or prototyping. This is achieved by estimating the thermophysical properties of the composite and extrapolating experimental/modelling results for steel and aluminium rims.

Table 1.2 describes the composition of a plain woven[i] CFRP sample for which the thermal conductivity has been experimentally determined. v, ρ and C_p denote the volume fraction, density and thermal capacity of the composite's constituents.

Table 1.2: Constituent Properties of Plain Woven CFRP [44].

Parameter	Unit	Fibre	Matrix
Material	–	Carbon Fiber T700S-12K	Epoxy Resin JC-02A
v	%	32.56	67.44
ρ	$^{kg}/_{m^3}$	1800	1130
C_p	$^{J}/_{kg\,\cdot\,^\circ C}$	750.0	1200

The measured conductivities for the CFRP sample are listed in Table 1.3. CFRP is a non-homogeneous, anisotropic material where thermal conductivity depends on the direction of heat flux. Conduction through the rim is three-dimensional and so the directional conductivities are averaged to give an effective conductivity for the material.

[i] This is the weave pattern most often used in automotive applications for its strength and structural stability [43, 44].

Table 1.3: Directional Thermal Conductivities of Plain Woven CFRP [44].

Direction	k ($^W/_{m\cdot{}^\circ C}$)
In-Plane (xx)	5.8
In-Plane (yy)	4.3
Out-of-Plane (zz)	2.9
Average	4.3

1.3 Objectives

There is a need to understand the thermal characteristics of currently available wheel assemblies and to develop methods for predicting overheating of wheel assembly components when subjected to braking. The objectives of this study are:

1. To measure and compare the axle beam, brake, rim and tyre temperatures of aluminium-rimmed and steel-rimmed wheels in dual and single configuration under 1 kW to 4 kW of continuous braking.
2. To construct lumped-mass models which output the transient temperature response of the wheel assemblies to various braking powers.
3. To determine whether certain rim materials or wheel configurations are at an increased risk of tyre failure or brake overheating and identify the physical parameters which contribute to excessive component temperatures.
4. To evaluate the feasibility of CFRP truck rims with respect to the thermal characteristics of the wheel assembly and its likelihood of overheating.

2 Analysis

2.1 Energy Balance

The thermal system encompassing the wheel assembly can be divided into four control volumes: the axle, brake shoe/drum, rim and tyre. For a control volume, Equation 2.1 holds for both transient and steady state conditions.

$$Q_{in} + Q_{generated} = Q_{stored} + Q_{out} \tag{2.1}$$

Where Q denotes the rate of heat transfer (W). The variables listed in Table 2.1 are substituted into Equation 2.1 to give energy balances specific to each control volume. A simplified depiction of the thermal system is shown in Figure 2.1.

Table 2.1: Expanded Energy Balance Terms.

Component	Subscript	Q_{in}	$Q_{generated}$	Q_{stored}	Q_{out}
(Axle) Beam	b	Q_{sb}	$Q_{friction}$	$(m \cdot C_p)_b \cdot \dot{T}_b$	Q_{ba}
(Brake) Shoe/Drum	s	0	P_b	$(m \cdot C_p)_s \cdot \dot{T}_s$	$Q_{sb} + Q_{sr} + Q_{sa}$
Rim	r	Q_{sr}	0	$(m \cdot C_p)_r \cdot \dot{T}_r$	$Q_{rt} + Q_{ra}$
Tyre	t	Q_{rt}	$Q_{hysteresis}$	$(m \cdot C_p)_t \cdot \dot{T}_t$	Q_{ta}

Where:

- Q_{xy} denotes heat transfer between component x and component y $(^\circ C)$.
- $Q_{friction}$ is the heat generated in the axle beam by bearing friction (W).
- $m \cdot C_p$ is thermal capacity $(^J/_{^\circ C})$ which is the product of mass, m (kg), and specific heat, C_p $(^J/_{kg \cdot {}^\circ C})$.
- $\dot{T}$ denotes the first derivative of temperature with respect to time $(^{\circ C}/_s)$.
- Q_{xa} denotes heat transfer between component x and the air $(^\circ C)$.
- P_b is the braking power generated by frictional rubbing (W).
- $Q_{hysteresis}$ is the hysteresis heat generated in the tyre as it rolls and deforms (W).

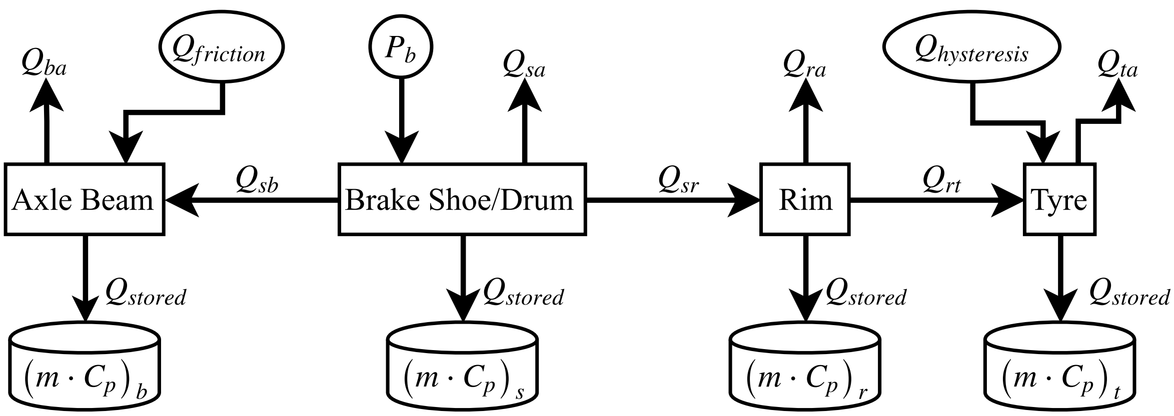

Figure 2.1: Heat Flow Diagram.

Heat is transmitted by conduction, convection and radiation[ii] such that

$$Q_{xy} = (Q_{conduction} + Q_{convection} + Q_{radiation})_{xy}$$

And

$$Q_{conduction} = \frac{k_{xy} \cdot A_{c,xy}}{L_{e,xy}} (T_x - T_y)$$

$$Q_{convection} = h_{xy} \cdot A_{s,xy} (T_x - T_y)$$

$$Q_{radiation} = \sigma_r \left(\frac{1 - \epsilon_x}{A_{s,x}\epsilon_x} + \frac{1}{A_{s,x}F_{xy}} + \frac{1 - \epsilon_y}{A_{s,y}\epsilon_y} \right)^{-1} (T^4_{x,abs} - T^4_{y,abs})$$

Where:

- T is temperature $(^\circ C)$.
- T_{abs} is absolute temperature (K).
- L_e is the effective conductive length (m).
- $\overline{k}_{xy}$ is the mean thermal conductivity between components x and y $(W/m \cdot {}^\circ C)$.
- h_{xy} is the convective heat transfer coefficient between x and y $(W/m^2 \cdot {}^\circ C)$.
- $A_{c,xy}$ and $A_{s,xy}$ are effective cross-sectional and surface areas respectively (m^2).
- F_{xy} is the view factor from surface x to surface y $(-)$.
- σ_r is the Stephan-Boltzmann constant $(\sigma_r = 5.68 \times 10^{-8}\ W/m \cdot K^4)$.
- ϵ is emissivity $(-)$.

It is common practice to incorporate the effects of radiation into convective heat transfer [13] using the relationship

$$Q_{convection} + Q_{radiation} = h_{e,xy} \cdot A_{s,xy} (T_x - T_y) \tag{2.2}$$

Where $h_{e,xy}$ is the combined radiative and convective heat transfer coefficient $(W/{}^\circ C)$. This simplification linearises the effects of radiation and is therefore an approximation. Total heat transfer can now be expressed as:

$$Q_{xy} = \left(\frac{k_{xy} \cdot A_{c,xy}}{L_{c,xy}} + h_{e,xy} \cdot A_{s,xy} \right) (T_x - T_y) \tag{2.3}$$

For simple geometries and homogeneous materials, heat transfer coefficients can be calculated from empirical correlations reported in literature. For a system as complex

[ii]Equations of heat transfer are discussed by Welty et al. [13].

as a wheel assembly, analytical determination of the heat transfer parameters is not feasible. Equation 2.4 defines the overall heat transfer coefficient, U ($^{W}/_{\circ C}$), which linearly relates heat transfer to temperature difference.

$$U_{xy} = \frac{k_{xy} \cdot A_{c,xy}}{L_{c,xy}} + h_{e,xy} \cdot A_{s,xy} \tag{2.4}$$

Assume $T_s > T_r > T_t > T_b > T_\infty$, where T_∞ is the ambient temperature which is assumed to remain constant. The transient energy balances for the axle beam, brake shoe/drum, rim and tyre are therefore given by Equation 2.5, 2.6, 2.7 and 2.8 respectively.

$$U_{sb}\left\{T_s(t) - T_b(t)\right\} + Q_{friction} = \left(m \cdot C_p\right)_b \dot{T}_b(t) + U_{ba}\left\{T_b(t) - T_\infty\right\} \tag{2.5}$$

$$\begin{aligned} P_b(t) = \left(m \cdot C_p\right)_s \dot{T}_s(t) + U_{sb}\left\{T_s(t) - T_b(t)\right\} + U_{sr}\left\{T_s(t) - T_r(t)\right\} \\ + U_{sa}\left\{T_s(t) - T_\infty\right\} \end{aligned} \tag{2.6}$$

$$U_{sr}\left\{T_s(t) - T_r(t)\right\} = \left(m \cdot C_p\right)_r \dot{T}_r(t) + U_{rt}\left\{T_r(t) - T_t(t)\right\} + U_{ra}\left\{T_r(t) - T_\infty\right\} \tag{2.7}$$

$$U_{rt}\left\{T_r(t) - T_t(t)\right\} + Q_{hysteresis} = \left(m \cdot C_p\right)_t \dot{T}_t(t) + U_{ta}\left\{T_t(t) - T_\infty\right\} \tag{2.8}$$

Equation 2.5 - 2.8 are rewritten in the matrix form defined in Equation 2.9.

$$\mathbf{B} \cdot \dot{\mathbf{T}}(t) + \mathbf{A} \cdot \mathbf{T}(t) = \mathbf{C}(t) \tag{2.9}$$

Where:

$$\mathbf{A} = \begin{bmatrix} U_{ba} + U_{sb} & -U_{sb} & 0 & 0 \\ -U_{sb} & U_{sb} + U_{sr} + U_{sa} & -U_{sr} & 0 \\ 0 & -U_{sr} & U_{sr} + U_{ra} + U_{rt} & -U_{rt} \\ 0 & 0 & -U_{rt} & U_{rt} + U_{ta} \end{bmatrix}, \quad \mathbf{T}(t) = \begin{bmatrix} T_b(t) \\ T_s(t) \\ T_r(t) \\ T_t(t) \end{bmatrix}$$

$$\mathbf{B} = \begin{bmatrix} (m \cdot C_p)_b & 0 & 0 & 0 \\ 0 & (m \cdot C_p)_s & 0 & 0 \\ 0 & 0 & (m \cdot C_p)_r & 0 \\ 0 & 0 & 0 & (m \cdot C_p)_t \end{bmatrix}, \quad \dot{\mathbf{T}}(t) = \begin{bmatrix} \dot{T}_b(t) \\ \dot{T}_s(t) \\ \dot{T}_r(t) \\ \dot{T}_t(t) \end{bmatrix}$$

$$\mathbf{C}(t) = \begin{bmatrix} T_\infty \cdot U_{ba} + Q_{friction} \\ T_\infty \cdot U_{sa} + P_b(t) \\ T_\infty \cdot U_{ra} \\ T_\infty \cdot U_{ta} + Q_{hysteresis} \end{bmatrix}$$

2.2 State-Space Formulation

The state-space-approach[iii] is a generalised method for modelling the time-dependent response of a multiple input, multiple output system. For the wheel assembly, $\mathbf{C}(t)$ contains the system inputs and the various component temperatures are the system outputs. Equation 2.10 is the generalised form of the state space equation.

$$\dot{\mathbf{x}}(t) = \mathbf{D} \cdot \mathbf{x}(t) + \mathbf{E} \cdot \mathbf{u}(t) \tag{2.10}$$

Where:

$$\mathbf{D} = \begin{bmatrix} d_{11} & d_{12} & \dots & d_{1n} \\ d_{21} & d_{22} & \dots & d_{2n} \\ \vdots & & & \\ d_{n1} & d_{n2} & \dots & d_{nn} \end{bmatrix}, \mathbf{x}(t) = \begin{bmatrix} x_1(t) \\ x_2(t) \\ \vdots \\ x_n(t) \end{bmatrix}, \mathbf{E} = \begin{bmatrix} e_{11} & \dots & e_{1m} \\ e_{21} & \dots & e_{2m} \\ \vdots & & \\ e_{n1} & \dots & e_{nm} \end{bmatrix}, \mathbf{u}(t) = \begin{bmatrix} u_1(t) \\ u_2(t) \\ \vdots \\ u_m(t) \end{bmatrix}$$

Here, $\mathbf{x}(t)$ is the state vector which gives the output of the system as a function of time in response to the input vector $\mathbf{u}(t)$. $\mathbf{D}$ and $\mathbf{E}$ are the system and control matrices respectively, which govern the response dynamics (rise time, steady state value, etc.).

$\dot{\mathbf{T}}(t)$ in Equation 2.9 is isolated to obtain the state-space form of the thermal system (Equation 2.11).

$$\dot{\mathbf{T}}(t) = \left(-\mathbf{B}^{-1} \cdot \mathbf{A}\right)\mathbf{T}(t) + \mathbf{B}^{-1} \cdot \mathbf{C}(t) \tag{2.11}$$

The solution to Equation 2.11 is found through the Laplace transform and is given in Equation 2.12.

$$\mathbf{T}(t) = \mathscr{L}^{-1}\left\{\left(s\mathbf{I} + \mathbf{B}^{-1} \cdot \mathbf{A}\right)^{-1}\mathbf{T}(0) + \left(s\mathbf{I} + \mathbf{B}^{-1} \cdot \mathbf{A}\right)^{-1}\mathbf{B}^{-1} \cdot \mathbf{C}(s)\right\} \tag{2.12}$$

Where:

- $\mathscr{L}^{-1}$ indicates the inverse Laplace transform operation.
- $\mathbf{I}$ is the identity matrix.
- $\mathbf{T}(0)$ is a column vector of the initial component temperatures ($°C$).
- $\mathbf{C}(s) = \mathscr{L}\{\mathbf{C}(t)\}$.

Equation 2.12 is indirectly solved using the MATLAB command *lsim*, allowing the transient temperature response of each component to be computed and plotted for any braking profile.

[iii] State-space methods are discussed by Burns [45].

3 Apparatus

3.1 Facility Overview

Experiments were performed using a custom-built rolling road rig depicted in Figure 3.1 and Figure 3.2. A heavy vehicle axle was mounted to a steel frame such that the tyre rests midway between two rollers. An electric motor applied a torque to the rollers (through a chain and sprocket gearing system) which in turn rotated the wheel. The other end of the axle was fastened to vertical, threaded rods for rigid support.

(a) Inner Sidewall View.

(b) Outer Sidewall View.

Figure 3.1: Wits Rolling Road Rig.

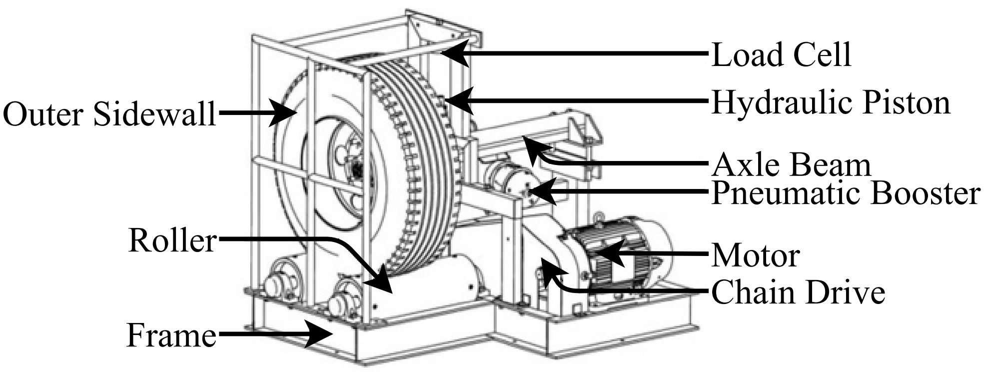

Figure 3.2: Rolling Road Rig Diagram.

A BPW Eco Plus 2[iv] axle was fitted with drum brakes and one of the four wheels discussed in Section 3.3. The brakes were actuated by externally-supplied compressed air which was fed to a pneumatic brake booster. A hydraulic piston actuated between

[iv]The BPW Eco Plus 2 axle is compatible with both single and dual wheels.

the axle and frame to apply a vertical force to the wheel. This gave the tyres sufficient traction against the rollers, and induced hysteresis heating in the tyres.

A programmable logic controller (PLC) modulated the wheel speed, axle load and driving power according to user-defined inputs. The PLC varied the power supplied to the motor to maintain a constant wheel speed. When the brakes were applied, the booster pressure was increased/decreased until the driving power at the input speed equalled the setpoint. The axle load was similarly controlled by actuating the cylinder according to the force measured by a load cell. Detailed descriptions of the system components follows below.

3.2 Electric Drive System

Table 3.1 lists the components of the electric drive system; all of which are manufactured by Siemens. 380 V AC was connected to a power module via an AC choke which filtered out high-frequency current to prevent damage to the motor and power module. The power module supplied voltage to a 30 kW electric motor as commanded by the motor control unit (MCU), which determined the motor speed and torque. Excess energy generated when the motor braked was dissipated in the braking resistor. An intelligent operator panel was attached to the MCU for manual operation of the motor. The drive module was controlled remotely via an Ethernet connection to a PC.

Table 3.1: Siemens Electric Drive System Components.

Component	Range	Model
30 kW Electric Motor	SIEMENS	1LG4207-4AA60-Z
AC Commutation Choke	SINAMICS	6SL3203-0CJ28-6AA0
Intelligent Operator Panel	SINAMICS	G120 6SL3255-0AA00-4JC1
Braking Resistor	MICROMASTER	6SE6400-4BD22-2EA1
Power Module	SINAMICS	240
Motor Control Unit	SINAMICS	CU240E-2 PN

3.3 Wheel Configurations

Table 3.2 lists the relevant properties of the rims and tyres which were used in this study. Steel and aluminium rims were tested in both dual and single configurations. The values for the dual wheels are for the individual rims and tyres and should be doubled to obtain the combined masses.

Table 3.2: Overview of Wheel Configurations.

Configuration	Rim			Tyre		
	Model	Mass (kg)	Thickness (mm)	Model	Size	Mass (kg)
Dual, Steel	Unknown	32.5	12.0	Dunlop Transteel 811	315/80 R22.5	67.0
Dual, Aluminium	Speedline SL830	28.0	24.5	Dunlop SP 391	315/80 R22.5	70.5
Single, Steel	Unknown	53.5	13.0	Firestone TSP 3000 II	385/65 R22.5	71.5
Single, Aluminium	Speedline SL291	26.0	26.0	Dunlop Transteel 833	385/65 R22.5	75.5

Figure 3.3 depicts the aluminium rims[v]. The thicknesses listed in Table 3.2 apply to the hub where the rim is bolted to the axle. The dish thicknesses of the dual, steel; dual, aluminium; and single, aluminium rims were measured to be 7.0 mm, 24.4 mm and 26.0 mm respectively. The single, steel rim does not have slots cut into the dish and so its thickness could not be readily measured.

3.4 Pneumatic System

Braking power was applied and regulated by controlling the air pressure input to a pneumatic brake booster. Compressed air at 6 bar was fed to a Festo LFR-1/4-D-MINI-A filter regulator which reduced the pressure to 3.5 bar. A Festo VPPM-6L-L-1-G18-0L6H-V1P-C1 proportional pressure regulator (PPR) supplied braking pressure (p_b, bar) to maintain the driving power at a user setpoint (P_d, W).

[v]The SL830 and SL921 rims were discontinued. Data sheets for the nearest equivalent rims currently in production were procured from BPW.

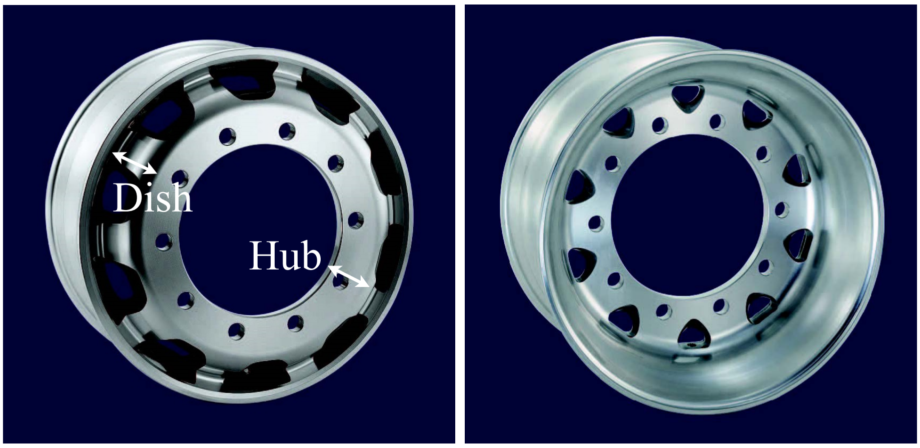

(a) Speedline SL830 (Dual) [46]. (b) Speedline SL291 (Single) [47].

Figure 3.3: Speedline SL Aluminium Rims.

The PLC signalled the PPR to increase/decrease the braking pressure according to the driving power output by the motor (P_r, W). This was achieved through a proportional-integral-derivative (PID) feedback loop. The simplified control algorithm is depicted in Figure 3.4. In flowcharts, rectangles and parallelograms denote processes and data objects respectively. The same convention is used in Figure 3.7 and Figure 5.2.

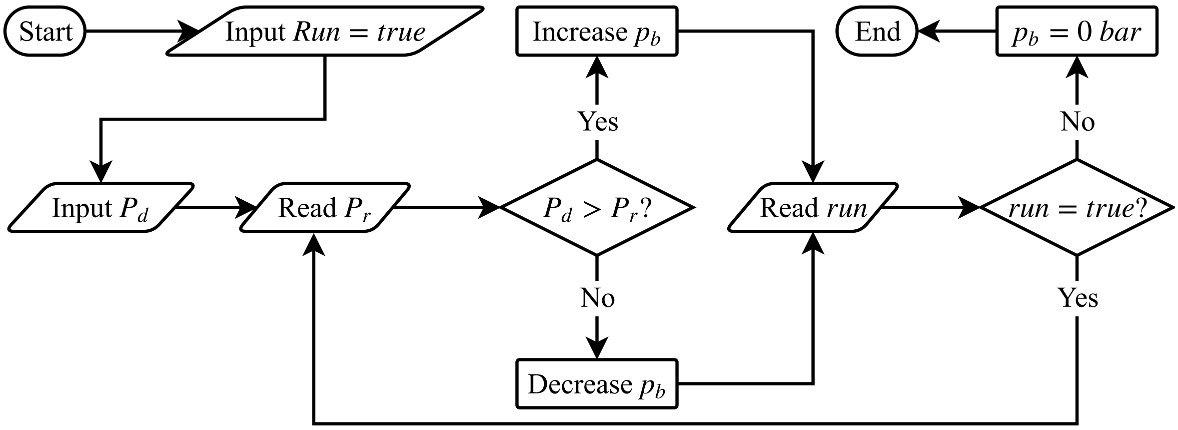

Figure 3.4: Driving Power Control Flowchart.

Figure 3.5[vi] shows a diagram of the pneumatic braking system. Component labels are shown as text followed by an arrow. A label enclosed in a box indicates a system input. In Figure 3.5, for example, there are two inputs: a signal input from the PLC to the PPR and a pressure input of 6 *bar* to the filter regulator. The same convention is used in Figure 3.6 and Figure 3.12.

[vi]The pressure regulators seen in Figure 3.5 were drawn using CAD files from Festo [48]. The image of the axle was taken from a report by Malzahn [49].

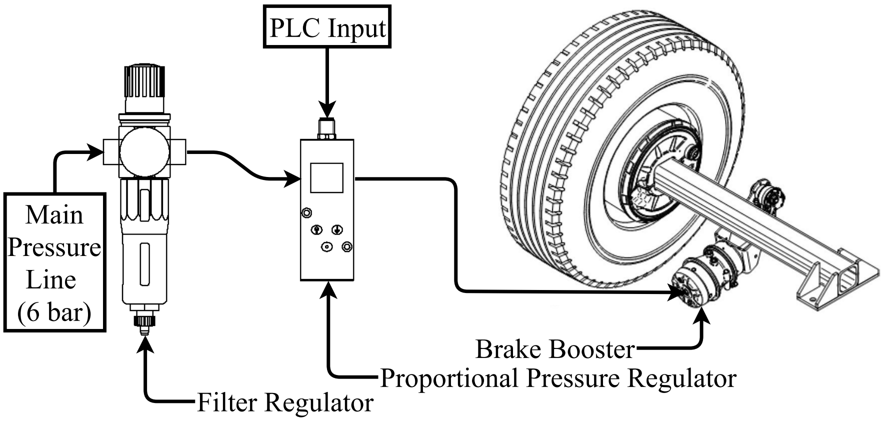

Figure 3.5: Pneumatic Actuation System.

3.5 Hydraulic System

A vertical force was applied to the axle by a hydraulic cylinder; the positioning of which can be seen in Figure 3.6[vii]. Hydraulic pressure was fed to a piston by a Fluid Power Group pump (detailed by Veerasamy [51]). When the cylinder extended, it contacted with the load cell which measured the force exerted between the axle and support frame (F_r, N).

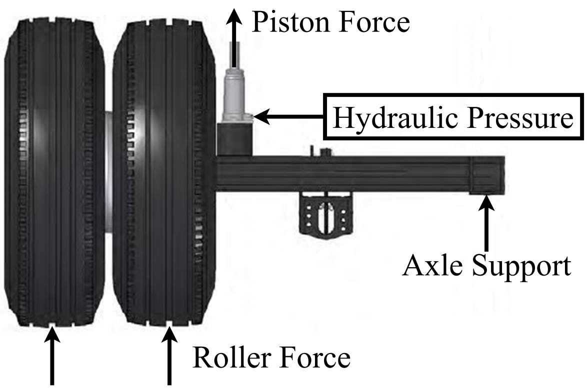

Figure 3.6: Axle Loading Diagram.

The cylinder was actuated using a proportional control valve (PCV). The direction of the cylinder's motion was determined by solenoid actuation of a CG24N9Z4 directional control valve (DCV). A PID feedback loop was used to maintain the axle load at the setpoint (F_s, N) by adjusting the extension of the cylinder. Figure 3.7 illustrates the simplified axle load control algorithm.

[vii]The image of the axle and tyres was taken from a report by Veerasamy [50].

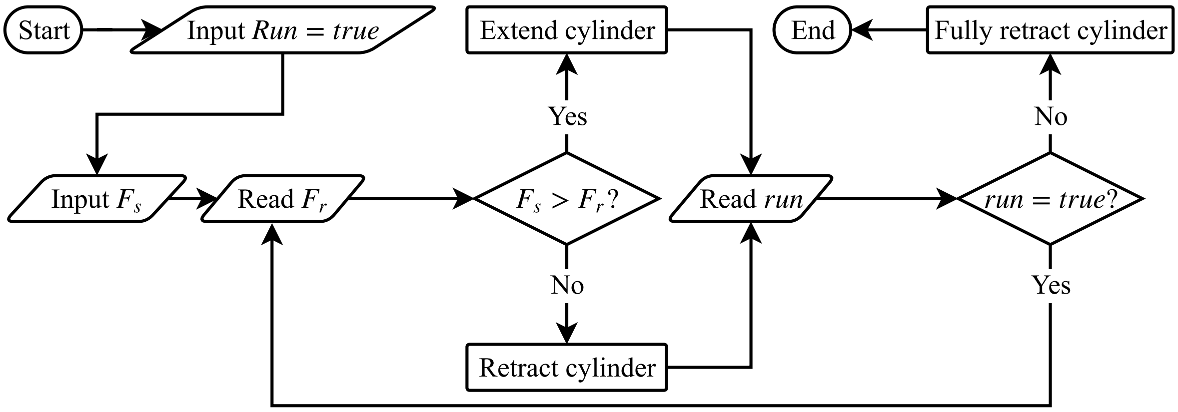

Figure 3.7: Axle Load Control Flowchart.

3.6 Instrumentation

Table 3.3 summarises the instrumentation used. A load cell and PPR recorded the values of axle load and braking pressure respectively. These instruments were monitored using Siemens Total Integrated Automation (TIA) Portal and a custom-built graphical user interface (GUI).

Table 3.3: List of Instrumentation.

Instrument	Manufacturer	Model	Accuracy	Sampling Interval (S)
Thermocouple (J-type, ×3)	Unitemp	STY5144A	2.2 $°C$	0.1
Thermal Imaging Camera	FLIR	T640	±2%	30
Proportional Pressure Regulator	Festo	VPPM-6L-L-1-G18-0L6H-V1P-C1	±2%	1
Load Cell	RDP	RLC5000	±105 kg	1

J-type thermocouples were embedded in the axle beam, brake shoe and axle bolt (Figure 3.8). The thermocouples were wired into an National Instruments SCXI-1303 front-mounting terminal block which was connected to an SCXI-1102 thermocouple amplifier card. This card was housed in and powered by an SCXI-1000 chassis. The SCXI-1102 thermocouple amplifier card signals were recorded using an SCXI-1600 data acquisition module. The SCXI-1600 interfaces with computer software via USB.

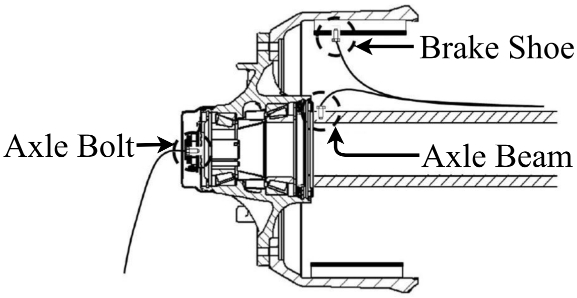

Figure 3.8: Thermocouple Locations.

A LabVIEW program was written to record and plot the thermocouple temperatures. The block diagram and front panel are shown in Figure 3.9a and Figure 3.9b respectively. Temperatures were sampled at a frequency of 10 Hz and plotted every 2 seconds.

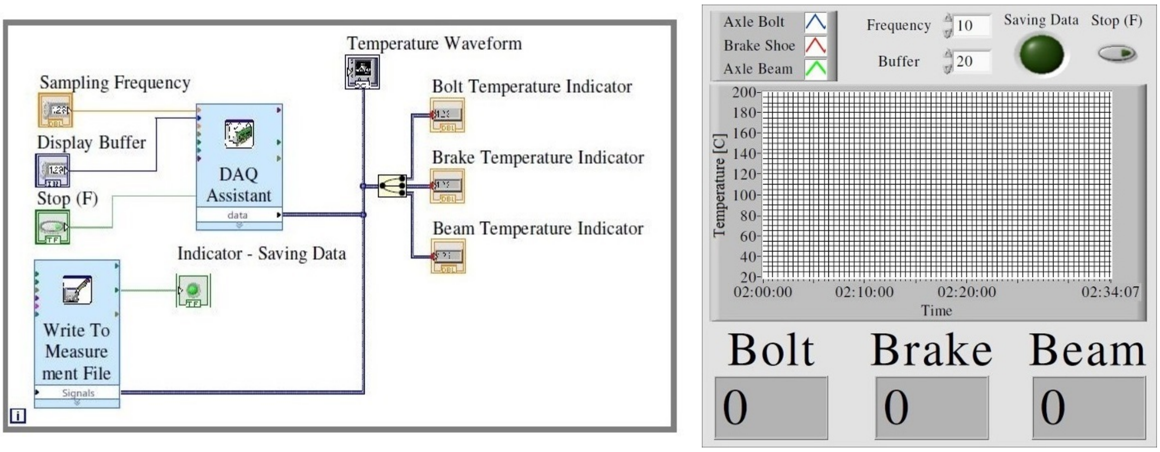

(a) Block Diagram.

(b) Front Panel.

Figure 3.9: *732069_Research_Thermocouple_Data_V1.vi* LabVIEW Program.

A FLIR T640 thermal imaging camera was used to record the surface radial temperature distribution of the inner sidewall of the tyre. This location was chosen as it is the closest to the brake and will undergo the greatest temperature change; thus it is the most likely location for blowout to occur. Figure 3.10a depicts the positioning of the camera and Figure 3.10b an example of the recorded thermal images which are imported into FLIR Tools for post-processing.

The tyre temperature used for lumped-mass modelling was calculated by taking the average temperature along the line "L_1", which extends radially outwards from the bead

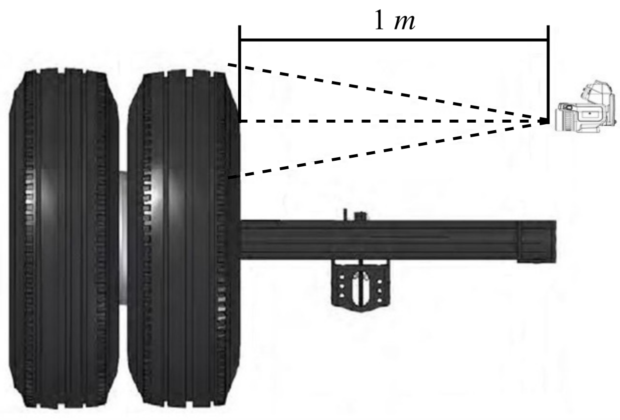

(a) Camera Positioning.

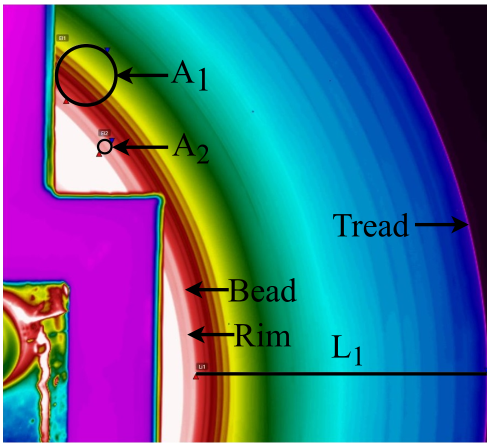

(b) Thermal Image.

Figure 3.10: FLIR T640 Thermal Imaging Camera Setup.

to the tread[viii]. The average temperatures in the regions labelled "A_1" and "A_2" were taken to be the maximum tyre temperature and the outer rim temperature respectively.

3.7 Remote Control System

The rig was operated remotely from a control room. A custom-built computer GUI was used to input operational setpoints and send them to a S7-1200 PLC. A screenshot of the program window is displayed in Figure 3.11. There are three inputs which can be changed throughout the test: (wheel) *Speed*, (motor driving) *Power* and (axle loading) *Force* defined in km/h, W and N respectively.

The measured values of these parameters (as well as motor torque and braking pressure) were sampled, displayed and logged in a *.csv* file at 1 second intervals.

Commands from the GUI were sent to the PLC through Siemens TIA Portal. Figure 3.12[ix] depicts the PLC components, their connections and their inputs/outputs. All modules seen in Figure 3.12 make up the S7-1200.

Control algorithms were uploaded to the central processing unit (CPU) 1212C which connected directly to the SM 1232 analogue output module. The SM 1232 converted digital signals from the CPU to analogue signals. The Festo PPR and hydraulic PCV

[viii] It is impractical to record the full temperature distribution of the tyre and so the average inner sidewall temperature is used since it is most relevant to overheating.

[ix] The PLC modules in Figure 3.12 were drawn using CAD files from Siemens [52].

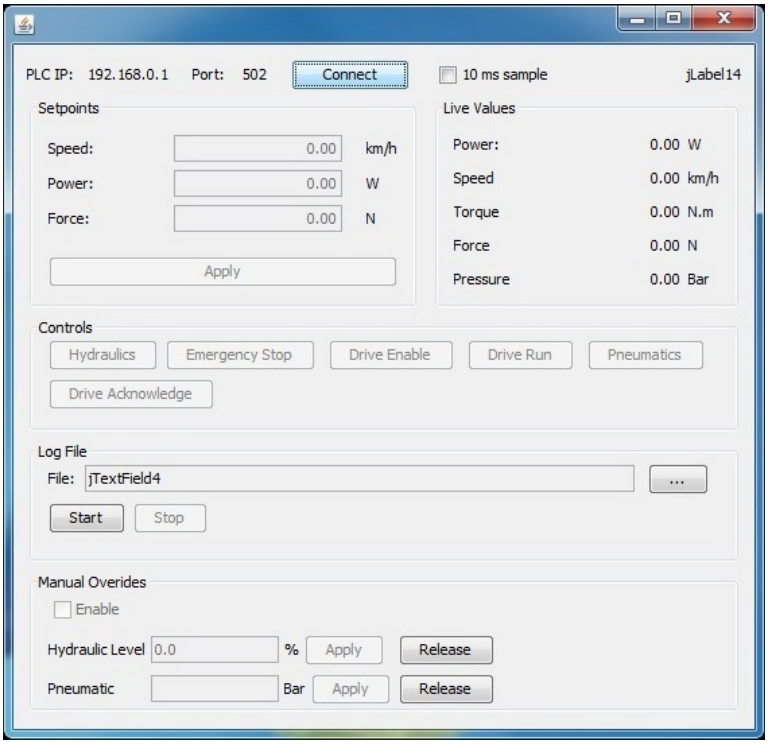

Figure 3.11: Rolling Road Control Graphical User Interface.

were connected to the SM 1232; allowing the braking pressure and axle load to be manipulated. The direction of the hydraulic cylinder's motion was determined by the output to the DCV which was sent from the CPU 1212C.

The compact switching module (CSM) 1277 transmitted signals between the CPU 1212C and the other control components, and communicated with the PC, MCU and WP231. Operational setpoints were uploaded to the CPU using the GUI on the PC. The MCU controlled the motor and fed back the measured operating values (power, torque and speed). The WP231 weighing module received the analogue output from the load cell. This signal was processed and transmitted to the CPU and PC.

4 Methodology

The axle load was applied and the wheel run at a constant speed without braking (free-roll) to reach an initial thermal steady state. At this point the driving power drawn by the motor has decreased to a constant value which was recorded. The driving power setpoint was determined by increasing the steady state free-roll power by the desired braking power. The brakes were then applied and the rig run at a constant driving

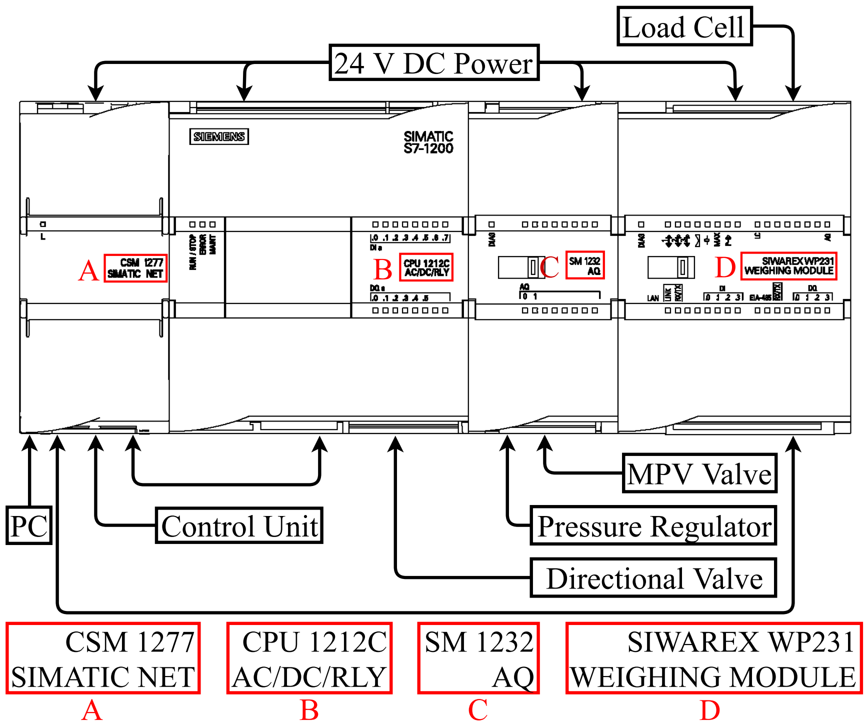

Figure 3.12: Programmable Logic Controller Diagram.

power until the test was terminated. The test parameters used in this study are listed in Table 4.1.

Table 4.1: Alpine Braking Test Parameters.

Test Parameter	Value	Unit
Axle Load	20	kN
Wheel Speed	20	$^{km}/_{h}$
Free-Roll Time	4	hours
Braking Time	4	hours
Braking Power	1, 2, 3, 4	kW

The axle load and wheel speed were selected based on the physical capabilities of the test rig as a higher speed or load would put excessive strain on the chain drive after the brakes were applied. Previous testing showed free-roll and braking times of 4 hours are needed to reach steady state. The braking power was limited to 4 kW to avoid unsafe temperatures. Testing was terminated if the brake or average tyre temperatures exceeded 300 $°C$ or 80 $°C$ respectively.

5 Data Processing

5.1 Response Averaging

The system described in Equation 2.11 is non-homogeneous owing to the constant terms in the differential equations. It is nevertheless assumed that the system is linear and thus additivity and homogeneity rules apply[x] such that:

$$S\left\{a_1 x_1(t) + a_2 x_2(t)\right\} = a_1 S\left\{x_1(t)\right\} + a_2 S\left\{x_2(t)\right\}$$

Therefore:

$$\frac{1}{n}\sum_{i=1}^{n} S\left\{x_i(t)\right\} = S\left\{\frac{1}{n}\sum_{i=1}^{n} x_i(t)\right\}$$

This states that the average of a system's outputs to various inputs is equal to the output in response to the average of the inputs, i.e.:

$$\overline{S}\left(x_i\right) = S(\overline{x}_i)\ ,\ 1 \leq i \leq n$$

Where a line above a variable denotes the average/mean. For each component of an individual wheel, the average temperature curve for the four tests was calculated to give the temperature response to the average braking power. Figure 5.1 illustrates this procedure for the dual, steel wheel where "1 kW" , "2 kW", "3 kW", and "4 kW" indicate the nominal setpoints and "$Av.$" is the power-averaged result ($P_b = 2.5\ kW$).

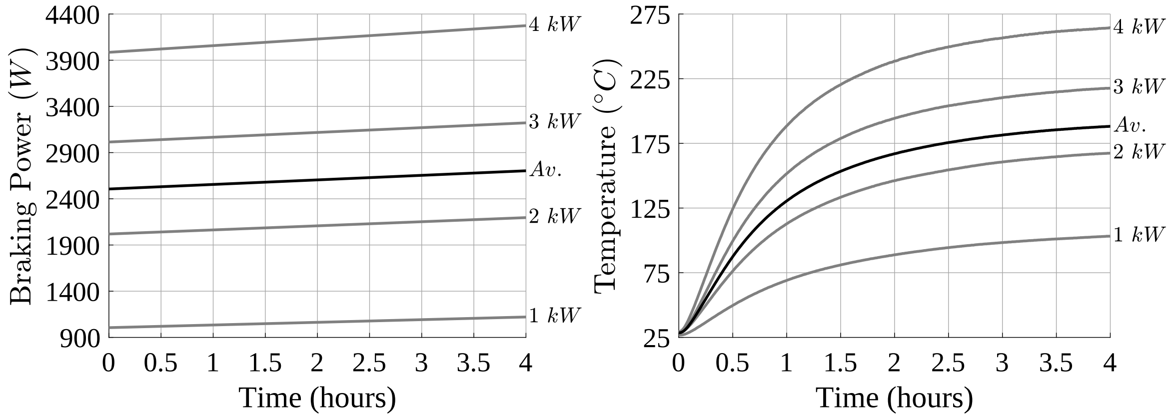

(a) Braking Power. (b) Brake Shoe Temperature.

Figure 5.1: Response Averaging Example (Dual, Steel).

Power-averaging the results reduced the number of responses to be calculated from 64 (1 curve per component per test per wheel) to 16, which considerably improved the speed

[x]This assumption is validated in Section 6.2.

of the optimisation procedure in Section 5.3. Averaging the responses also mitigated the impact of experimental errors which arose from changes in ambient conditions (air temperature, humidity, ventilative airflow, etc.).

5.2 Input/Output Discretisation

Over the duration of the test the power setpoint remained constant. However, the total power lost to friction and rolling resistance decreased as the test rig heated up. This caused an upward drift in braking power from a minimum at the onset of braking to a maximum just before the brakes were released. Table 5.1 lists the average initial and final braking powers $\left(\overline{P}_{b,i},\ \overline{P}_{b,f}\right)$ for each wheel configuration.

It was assumed that the braking power varied linearly between these two values. The time-dependent input function describing braking was therefore calculated using the straight line equations for $P_b(t)$ in Table 5.1.

Table 5.1: Braking Power Input Parameters.

Power (W)	Dual, Steel	Dual, Aluminium	Single, Steel	Single, Aluminium
$\overline{P}_{b,i}$	2506	2504	2499	2499
$\overline{P}_{b,f}$	2703	2690	2639	2671
$P_b(t)$	$\frac{197}{14400}t + 2506$	$\frac{186}{14400}t + 2504$	$\frac{140}{14400}t + 2499$	$\frac{172}{14400}t + 2499$

The state-space power input, $P_b(t)$, was updated at 30-second intervals over the 4-hour test i.e. for $t = \{0, 30, 60, ..., 14400\}$, which gave the input matrix:

$$\mathbf{C}(t) = \begin{bmatrix} T_\infty \cdot U_{ba} + Q_{friction} & T_\infty \cdot U_{ba} + Q_{friction} & \dots & T_\infty \cdot U_{ba} + Q_{friction} \\ T_\infty \cdot U_{sa} + P_b(t=0) & T_\infty \cdot U_{sa} + P_b(t=30) & \dots & T_\infty \cdot U_{sa} + P_b(t=14400) \\ T_\infty \cdot U_{ra} & T_\infty \cdot U_{ra} & \dots & T_\infty \cdot U_{ra} \\ T_\infty \cdot U_{ta} + Q_{hysteresis} & T_\infty \cdot U_{ta} + Q_{hysteresis} & \dots & T_\infty \cdot U_{ta} + Q_{hysteresis} \end{bmatrix}$$

The output matrix was returned as discrete temperatures in the form:

$$\mathbf{T}(t) = \begin{bmatrix} T_b(t=0) & T_b(t=30) & \dots & T_b(t=14400) \\ T_s(t=0) & T_s(t=30) & \dots & T_s(t=14400) \\ T_r(t=0) & T_r(t=30) & \dots & T_r(t=14400) \\ T_t(t=0) & T_t(t=30) & \dots & T_t(t=14400) \end{bmatrix}$$

5.3 Optimisation

There are 10 unknowns in Equation 2.9 and only 4 independent equations. The system is therefore underdetermined and the unknown coefficients cannot be solved through matrix manipulation alone. A random optimisation approach was used to find the combination of parameters which minimised the difference between the experimental data and the modelled response.

A cost function was defined and a solution space specified to constrain the optimisation to a reasonable range of values. Thereafter, a simulated annealing[xi] algorithm was used to incrementally refine the solution. Since certain parameters are common to different wheels, the optimisation was performed for all four configurations simultaneously.

5.3.1 Cost Function

A cost function defines the degree of agreement between the measured and modelled temperatures and must be minimised to obtain the best fit parameters. The error could be specified as the magnitude of the difference between the measured and modelled temperatures, but this would bias the solution towards the high-temperature region which compromises the accuracy of the model during the transient period. Percentage error is a more suitable metric for determining the accuracy of the model over a range of temperatures. The percentage error vector, $\mathbf{e}$, was calculated using Equation 5.1.

$$\mathbf{e} = 100 \times \frac{\mathbf{T}_{exp} - \mathbf{T}_{mod}}{\mathbf{T}_{exp}} \tag{5.1}$$

Where:

- $\mathbf{T}_{exp}$ is a vector of the measured temperature response of a component.
- $\mathbf{T}_{mod}$ is a vector of the modelled temperature response of a component.

Equation 5.1 was applied to each component of each wheel and the vectors concatenated to generate an overall error matrix (Equation 5.2).

$$\mathbf{E}_{\%} = \begin{array}{cl} \left[\begin{matrix} \mathbf{e}_b & \mathbf{e}_s & \mathbf{e}_r & \mathbf{e}_t \\ \mathbf{e}_b & \mathbf{e}_s & \mathbf{e}_r & \mathbf{e}_t \\ \mathbf{e}_b & \mathbf{e}_s & \mathbf{e}_r & \mathbf{e}_t \\ \mathbf{e}_b & \mathbf{e}_s & \mathbf{e}_r & \mathbf{e}_t \end{matrix}\right] & \begin{matrix} \leftarrow \textit{Dual, Steel} \\ \leftarrow \textit{Dual, Aluminium} \\ \leftarrow \textit{Single, Steel} \\ \leftarrow \textit{Single, Aluminium} \end{matrix} \end{array} \tag{5.2}$$

[xi] Simulated annealing optimisation routines are discussed by Jonhson et al. [53].

The overall percentage root-mean-square error ($RMSE$) was chosen as the cost function for optimisation and calculated using Equation 5.3.

$$RMSE = \sqrt{\frac{1}{n \times m} \sum_{j=1}^{n} \sum_{i=1}^{m} \mathbf{E}^2_{\%\ i,j}}\ , \quad \mathbf{E}_{\%} \in \mathbb{R}^{n \times m} \tag{5.3}$$

For $t = \{0, 30, ..., 14400\}$, $\mathbf{e} \in \mathbb{R}^{1 \times 481}$ and therefore $\mathbf{E}_{\%} \in \mathbb{R}^{4 \times 1924}$.

5.3.2 Solution Space

$(m \cdot C_p)_r$ and $(m \cdot C_p)_t$ were calculated from the data in Table 1.1. From literature [13] and information provided by BPW [54], the thermal capacity of the beam was estimated to be:

$$(m \cdot C_p)_b = 56.80\ {}^{kJ}\!/{}_{^\circ C}$$

The greater the number of unknowns, the slower and less accurate the overall optimisation. The values for $(m \cdot C_p)_r$, $(m \cdot C_p)_t$ and $(m \cdot C_p)_b$ were thus fixed. This left 7 unknown coefficients which determine the proportions in which heat was transferred throughout the wheel assembly. The local rate of heat transfer, Q_{xy} (W), is given by:

$$Q_{xy} = U_{xy} \Delta T_{xy}$$

Where ΔT_{xy} is the temperature difference between component x and y ($^\circ C$). Table 5.2 lists the maximum component temperatures for the power-averaged curves obtained in Section 5.1, and Table 5.3 the corresponding temperature differences.

Table 5.2: Maximum Component Temperatures (Power-Averaged).

Component	T_{max} ($^\circ C$)			
	Dual, Steel	Dual, Aluminium	Single, Steel	Single, Aluminium
Axle Beam	121.6	114.6	117.8	115.4
Brake Shoe	188.2	183.9	186.4	184.9
Rim	89.67	98.79	113.5	116.9
Tyre	48.50	50.61	61.26	71.24

It was assume that, at these temperatures, each thermal interaction transmitted between 5% and 50% of the final braking powers, $\overline{P}_{b,f}$, listed in Table 5.1. The fraction of power transmitted depends on the magnitude of the heat transfer coefficient, i.e.:

$$\frac{0.05 \cdot \overline{P}_{b,f}}{\Delta T_{xy}} \leq U_{xy} \leq \frac{0.5 \cdot \overline{P}_{b,f}}{\Delta T_{xy}} \tag{5.4}$$

Equation 5.4 was applied to each temperature difference in Table 5.3, and the overall minima and maxima (Table 5.4) used to bound the solution space. Table 5.5 gives the optimisation limits for the three remaining unknowns - $Q_{friction}$, $Q_{hysteresis}$ and $(m \cdot C_p)_s$ - which were determined by trial and error.

Table 5.3: Final Temperature Differences (Power-Averaged, $T_\infty = 25\ °C$).

Interaction	ΔT ($°C$)			
	Dual, Steel	Dual, Aluminium	Single, Steel	Single, Aluminium
Shoe - Beam	96.56	89.58	92.79	90.38
Shoe - Rim	66.60	69.27	68.61	69.57
Rim - Tyre	163.2	158.9	161.4	159.9
Beam - Air	98.49	85.06	72.88	68.09
Shoe - Air	41.17	48.19	52.25	45.62
Rim - Air	64.67	73.79	88.51	91.86
Tyre - Air	23.50	25.61	36.26	46.24

Table 5.4: Overall Heat Transfer Coefficients Optimisation Limits.

U_{xy} ($W/°C$)	Minimum	Maximum
U_{ba}	1.400	15.01
U_{sb}	1.920	20.29
U_{sa}	0.8175	8.467
U_{sr}	1.372	19.61
U_{rt}	2.525	32.83
U_{ra}	1.454	20.90
U_{ta}	2.888	57.51

Table 5.5: Miscellaneous Parameter Optimisation Limits.

Parameter	Unit	Minimum	Maximum
$Q_{friction}$	W	0	1000
$Q_{hysteresis}$	W	0	1000
$(m \cdot C_p)_s$	$kJ/°C$	40	60

5.3.3 Simulated-Annealing Algorithm

Initial estimates for each unknown parameter were randomly generated and used to calculate the temperature responses of the four wheels. Each iteration, a single parameter was randomly selected and varied within its specified limits. The temperature response and the overall percentage $RMSE$ were calculated. If the $RMSE$ decreased between successive iterations, the change was automatically accepted.

Intuitively, only "downhill" moves (changes which decrease the cost function) should be accepted. However, this approach tends to trap the solution in local optima. The simulated annealing algorithm - summarised in a flowchart in Figure 5.2 - allows for occasional uphill moves which enables the optimisation to escape local optima, explore the solution space more fully and thereby find the global optimum solution. A description of the simulated-annealing algorithm follows.

If the $RMSE$ increases between iterations, the inequality in Equation 5.5 is evaluated.

$$exp\left(-\frac{\Delta RMSE}{T_{sim}}\right) \geq R \tag{5.5}$$

Where:

- $exp(x) \equiv e^x$.
- R is a randomly generated number between 0 and 1.
- T_{sim} is the simulated annealing temperature; a virtual temperature which decreases with each iteration of the optimisation ($°C$).

If the equality is true, the change is accepted. Otherwise, the change is rejected and the parameter reverts to its previous value. Note that the larger the increase in $RMSE$ and the higher the value of T_{sim}, the less likely an uphill move is to be accepted. T_{sim} is recalculated each iteration using Equation 5.6.

$$T_{sim} = T_{sim,0} \cdot exp(-d \times i) \tag{5.6}$$

Where:

- $T_{sim,0}$ is the initial simulated temperature ($°C$). $T_{sim,0}$ is chosen such that initially every change is accepted and so the entire solution space is explored.
- d is a decay factor which governs the rate at which T_{sim} decreases ($-$). Small values yield more refined solutions at the cost of increasing computation time.

- i is the number of iterations which have been performed $(-)$.

Towards the end of the optimisation, virtually no uphill move will be accepted. The optimisation terminates when $T_{sim} \leq T_{min}$, a minimum temperature also specified by the user. The lower the value of T_{min} $(°C)$, the longer the optimisation spends searching exclusively for downhill moves and the more refined the solution.

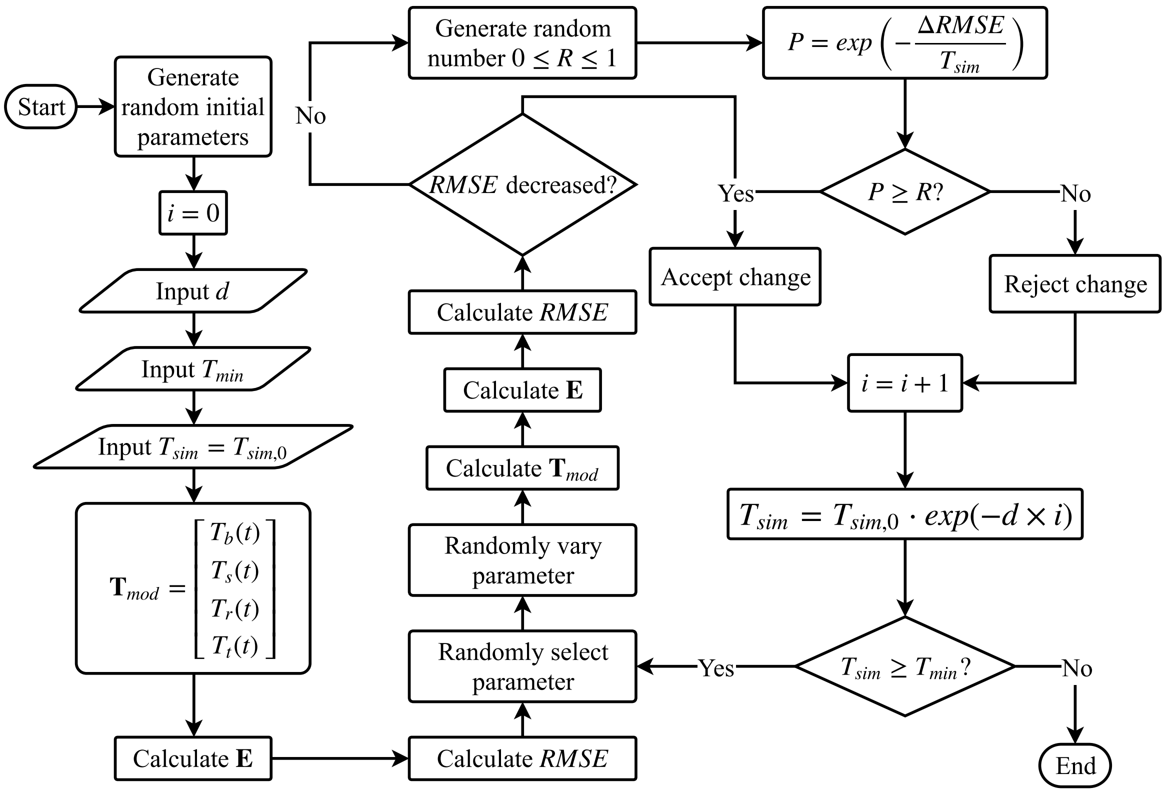

Figure 5.2: Simulated Annealing Optimisation Algorithm.

5.3.4 Assumptions

It was assumed that the values of certain parameters were equal for multiple configurations. These assumptions are stated and justified below:

- U_{ba}, U_{sb}, U_{sa}, $(m \cdot C_p)_b$ and $(m \cdot C_p)_s$ are the same for all four configurations as they depend on the axle's properties which do not change for different wheels.

- $(U_{ta})_{Dual,\ Steel} = (U_{ta})_{Dual,\ Aluminium}$ and $(U_{ta})_{Single,\ Steel} = (U_{ta})_{Single,\ Aluminium}$. U_{ta} depends on tyre geometry which is similar for tyres of the same size.

- $Q_{friction}$ is the same for all four configurations as the heat generated in the axle bearing is independent of wheel configuration.
- $Q_{hysteresis}$ is the same for all four configurations. Hysteresis heating is extremely difficult to estimate, however is it roughly proportional to the ratio of the applied load to the volume of rubber being deformed [55] (assumed to be the same for all tests).

5.3.5 Distributed Temperature Compensation

The geometry of the wheel assembly makes it difficult to measure the temperature distribution in components such as the brake, beam and rim. Local temperatures were therefore recorded which did not directly equal the average temperature of the body, but with analysis of the geometry could be used to estimate the average temperature.

The rim temperature (measured at the outer edge) decreases with increasing distance from the brake. It follows that the corrected rim temperature is a weighted average of the measured brake and rim temperatures (Equation 5.7). The temperature of the beam was recorded at the end nearest to the brake and decreases from a maximum at this location to approximately room temperature at its opposite end. The corrected beam temperature was thus a weighted average of the measured beam temperature and the ambient temperature (Equation 5.8).

$$T_r(t)_{average} = W_r \cdot T_r(t)_{measured} + (1 - W_r) \cdot T_s(t)_{measured} \tag{5.7}$$

$$T(t)_{b,average} = W_b \cdot T_b(t)_{measured} + (1 - W_b) \cdot T_{\infty,assumed} \tag{5.8}$$

W in Equation 5.7 and Equation 5.8 is a fractional weighting factor $(-)$. The weighting factors were chosen such that the overall $RMSE$ of the model was minimised. This was achieved by assuming an ambient temperature of $T_\infty = 25\ °C$ and defining:

$$W_r = \{0, 0.1, 0.2, ..., 1\}\ ,\ W_b = \{0, 0.1, 0.2, ..., 1\}$$

An optimisation was run for each permutation of these factors i.e.

$$\mathbf{P} = \begin{bmatrix} 0 & 0 & 0 & 0 & 0 & \cdots & 1 & 1 & 1 & 1 \\ 0 & 0.1 & 0.2 & 0.3 & 0.4 & \cdots & 0.7 & 0.8 & 0.9 & 1 \end{bmatrix}$$

This was repeated 5 times and the average $RMSE$ obtained using each combination plotted in Figure 5.3. The global minimum $RMSE$ occurred where:

$$W_r = 1.0\ ,\ W_b = 0.2$$

These results imply that the measured rim temperatures were close approximations of the overall average. The average beam temperatures used in subsequent calculations were corrected by substituting $W_b = 0.2$ into Equation 5.8, which is demonstrated for the dual, steel wheel in Figure 5.4.

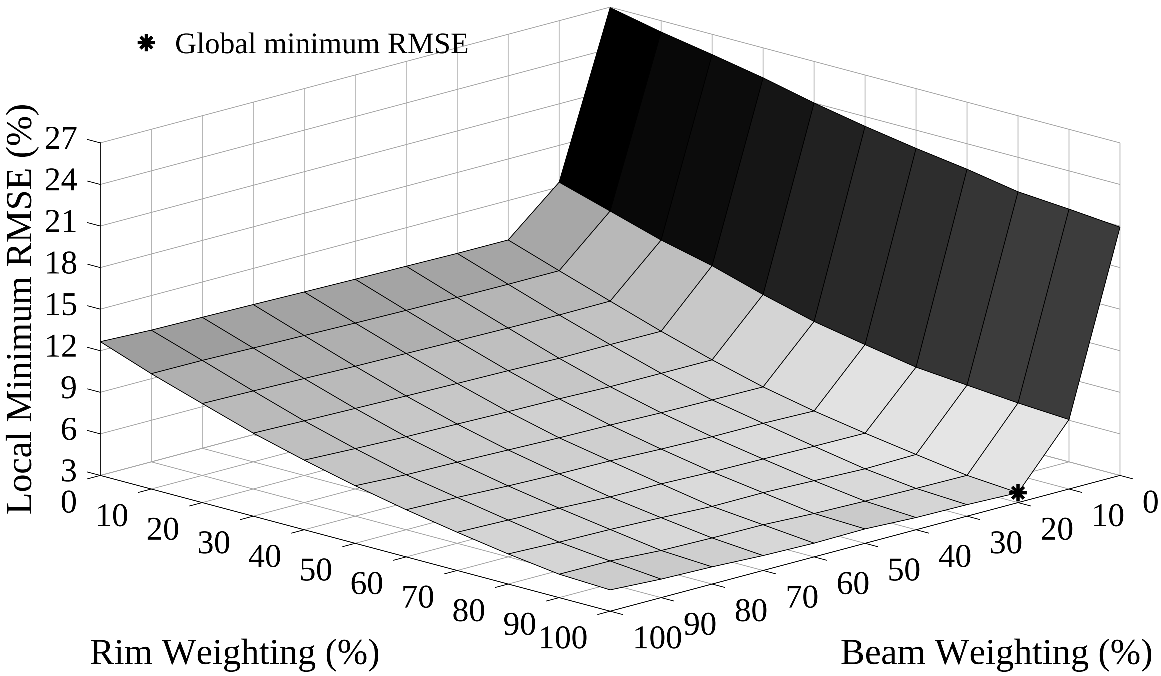

Figure 5.3: Evaluation of Temperature Weighting Factors.

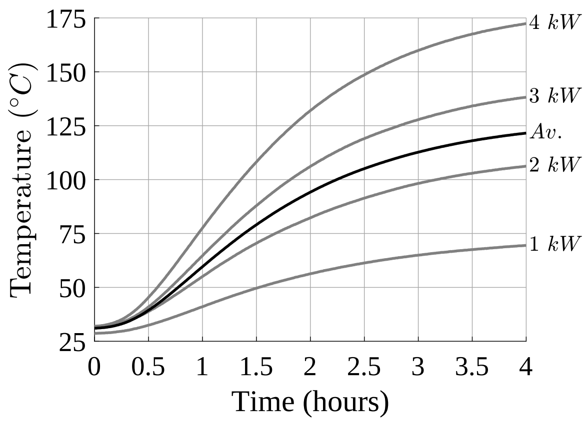

(a) Measured.

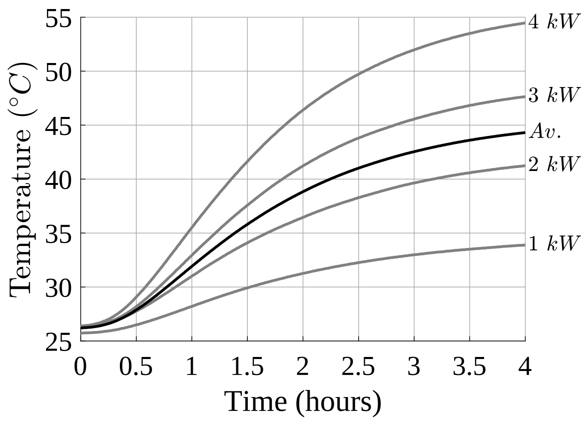

(b) Corrected.

Figure 5.4: Beam Temperature Correction (Dual, Steel, $W_b = 0.2,\ T_\infty = 25\ °C$).

5.3.6 Model Finalisation

Table 5.6 lists the parameters used in the final optimisation of the lumped mass models. These values were chosen based on a trial and error approach for their consistent and low final *RMSE* and reasonable runtime (approximately 1 minute per solution).

Table 5.6: Final Optimisation Parameters.

Parameter	Value	Unit
$T_{sim,0}$	1000	$^\circ C$
T_{min}	1×10^{-9}	$^\circ C$
d	5×10^{-4}	$-$

The optimisation was run 100 times and the solutions recorded. The finalised parameters - listed in Table 6.1 - were calculated by averaging the 100 values for each parameter.

5.4 Thermal Characteristics of CFRP Rims

CFRP rims are not available for heavy vehicle applications. Their relevant properties can, however, be estimated based on information and modelling results for steel and aluminium rims. Future CFRP rims must conform to industry standard sizes to be compatible with current vehicles and tyres. The volumes of the four rims which were tested are listed in Table 5.7. The average volume $\left(\overline{V},\ m^3\right)$ of the dual and single rims were calculated and used to estimate the volume of the equivalent CFRP rim.

Table 5.7: Estimation of CFRP Rim Volumes.

Parameter	Unit	Dual, Steel	Dual, Aluminium	Single, Steel	Single, Aluminium
m	kg	65.00	56.00	53.50	26.00
ρ	$^{kg}/_{m^3}$	7800	2701	7800	2701
V	$m^3 \times 10^3$	8.333	20.73	6.859	9.626
$\overline{V}$	$m^3 \times 10^3$	14.53		8.242	

The overall density, mass and specific heat of the CFRP were calculated using Equation 5.9 to Equation 5.11[xii] and the data in Table 1.2. These results are listed in Table 5.8 and are later used to estimate the total thermal capacities, $(m \cdot C_p)_r$, of CFRP rims in dual and single configurations. Note the subscripts c, f and m denote the (overall) *composite*, (carbon) *fibre* and (epoxy resin) *matrix* respectively.

$$\rho_c = \rho_f v_f + \rho_m v_m \tag{5.9}$$

$$m_c = \rho_c V_c \tag{5.10}$$

$$C_{p,c} = \frac{\rho_f v_f C_{p,f} + \rho_m v_m C_{p,m}}{\rho_f v_f + \rho_m v_m} \tag{5.11}$$

Table 5.8: Bulk Properties of CFRP Rims.

Parameter	Unit	Dual	Single
V	$m^3 \times 10^3$	14.53	8.242
ρ	$^{kg}/_{m^3}$	1348	
m	kg	19.59	11.11
C_p	$^{J}/_{kg\cdot°C}$	1004	

Changing the rim material will affect the following parameters in the lumped-mass model:

$$U_{sr},\ U_{rt},\ U_{ra},\ U_{ta},\ (m \cdot C_p)_r \text{ and } (m \cdot C_p)_t$$

Parameters relating to the axle and brake do not vary. U_{sr} and U_{rt} are predominantly conductive heat transfer parameters and therefore:

$$U_{sr} \approx \overline{k}_{sr} \left(\frac{A_c}{L_e}\right)_{sr} ,\ U_{rt} = \overline{k}_{rt} \left(\frac{A_c}{L_e}\right)_{rt}$$

Where $\overline{k}$ is the average thermal conductivity between two materials. For the flow of heat between different materials, the average thermal conductivity is a weighted average of the constituent thermal conductivities which accounts for the volume fraction of each material present. For the purposes of this analysis and understanding the experimental results, a simple average without weightings was used.

For steel rims:

$$\overline{k}_{sr} = k_{steel} ,\ \overline{k}_{rt} = \frac{k_{steel} + k_{rubber}}{2}$$

[xii] Calculation of composite material properties is detailed by Gay [56].

For aluminium rims:

$$\overline{k}_{sr} = \frac{k_{steel} + k_{aluminium}}{2} \;,\; \overline{k}_{rt} = \frac{k_{aluminium} + k_{rubber}}{2}$$

For CFRP rims:

$$\overline{k}_{sr} = \frac{k_{steel} + k_{composite}}{2} \;,\; \overline{k}_{rt} = \frac{k_{composite} + k_{rubber}}{2}$$

Heat is transmitted from the brake to the rim by conduction, convection and radiation and therefore:

$$U_{sr} = \overline{k}_{sr} \left(\frac{A_c}{L_e} \right)_{sr} + (h_e A_s)_{sr}$$

However, there is not enough information to solve for two unknowns and so convection and radiation from the brake to the rim is neglected. Approximations for $^{A_c}/_{L}$ were calculated from the optimised values of U_{sr} and U_{rt}. These results were then averaged for dual and single rims. U_{ra}, U_{ta} and $(m \cdot C_p)_t$ are estimated by taking averages for dual and single wheels. The results of this process are summarised in Table 6.6.

6 Results and Discussion

6.1 Finalised Lumped Mass Models

The finalised model parameters for the four wheel configurations are listed in Table 6.1. These are not the correct numerical values which correspond exactly to the physical properties of the system. Since Equation 2.9 is underdetermined, there are infinitely many solutions which will balance the net heat transfer of each component. The optimisation will also be affected by experimental errors as well as the specified solution intervals. Nevertheless, these values give insight into and understanding of the comparative heat transfer characteristics of each wheel configuration, which is discussed in Section 6.3.

The finalised model parameters were input into state-space models for each wheel and the power-averaged temperature responses calculated. These results are plotted with the power-averaged experimental data in Figure 6.1 to Figure 6.4. The graphs are accompanied by error plots where error was calculated as a percentage of the experimental value.

The *RMSE*s for each curve and model were calculated and listed in Table 6.2. The overall *RMSE*s are all within 5%, which indicates good agreement with the experimental results. The lumped mass models are therefore valid for calculating the temperature response of the wheel assemblies to the averaged braking powers. It is shown in Section 6.2 and Appendix A that this validity extends to the individual braking powers.

Table 6.1: Finalised Lumped Mass Model Parameters.

Parameter	Unit	Dual, Steel	Dual, Aluminium	Single, Steel	Single, Aluminium
U_{ba}	$W/^{\circ}C$	14.99			
U_{sb}	$W/^{\circ}C$	2.026			
U_{sa}	$W/^{\circ}C$	5.403			
U_{sr}	$W/^{\circ}C$	12.69	15.70	17.45	19.03
U_{rt}	$W/^{\circ}C$	14.00	15.15	8.687	20.45
U_{ra}	$W/^{\circ}C$	13.81	7.103	9.862	4.567
U_{ta}	$W/^{\circ}C$	53.07		31.32	
$(m \cdot C_p)_b$	$kJ/^{\circ}C$	56.80			
$(m \cdot C_p)_s$	$kJ/^{\circ}C$	54.71			
$(m \cdot C_p)_r$	$kJ/^{\circ}C$	28.21	52.55	23.22	24.40
$(m \cdot C_p)_t$	$kJ/^{\circ}C$	185.1	194.8	98.76	104.3
$Q_{hysteresis}$	W	697.1			
$Q_{friction}$	W	19.59			

Table 6.2: Model Percentage $RMSE$ (Averaged, $P_b \approx 2.5\ kW$).

Component	$RMSE$ (%)				
	Dual, Steel	Dual, Aluminium	Single, Steel	Single, Aluminium	Maximum
Axle Beam	1.1	1.2	1.1	1.1	1.2
Brake Shoe	6.2	5.8	6.1	5.8	6.2
Rim	3.7	2.9	4.0	2.0	4.0
Tyre	3.0	1.0	1.0	4.0	4.0
Overall	3.9	3.3	3.7	3.7	3.9

There is disagreement between the measured and modelled brake shoe temperature, particularly when $t < 30\ min$. This error is a consequence of taking measurements

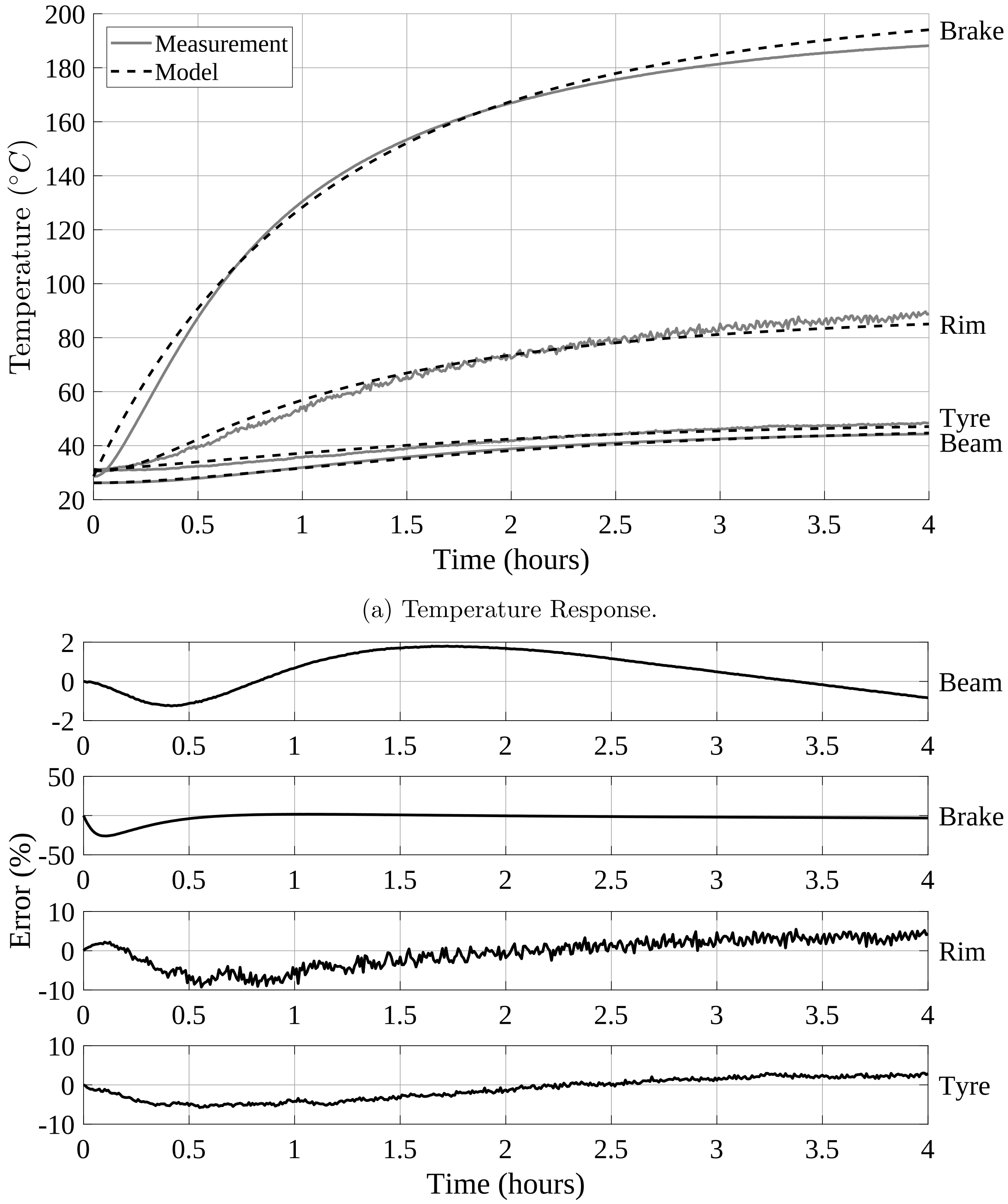

(a) Temperature Response.

(b) Model Errors.

Figure 6.1: Modelling Results (Averaged, Dual, Steel, $P_b \approx 2.5\ kW$).

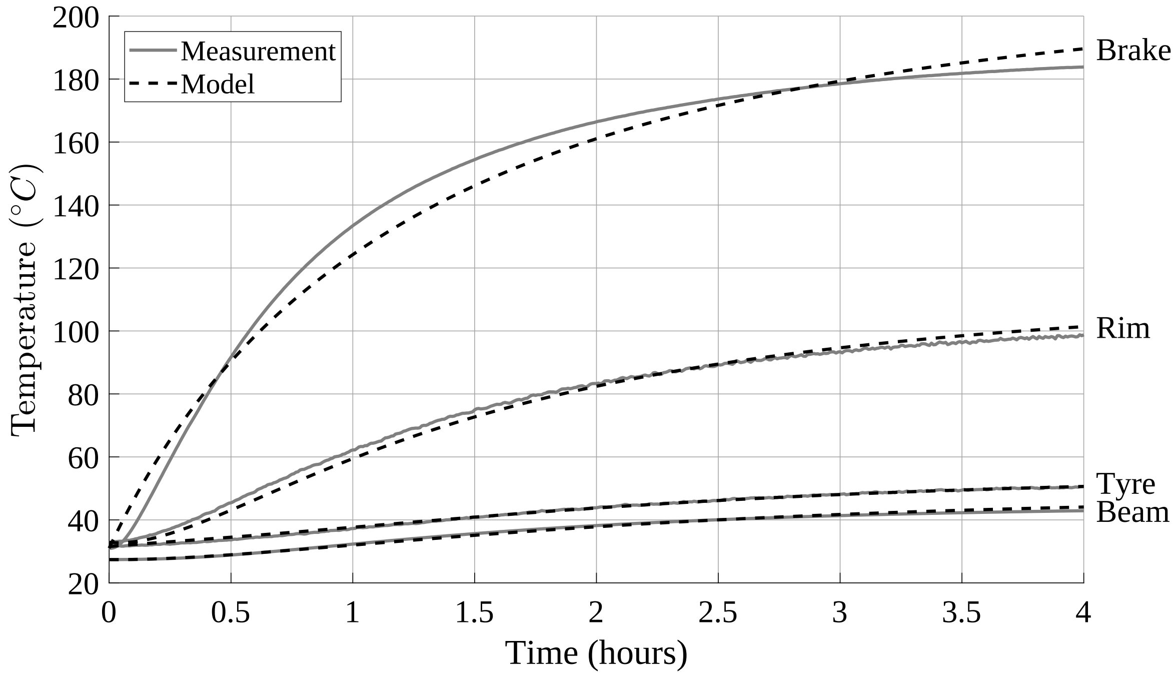

(a) Temperature Response.

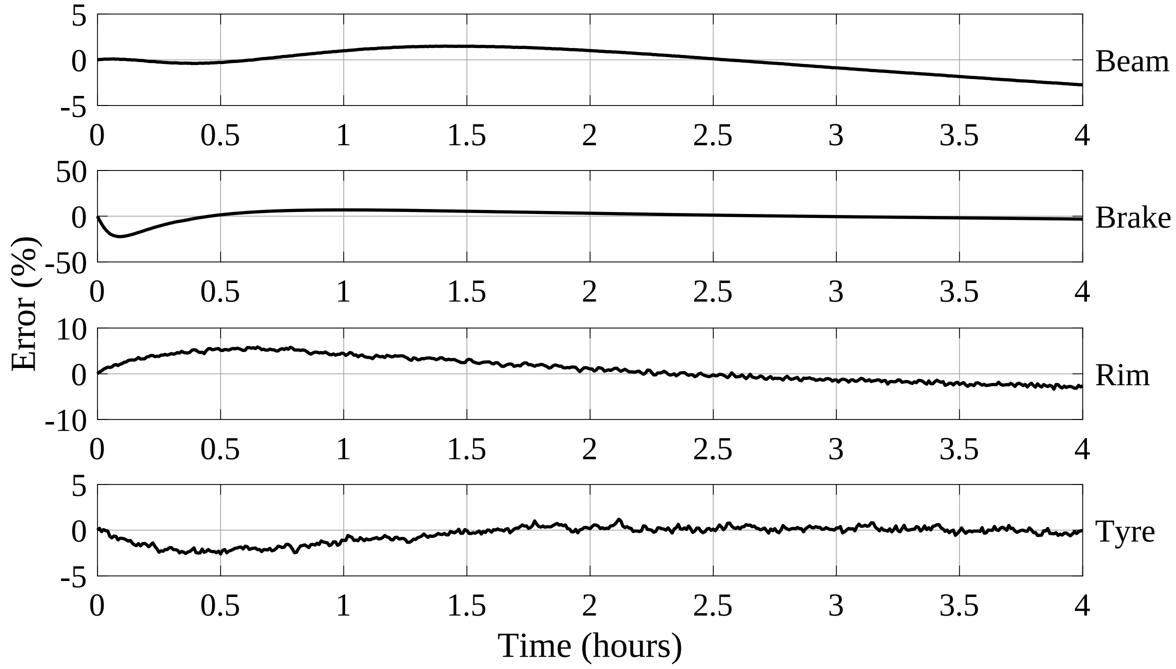

(b) Model Errors.

Figure 6.2: Modelling Results (Averaged, Dual, Aluminium, $P_b \approx 2.5\ kW$).

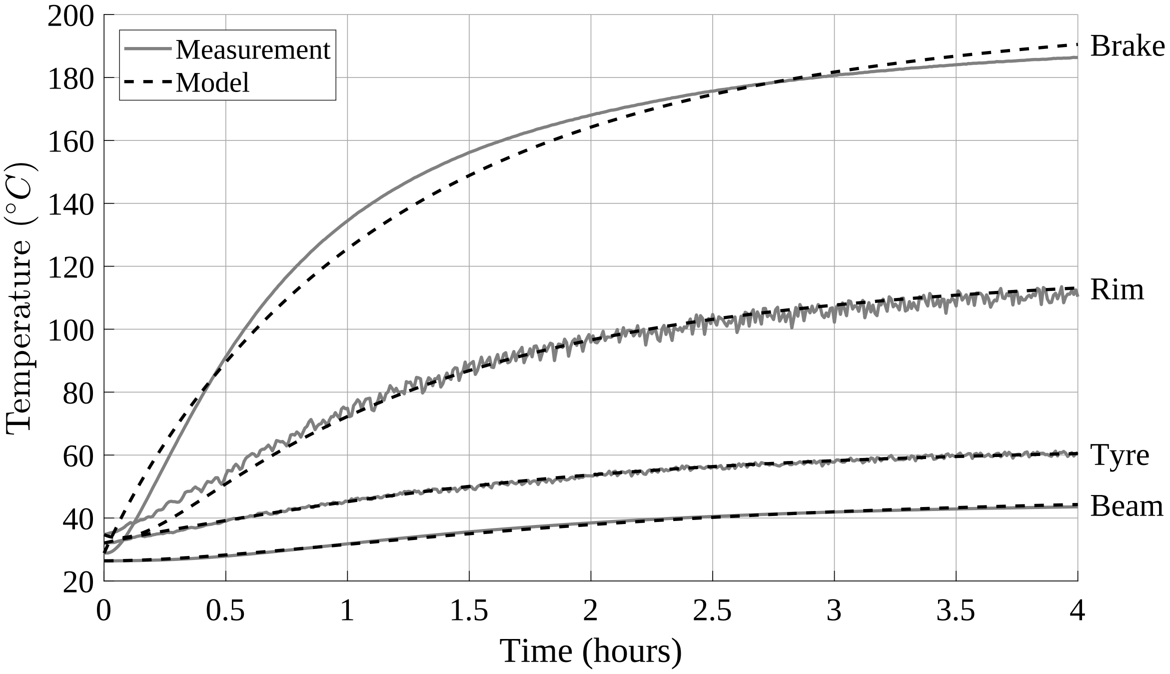

(a) Temperature Response.

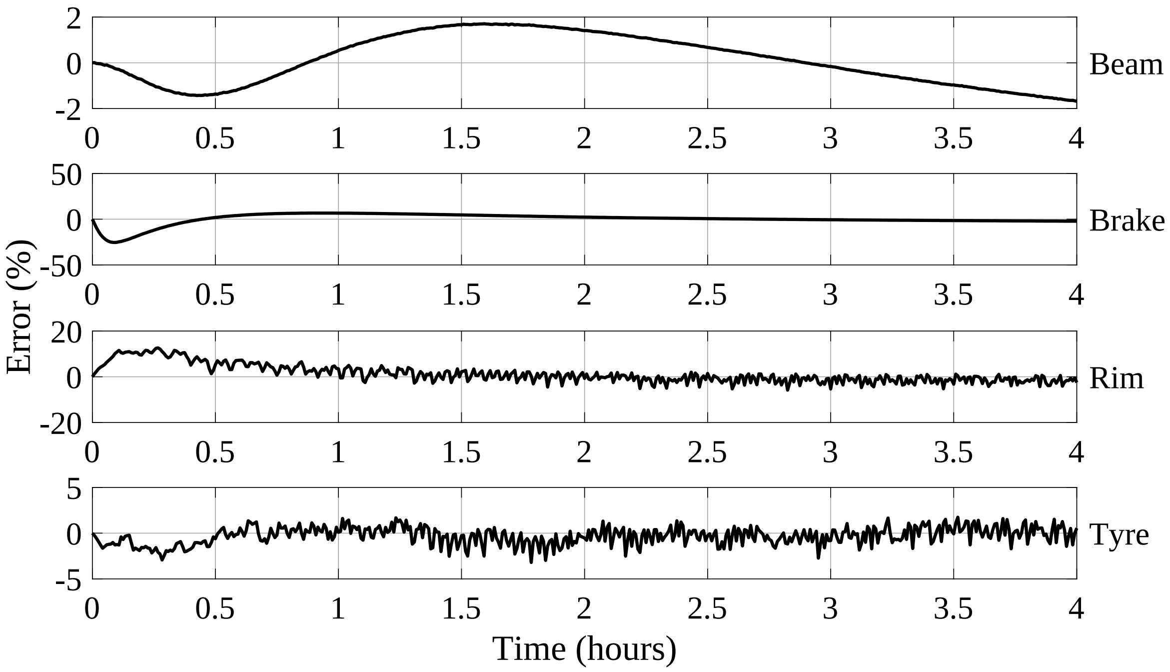

(b) Model Errors.

Figure 6.3: Modelling Results (Averaged, Single, Steel, $P_b \approx 2.5\ kW$).

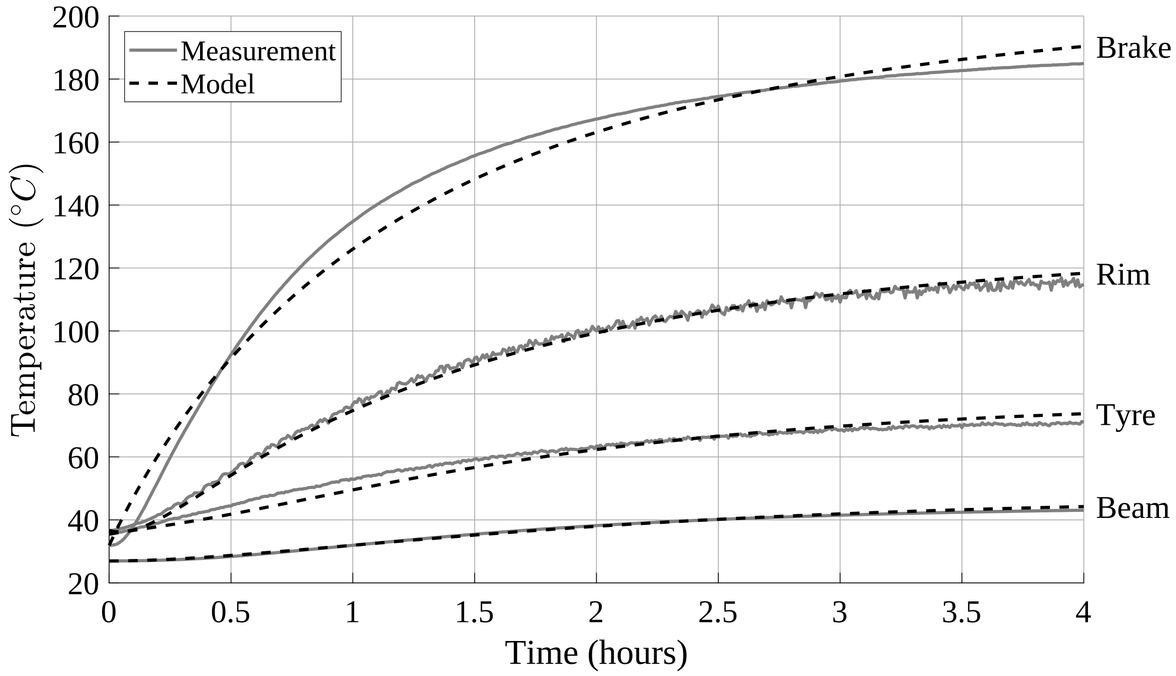

(a) Temperature Response.

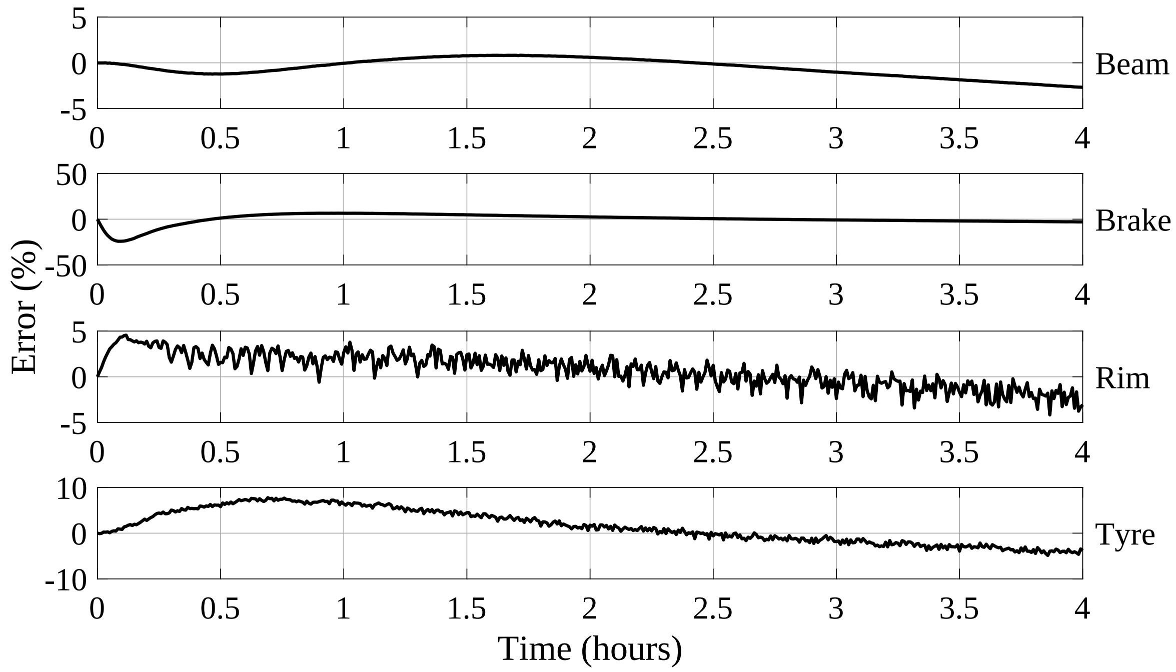

(b) Model Errors.

Figure 6.4: Modelling Results (Averaged, Single, Aluminium, $P_b \approx 2.5\ kW$).

at the inner edge of the brake shoe, since the temperature change must first propagate from the friction surface and through the thickness of the brake shoe before it is measured by the thermocouple.

The model, however, outputs the average brake shoe temperature which will begin to rise immediately after the brakes are applied and is consequently a first-order response. This error can be removed by separating the brake shoe temperature and the heat source in the lumped mass model. Introducing a virtual sensor - denoted by the subscript v - gives Equation 6.1.

$$\mathbf{B_v} \cdot \dot{\mathbf{T}}_\mathbf{v}(t) + \mathbf{A_v} \cdot \mathbf{T_v}(t) = \mathbf{C_v}(t) \tag{6.1}$$

Where:

$$\mathbf{A_v} = \begin{bmatrix} U_{ba} + U_{sb} & -U_{sb} & 0 & 0 & 0 \\ -U_{sb} & U_{sb} + U_{vs} + U_{sa} & -U_{vs} & 0 & 0 \\ 0 & -U_{vs} & U_{vs} + U_{vr} + U_{va} & -U_{vr} & 0 \\ 0 & 0 & -U_{vr} & U_{vr} + U_{ra} + U_{rt} & -U_{rt} \\ 0 & 0 & 0 & -U_{rt} & U_{rt} + U_{ta} \end{bmatrix}$$

$$\mathbf{B_v} = \begin{bmatrix} (m \cdot C_p)_b & 0 & 0 & 0 & 0 \\ 0 & (m \cdot C_p)_s & 0 & 0 & 0 \\ 0 & 0 & (m \cdot C_p)_v & 0 & 0 \\ 0 & 0 & 0 & (m \cdot C_p)_r & 0 \\ 0 & 0 & 0 & 0 & (m \cdot C_p)_t \end{bmatrix}$$

$$\mathbf{C_v}(t) = \begin{bmatrix} T_\infty \cdot U_{ba} + Q_{friction} \\ T_\infty \cdot U_{sa} \\ T_\infty \cdot U_{va} + P_b(t) \\ T_\infty \cdot U_{ra} \\ T_\infty \cdot U_{ta} + Q_{hysteresis} \end{bmatrix}, \quad \dot{\mathbf{T}}_\mathbf{v}(t) = \begin{bmatrix} \dot{T}_b(t) \\ \dot{T}_s(t) \\ \dot{T}_v(t) \\ \dot{T}_r(t) \\ \dot{T}_t(t) \end{bmatrix}, \quad \mathbf{T_v}(t) = \begin{bmatrix} T_b(t) \\ T_s(t) \\ T_v(t) \\ T_r(t) \\ T_t(t) \end{bmatrix}$$

Optimised parameters for Equation 6.1 were determined and the resulting temperature response of the dual, aluminium wheel plotted in Figure 6.5. Adding this fifth degree-of-freedom (DoF) produces the required delayed first-order temperature response at the brake shoe with a maximum error of 8%.

Although this model exhibits improved agreement with the experimental data, the physics of the system are well described by Equation 2.9. The delayed first-order

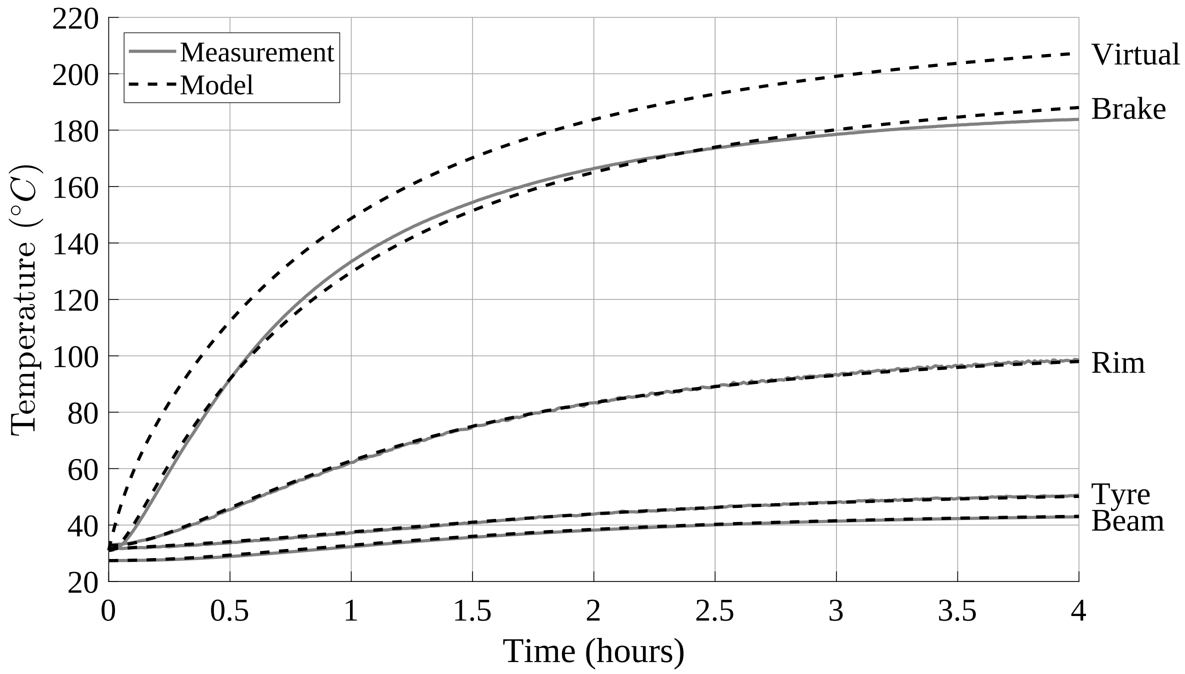

(a) Temperature Response.

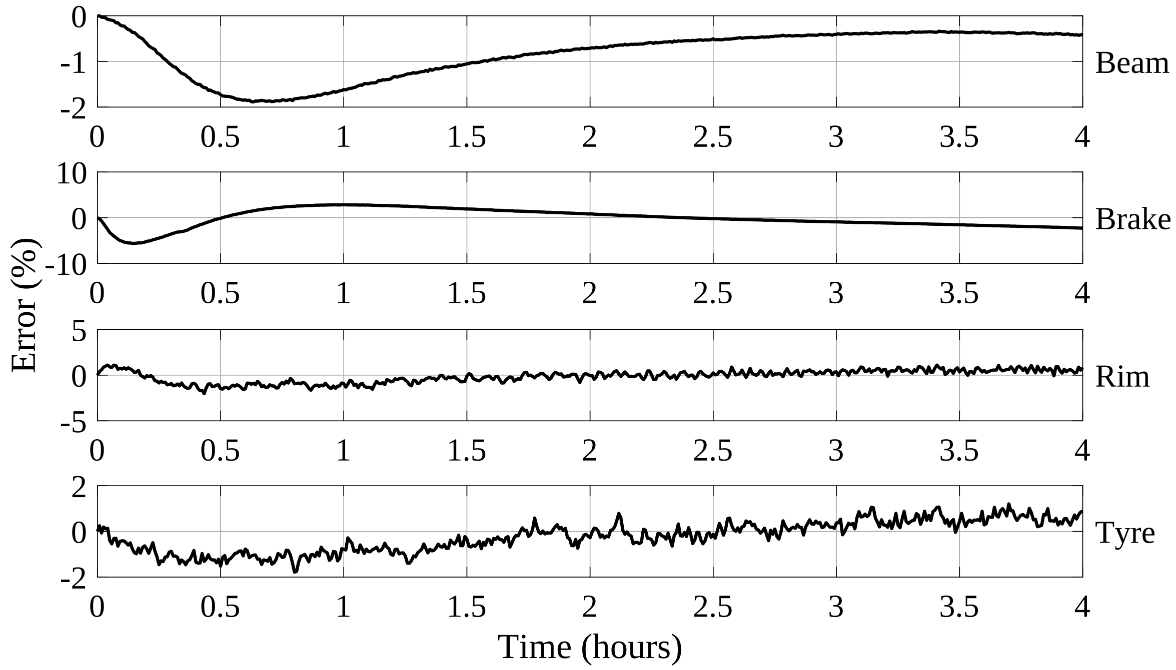

(b) Model Errors.

Figure 6.5: Five DoF Modelling Results (Averaged, Dual, Aluminium, $P_b \approx 2.5\ kW$).

response of the brake shoe temperature is observed due to the physical limitations in measurement capabilities of not being able to place the thermocouple closer to the point where the temperature first increases. The errors do not necessitate alteration of the model since the source of error is understood.

A value of $(m \cdot C_p)_s = 17.34\ ^{kJ}/_{°C}$ was obtained for Equation 6.1. For a predominantly steel brake assembly (shoe and drum) with $C_p = 434\ ^{J \cdot kg}/_{°C}$, the corresponding mass is approximately 40 kg which is a reasonable estimate. For the four DoF models where the inner brake shoe temperature is used to represent the shoe and drum, $(m \cdot C_p)_s = 54.71\ ^{kJ}/_{°C}$ and therefore $m = 127\ kg$ which is impractically high. This results from the optimisation attempting to increase the thermal inertia of the shoe and drum to slow the temperature rise and thereby compensate for the time taken for the heat to propagate through to the thermocouple on the inner surface of the shoe.

6.2 System Linearity

It was assumed in Section 5 that the temperature curves could be averaged to reduce experimental error and improve computation speed. The consequences of this assumed linearity or scaling of the temperature responses with braking power is discussed in this section.

The temperature responses of each wheel for $P_b \approx 1\ kW - 4\ kW$ were calculated and are plotted in Figure A.1 to Figure A.16 (see Appendix A). The average percentage $RMSE$s, $\overline{E}$, for the four wheels at different braking powers are listed with their corresponding standard deviations, σ, in Table 6.3. For the axle beam, rim and tyre temperatures there is good agreement between measured and modelled results across all braking powers with average $RMSE$ values of less than 6%. There are instances of higher disagreement (up to 18%), however these are uncommon and are attributed to experimental error. The standard deviations show that the majority of $RMSE$s are within close proximity to the average and are therefore acceptable.

The models consistently underpredict brake temperature for lower braking powers and overpredict brake temperature for higher braking powers. This error arises from the linear approximation of radiative cooling (Equation 2.2), which is illustrated using Figure 6.6, where it is assumed that radiation and convection each account for 50% of heat transfer from the brake to the surroundings. For $P_b = 2.5\ kW$, the final brake

Table 6.3: Lumped-Mass Modelling Error Metrics for Various Braking Powers.

P_b	Error Metric (%)									
	Axle Beam		Brake Shoe		Rim		Tyre		Overall	
(kW)	$\overline{E}$	σ	$\overline{E}$	σ	$\overline{E}$	σ	$\overline{E}$	σ	$\overline{E}$	σ
1	1.3	0.89	8.0	5.7	4.8	4.1	6.6	5.1	5.2	4.7
2	3.4	4.0	7.7	1.6	5.0	1.7	5.9	3.0	5.5	2.9
3	1.6	0.70	6.1	2.4	3.9	2.1	3.0	0.6	3.7	2.2
4	2.4	1.2	8.8	3.7	6.3	1.2	5.7	3.3	5.8	3.3
Overall	2.2	2.1	7.6	3.4	5.0	2.4	5.3	3.3	5.0	3.4

temperatures are between 147 $°C$ and 152 $°C$. The higher-order curve which, at 150 $°C$, gives the same rate of heat transfer as the linear approximation is also plotted.

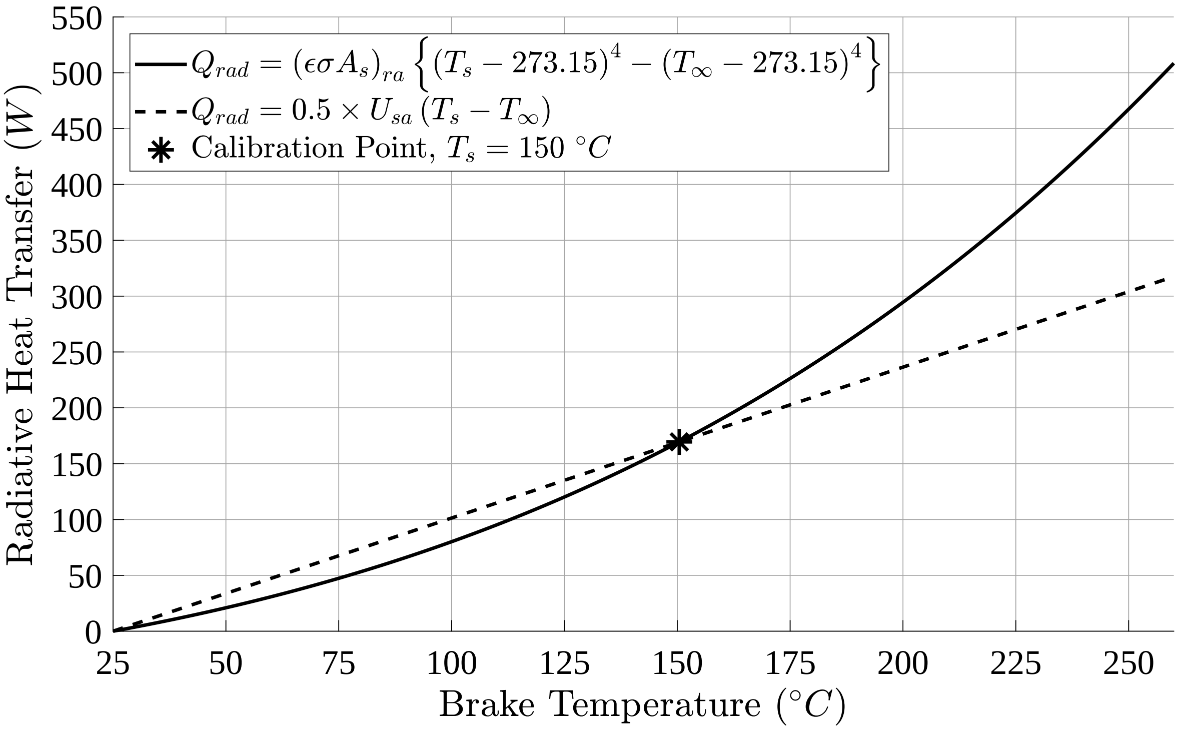

Figure 6.6: Linear versus Exponential Radiative Cooling ($T_\infty = 25$ $°C$).

Radiative heat transfer is a function of temperature difference to the fourth power and is thus a nonlinear phenomenon. At lower temperatures, the linear equation over-predicts radiative cooling and so the true temperature of the brake is higher than calculated by the models. At higher temperatures, this relationship is reversed as the effects of radiation become exponentially greater. The models are optimised around the temperature response to the mean braking power and will therefore overpredict the temperature rise for $P_b > 2.5\ kW$.

Although radiation is nonlinear, a linear approximation is sufficiently accurate. Since radiative cooling in the brake is independent of the rim material and wheel configuration, the error arising from linearising radiation is common to each wheel and does not affect the qualitative comparison of the temperature responses. The quantitative results for brake temperature are also valid when predicting overheating. Between experimental temperatures of 120 $°C$ and 235 $°C$, the models are accurate to within 12% (less than 15 $°C$ − 30 $°C$). High accuracy in this region is important since brake fade is known to begin around 120 $°C$. Beyond 235 $°C$ the brake temperature is overpredicted which prematurely indicates danger. The models are therefore conservative in predicting brake overheating.

6.3 Impact of Wheel Configuration on Component Heating

6.3.1 Steady State Conditions

The steady state temperature increases ($\Delta T_{ss},\ °C$) of each component for $P_b = 2.5\ kW$ are listed in Table 6.4. For a given rim material, there are no appreciable differences in axle beam and brake shoe temperatures between single and dual configurations. However, steel-rimmed configurations exhibit slightly higher temperature increases than the aluminium-rimmed do; 0.910 $°C$ (5.0%) and 3.05 $°C$ (1.9%) on average for the axle beam and brake shoe respectively. The maximum difference in brake temperature increase is 3.3 $°C$ (2.1%) between the single, steel and single, aluminium wheels where the steel-rimmed wheel's brake is hotter than the aluminium-rimmed wheel's brake. These differences are minor and therefore wheel configuration and rim material are unlikely the dominant contributing factor to brake or axle overheating.

Rim temperature increase is, on average, 18.9 $°C$ (33%) higher for single wheels than for duals and 10.9 $°C$ (19%) higher for aluminium rims than for steel. The maximum difference in rim temperature increase is therefore 29.8 $°C$ (56%) between the single, aluminium wheel and the dual, steel wheel where the single, aluminium rim is hotter than the dual, steel rim. While the differences in temperatures are substantial, no rim is close to exceeding its safe operating temperature and thus rim longevity is not impacted.

Table 6.4: Steady State Component Temperature Increase ($P_b = 2.5\ kW$).

Component	ΔT_{ss} ($^{\circ}C$)			
	Dual, Steel	Dual, Aluminium	Single, Steel	Single, Aluminium
Axle Beam	19.42	18.19	19.31	18.72
Brake Shoe	160.0	157.2	160.3	157.0
Rim	52.90	70.69	78.71	82.72
Tyre	17.13	21.12	29.58	40.29

Tyre temperature increase is, on average, 15.8 $^{\circ}C$ (82%) higher for single wheels than for duals and 7.35 $^{\circ}C$ (30%) higher for aluminium rims than for steel. The maximum difference in average tyre temperature increase is therefore 23.2 $^{\circ}C$ (135%) between the single, aluminium wheel and the dual, steel wheel where the single, aluminium tyre is hotter than the dual, steel tyres. Aluminium rims therefore contribute to higher tyre temperatures in comparison to steel rims for alpine braking. Similarly, single wheel tyres will run hotter than dual wheel tyres. The maximum allowable temperature of rubber (90 $^{\circ}C$) is lower than the maximum allowable temperatures of steel or aluminium and therefore the differences between tyre temperatures for different configurations and rim materials is significant. The severity of these differences is discussed further in Section 6.4.

6.3.2 Heat Transfer Characteristics

The inter-component heat transfers at steady state (Q_{ss}, W) for the four wheel configurations are listed in Table 6.5. The differences in Q_{sb}, Q_{sr}, Q_{ba} and Q_{sa} between any of the configurations are all less than 1%. However, $(U_{sr})_{Aluminium} > (U_{sr})_{Steel}$ due to the higher thermal conductivity of aluminium which facilitates greater conduction of braking heat into the rim. This indicates that a steeper temperature gradient is needed between the brake and the steel rims than between the brake and aluminium rims for the same quantity of heat to be conducted because $Q_{sr} = U_{sr}\,(T_s - T_r)$. Thus the brake temperature is higher and the rim temperature is lower for steel rims. These differences are however inconsequential in terms of brake and rim overheating.

Q_{rt} is, on average, 352 W (75%) higher for aluminium rims than for steel. This occurs because the aluminium rims reach higher temperatures than the duals and $(U_{rt})_{Aluminium} > (U_{rt})_{Steel}$ owing to the higher thermal conductivity of aluminium in

Table 6.5: Inter-Component Heat Transfer at Steady State ($P_b = 2.5\ kW$).

Interaction	Symbol	Q_{ss} (W) Dual, Steel	Dual, Aluminium	Single, Steel	Single, Aluminium
Shoe - Beam	Q_{sb}	289.8	289.0	290.7	290.4
Shoe - Rim	Q_{sr}	1326	1329	1322	1324
Rim - Tyre	Q_{rt}	509.6	771.1	450.0	892.6
Beam - Air	Q_{ba}	309.4	308.6	310.3	309.9
Shoe - Air	Q_{sa}	884.2	881.9	887.1	885.9
Rim - Air	Q_{ra}	816.4	558.0	872.1	431.1
Tyre - Air	Q_{ta}	1207	1468	1147	1590

comparison to steel. The aluminium rims are also twice the thickness of the steel rims at the hub and up to 3.5 times as thick at the dish. This gives aluminium rims a greater ratio of cross-sectional area to effective length and therefore a higher overall U_{rt} because $U_{rt} = \overline{k}_{rt}\left({}^{A_c}/_{L_e}\right)_{rt}$. Tyre temperatures are therefore lower for the steel rim configurations. The lower the rim temperature or value of U_{rt}, the lower the tyre temperature must be to facilitate the Q_{rt} listed in Table 6.5. Accordingly, the steel rims' tyre temperatures are lower than for the aluminium rims as the steel rims are cooler and conduct heat less effectively.

The heat convected from the rim to the air, Q_{ra}, is, on average, 350 W (74%) higher for steel rims than for aluminium. This is a consequence of higher overall heat transfer coefficients between the steel rims and the ambient air than between the aluminium rims and the air; i.e. $(U_{ra})_{steel} > (U_{ra})_{aluminium}$. Heat must first be conducted through the rim before being convected to the air. U_{ra} is therefore influenced by both convective and conductive heat transfer parameters such that:

$$U_{ra} = (h_e A_s)_{ra} + k_r \left(\frac{A_c}{L_e}\right)_r$$

The higher the surface area, the higher U_{ra} and therefore $(U_{ra})_{dual} > (U_{ra})_{single}$ for a given rim material because the dual rims have a higher combined surface area than the singles. For a given configuration, $(U_{ra})_{steel} > (U_{ra})_{aluminium}$ which is unexpected since $k_{steel} < k_{aluminium}$. However, the aluminium rims are between two and four times thicker than the steel rims. The effective conductive length for analysing heat transfer from the rim to the air is therefore higher for aluminium rims than for steel, so much so that the increased thermal conductivity of the aluminium is cancelled out. This explains why steel rims convect heat to the air more effectively than aluminium rims.

The heat transfer characteristics of the rims are best understood when U_{ra} and U_{rt} are considered together, as $(U_{rt})_{steel} < (U_{rt})_{aluminium}$ and $(U_{ra})_{steel} > (U_{ra})_{aluminium}$. This indicates that steel rims convect a greater proportion of heat to the air and conduct a lesser proportion of heat to the tyres than aluminium rims do. The additional heat which is transmitted to the tyres by the aluminium rims must be removed by convection to the air. Therefore, $(Q_{ta})_{steel} > (Q_{ta})_{aluminium}$. However, U_{ta} is the same for both of the dual wheels and for both of the single wheels and so the aluminium rims' tyres must rise to a higher temperature to dissipate more heat.

$(U_{ta})_{dual} > (U_{ta})_{single}$ owing to the two additional sidewalls of the dual wheel tyres which increase their convective surface area in comparison to the singles. Assuming an equal Q_{rt}, the temperature of the single wheel tyres must be higher to convect heat such that $Q_{rt} = Q_{ta}$ $(Q_{in} = Q_{out})$. The wheel configuration (dual versus single) has the highest impact on tyre temperature, since the resulting difference in temperature increase is 82%, whereas aluminium rims cause tyre temperature increases 30% higher than steel rims do.

6.4 Maximum Tyre Temperature

From the results in Table 6.4, aluminium rims and single wheels will experience higher average tyre temperatures for alpine braking. However, the highest tyre temperature observed during testing was 83.13 $°C$ (measured) or 91.36 $°C$ (modelled). Tyre degradation is known to begin between 90 $°C$ – 120 $°C$, which implies that the tyres of all four configurations were roughly within acceptable limits during testing.

By plotting the radial temperature distribution in the tyre, it can be seen that the temperature decays exponentially from a maximum at the bead (0% radial position) to a minimum at the tread (100% radial position). Figure 6.7 shows the temperature distribution in the single, aluminium rim tyre for $P_b \approx 4\ kW$ which are the same test conditions which gave rise to a 83.13 $°C$/91.36 $°C$ final average tyre temperature. At the end of the test, the maximum tyre temperature rose by 100 $°C$ – 120 $°C$ while the average temperature had increased by less than 60 $°C$. Regions of the single, aluminium rim tyre were therefore above the upper threshold for tyre degradation.

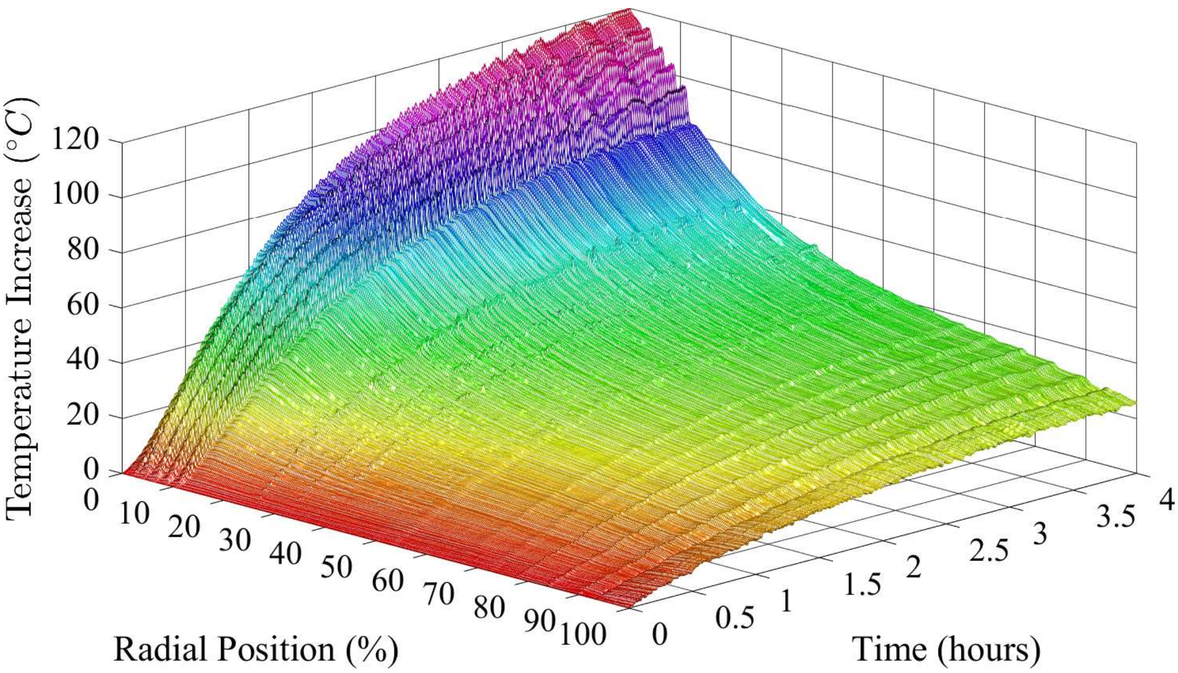

Figure 6.7: Radial Tyre Temperature Distribution (Single, Aluminium, $P_b \approx 4\ kW$).

The maximum tyre temperature increases for each test were plotted and a second-order curve fitted to the results. The responses were averaged and normalised per unit braking power to produce the curves shown in Figure 6.8[xiii]. The dual, steel wheels undergo the lowest maximum temperature change per kilowatt of braking power, while the maximum tyre temperature increase of the dual, aluminium wheels is 14% ($1.70\ ^\circ C - 6.80\ ^\circ C$) higher for $P_b = 1\ kW - 4\ kW$. The single, aluminium tyre's maximum temperatures rose 18% ($3.80\ ^\circ C - 15.2\ ^\circ C$) more than the single, steel tyre's across the same braking power range. The maximum temperature increases of the single wheel tyres are 80% ($9.50\ ^\circ C - 38.0\ ^\circ C$) higher for the steel rims and 85% ($11.6\ ^\circ C - 46.4\ ^\circ C$) higher for the aluminium rims in comparison to the dual wheels. The greatest differences in maximum tyre temperature, $13.3\ ^\circ C - 53.2\ ^\circ C$, therefore arise between the single, aluminium wheel and the dual, steel wheel.

On average, the maximum tyre temperature increase of aluminium-rimmed wheels is 16% higher than that of the steels-rimmed wheels, and the maximum tyre temperature increase of single wheels is 83% higher than that of dual wheels. As with average tyre temperature, the higher thermal conductivity and cross-sectional areas of the aluminium rims is responsible for the increased maximum tyre temperatures compared to the steel-rimmed wheels since more heat is conducted into the tyre which must then be convected to the ambient air. Heat conducted into the tyre is distributed

[xiii] A complete description of the maximum tyre temperature models can be found in Appendix C.

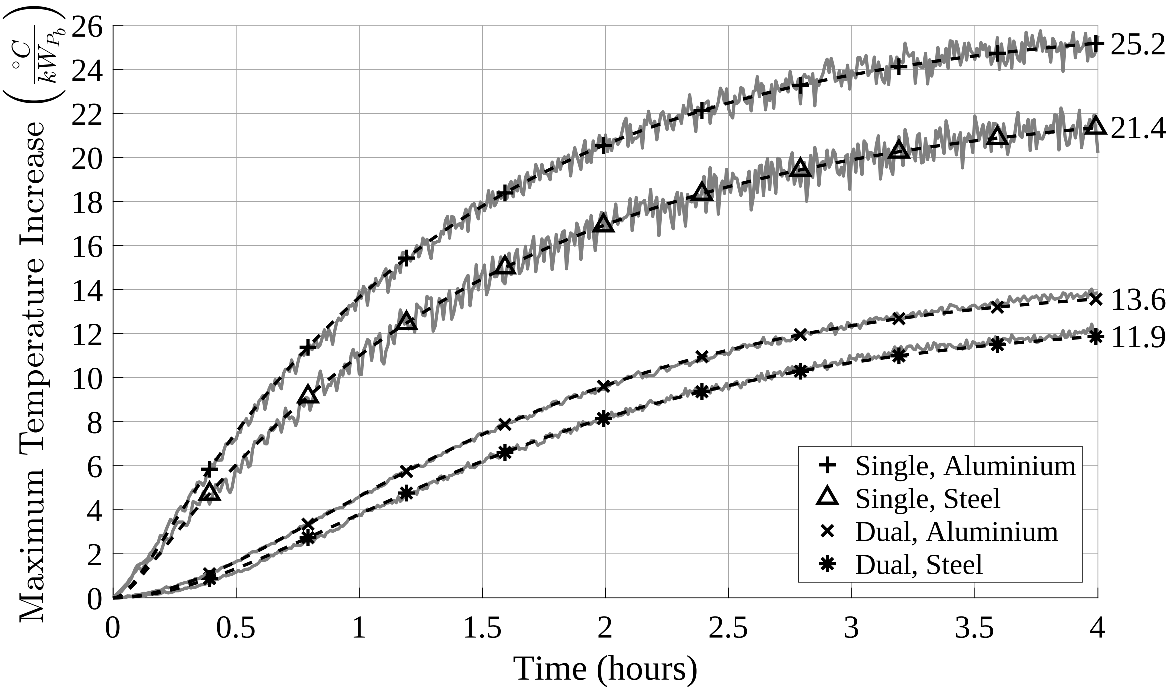

Figure 6.8: Normalised Maximum Tyre Temperature Increase ($\overline{T}_i = 32\ °C$).

between the sidewalls, and so each sidewall of the dual wheel tyres conducts less heat through its length and convects less heat from its surface than the single wheel tyres do. Consequently, the temperature gradient between the bead and tread is lower for the dual wheel tyres than the singles, as is the temperature gradient between the maximum temperature region and the ambient air.

While aluminium rims increase the maximum tyre temperature, the difference is smaller in comparison to that between the dual and single configurations. Under operating conditions which are acceptable for dual wheels, regions of the single wheel tyres are likely to be at temperatures above safe thresholds. Single wheels are therefore at a higher risk of experiencing blowout, which is exacerbated by using aluminium rims in place of steel.

This conclusion is however limited by the difficulty of measuring the temperature in the middle sidewalls of the dual wheels. Contact sensors are either not suitable for capturing temperature distribution or impractical to use on continuously rotating objects. Neither of these restrictions apply to non-contact sensors such as a thermal imaging camera, however these instruments require a unobstructed line of sight facing perpendicular to the surface being measured.

Figure 6.9 depicts the locations where blowout is likely to occur. The subscripts s, d, o, i and m denote *single, dual, outer, inner* and *middle* respectively. Assuming that the rim temperature decreases from a maximum where the drum and rim meet, then $T_{s,i} > T_{s,o}$ and $T_{d,m} > T_{d,i} > T_{d,o}$. It is likely that the true maximum tyre temperature of the dual wheels is higher than what was measured and thus the difference between the two configurations is less pronounced than what the results from this study show.

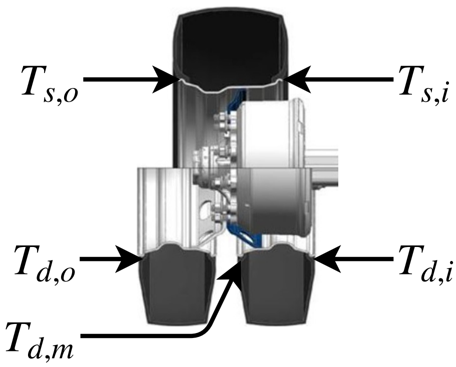

Figure 6.9: Critical Temperature Locations of Dual and Single Wheel Tyres.

6.5 Thermal Response of CFRP-Rimmed Wheel Assemblies

Table 6.6 details the approximation of the parameters for the CFRP rims. From these results, the final conductive parameters for the CFRP rims were estimated (Table 6.7) and lumped mass models built for CFRP rims in both dual and single configurations (Table 6.8).

Using the average initial temperatures observed during testing, the temperature responses of the CFRP rims were calculated for $P_b = 2.5\ kW$ and the results plotted in Figure 6.10a for a dual wheel and Figure 6.10b for a single wheel.

The steady state component temperature increases for the CFRP wheels were calculated and listed in Table 6.9. As with steel and aluminium rims, there is negligible difference in the axle beam and brake shoe temperatures between dual and single wheels. The single wheel exhibits rim and tyre temperature increases $34.7°C$ (53%) and $9.80\ °C$ (151%) higher than the dual wheel. These results are consistent with those obtained for steel and aluminium rims, and are explained by the same mechanisms.

Table 6.6: Estimation of CFRP Rim Properties.

	Parameter	Unit	Dual, Steel	Dual, Aluminium	Single, Steel	Single, Aluminium
	U_{sr}	$W/{}^\circ C$	12.69	15.70	17.45	19.03
	$\overline{k}_{sr}$	$W/m\cdot{}^\circ C$	60.50	144.8	60.50	144.8
	$\left(A_c/L_e\right)_{sr}$	m^2/m	0.2097	0.1085	0.2885	0.1315
$\longrightarrow$	$\left(\overline{A_c/L_e}\right)_{sr}$	m^2/m	0.1591		0.2100	
	U_{rt}	$W/{}^\circ C$	14.00	15.15	8.687	20.45
	$\overline{k}_{rt}$	$W/m\cdot{}^\circ C$	30.41	114.7	30.41	114.7
	$\left(A_c/L_e\right)_{rt}$	m^2/m	0.4605	0.1321	0.2857	0.1784
$\longrightarrow$	$\left(\overline{A_c/L_e}\right)_{rt}$	m^2/m	0.2963		0.2320	
	U_{ra}	$W/{}^\circ C$	13.81	7.103	9.862	4.567
$\longrightarrow$	$\overline{U}_{ra}$	$W/{}^\circ C$	10.45		7.215	
	$(m\cdot C_p)_t$	$kJ/{}^\circ C$	185.1	194.8	98.76	104.3
$\longrightarrow$	$\left(\overline{m\cdot C_p}\right)_t$	$kJ/{}^\circ C$	189.9		101.5	

Table 6.7: Estimated Conductive Heat Transfer Parameters of CFRP Rims.

Parameter	Unit	Dual	Single
$\left(A_c/L_e\right)_{sr}$	m^2/m	0.1591	0.2100
$\overline{k}_{sr}$	$W/m\cdot{}^\circ C$	32.42	
$\left(A_c/L_e\right)_{rt}$	m^2/m	0.2963	0.2320
$\overline{k}_{rt}$	$W/m\cdot{}^\circ C$	2.322	

Table 6.8: CFRP-Rimmed Wheel Model Parameters.

Parameter	Unit	Dual	Single
U_{ba}	$W/°C$	14.99	
U_{sb}	$W/°C$	2.026	
U_{sa}	$W/°C$	5.403	
U_{sr}	$W/°C$	5.157	6.807
U_{rt}	$W/°C$	0.6882	0.5389
U_{ra}	$W/°C$	10.45	7.215
U_{ta}	$W/°C$	53.07	31.32
$(m \cdot C_p)_b$	$kJ/°C$	56.80	
$(m \cdot C_p)_s$	$kJ/°C$	54.71	
$(m \cdot C_p)_r$	$kJ/°C$	19.68	11.16
$(m \cdot C_p)_t$	$kJ/°C$	189.9	101.5
$Q_{hysteresis}$	W	697.1	
$Q_{friction}$	W	19.59	

Table 6.9: Steady State Component Temperature Increase (CFRP, $P_b = 2.5\ kW$).

Component	ΔT_{ss} $(°C)$	
	Dual	Single
Axle Beam	27.26	27.04
Brake Shoe	228.7	226.9
Rim	65.70	100.4
Tyre	6.507	16.31

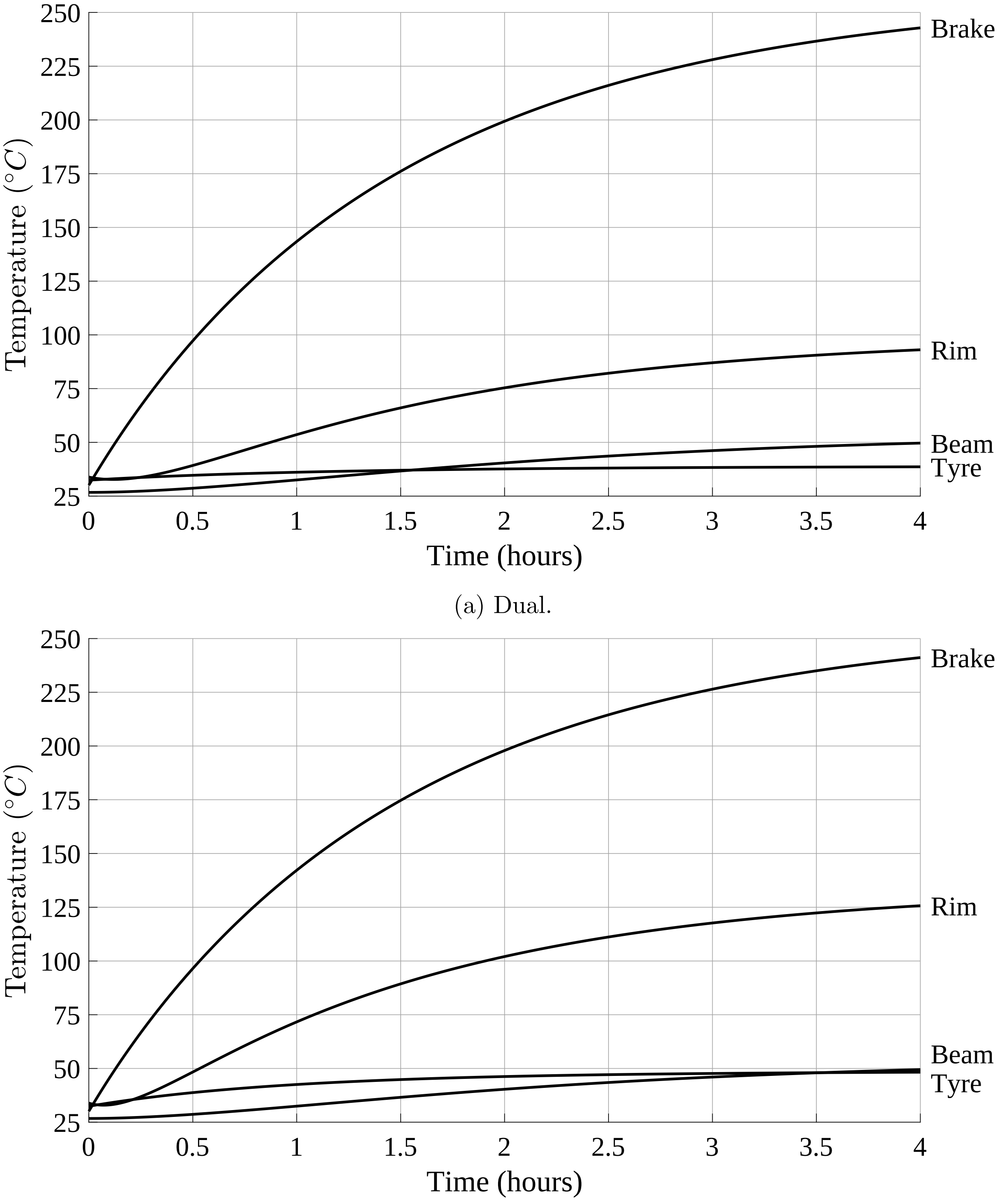

(a) Dual.

(b) Single.

Figure 6.10: CFRP-Rimmed Wheel Temperature Response ($P_b = 2.5\ kW$).

Figure 6.11a and Figure 6.11b compare the brake shoe temperature responses of the CFRP rims to those of the steel and aluminium rims in dual and single wheel configurations respectively. These responses were calculated using the same initial temperature for each wheel. For $t \leq 30\ min$, the brake temperature responses of the various wheels are similar. During this period, most of the heat being generated is absorbed by the brake which has the same thermal capacity regardless of which rim is used. Once the brakes reach a sufficiently high temperature (approximately 90 $°C$) the responses begin to diverge with the CFRP-rimmed wheels exhibiting higher temperatures for the remainder of the response. During this phase, the brakes are saturated and the dominant mechanisms of heat transfer are conduction through the rim and convection to the air.

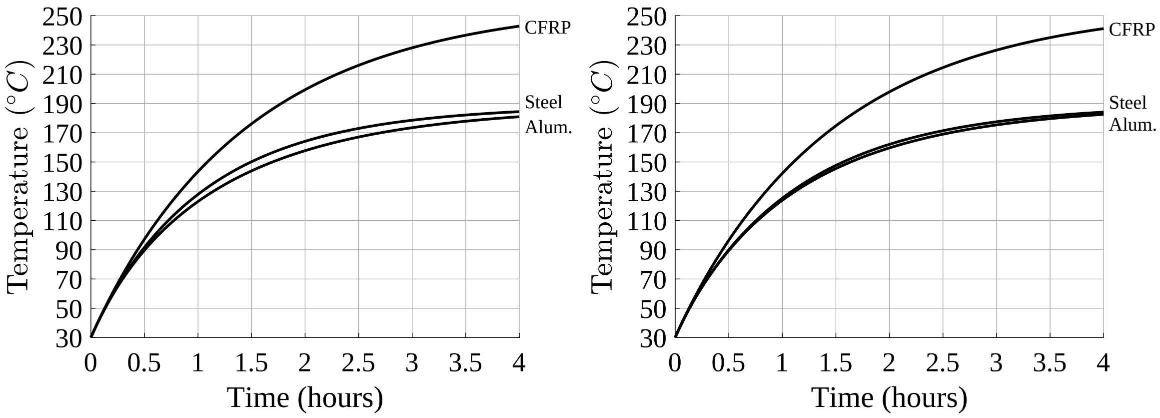

(a) Dual Wheels. (b) Single Wheels.

Figure 6.11: Comparison of Brake Shoe Temperature Responses ($P_b = 2.5\ kW$).

At steady state, the CFRP wheels' brake temperature increases are, on average, 67.7 $°C$ (42%) and 70.1 $°C$ (45%) higher than when using steel and aluminium rims respectively. The tyre temperature responses for dual and single wheels are compared in Figure 6.12. The steady state tyre temperature increase of the dual CFRP wheel is 10.6 $°C$ (62%) and 14.6 $°C$ (69%) lower than for the steel and aluminium rims respectively. The steady state tyre temperature increase of single CFRP wheel tyres is 13.3 $°C$ (45%) and 24.0 $°C$ (60%) lower than for steel and aluminium rims respectively. These results indicate that CFRP rims inhibit brake cooling and conduction of heat into the tyres.

The steady state inter-component heat transfers of the CFRP-rimmed wheel assembly were calculated and listed in Table 6.10. Q_{sr} is, on average, 497 W (38%) lower for CFRP rims than for steel or aluminium rims. This is attributed to the thermal conductivity of the CFRP, which is approximately 14 and 53 times lower than that of steel and aluminium respectively, and therefore inhibits conduction of heat out of the brake and into the rim. Consequently, the brakes of the CFRP-rimmed wheel must

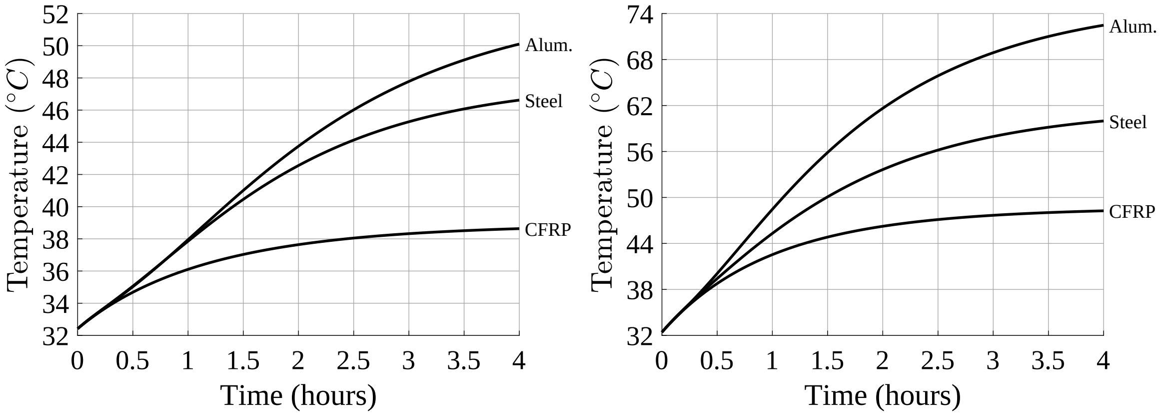

(a) Dual Wheels. (b) Single Wheels.

Figure 6.12: Comparison of Tyre Temperature Responses ($P_b = 2.5\ kW$).

dissipate an average of 374 W (42%) more heat by convection than for the steel or aluminium configurations. Since U_{sa} has not changed, the CFRP wheel brake shoe must reach higher temperatures in order to achieve the necessary thermal gradient.

Table 6.10: Steady State Inter-Component Heat Transfer (CFRP, $P_b = 2.5\ kW$).

Interaction	Symbol	Q_{ss} (W) Dual	Single
Shoe - Beam	Q_{sb}	415.1	411.8
Shoe - Rim	Q_{sr}	821.4	834.8
Rim - Tyre	Q_{rt}	41.74	46.12
Beam - Air	Q_{ba}	434.7	431.3
Shoe - Air	Q_{sa}	1264	1253
Rim - Air	Q_{ra}	779.6	788.7
Tyre - Air	Q_{ta}	738.8	743.2

On average, the CFRP rims transmit 436 W (91%) and 788 W (95%) less heat to the tyres than the steel and aluminium rims respectively. This is a consequence of the low thermal conductivity of CFRP which allows for 95% of the heat which enters the rim to be convected to the air before entering the tyre. Since U_{ta} is independent of rim material, the CFRP wheel tyres will exhibit comparatively small changes in average tyre temperature.

CFRP rims would therefore reduce the likelihood of tyre blowout due to overheating caused by alpine braking, but at the expense of heightening the risk of premature brake fade, accelerated brake wear and bearing fires. The convective performance of the brake must be improved if CFRP rims are to be implemented on heavy vehicles. This can be achieved by using ventilated brake discs in place of drums, which is standard practice on high-performance vehicles where CFRP rims are currently used. Application of CFRP rims to vehicles which implement regenerative braking (in which the dissipative requirements of brake heat are less severe) may be required.

The elevated brake temperatures when using CFRP-rimmed wheels results in higher average rim temperatures. This is problematic for CFRP rims because epoxy resins are limited to operating temperatures below 120 $°C$ [56]. The single, CFRP rim reaches an average temperature of 100 $°C$ for $P_b = 2.5\ kW$ which is a moderate braking power. Furthermore, the rims are mounted to the axle hub which is in direct contact with the brake drum. The maximum temperature experienced by the rim will therefore be close to the brake temperature which is above 120 $°C$. CFRP rims must therefore be designed such that they are insulated against direct exposure to excessive temperature.

7 Conclusions

1. The axle beam, brake shoe, rim and tyre temperatures of four heavy vehicle wheel configurations (dual, steel-rimmed, dual, aluminium-rimmed, single, steel-rimmed and single, aluminium-rimmed) were measured for 1 $kW - 4\ kW$ of continuous braking.

2. Lumped mass models were developed by applying an energy balance to the axle beam, brake shoe, rim and tyre.

   (a) These equations were manipulated into state-space form and can be used to calculate the transient temperature response of the axle beam, brake shoe and drum, rim and tyre to any braking profile.

   (b) A simulated-annealing optimisation routine was used to determine model parameters for the overall heat transfer coefficients of each wheel assembly as well as the magnitudes of auxiliary heat sources (bearing fiction and hysteresis).

   (c) These models were used to calculate the temperature responses of the four wheel configurations to 2.5 kW of continuous braking so that their thermal responses could be directly compared.

3. Conclusions drawn from the temperature responses of the four wheel configurations to the 2.5 kW of continuous or alpine braking above are as follows:
   (a) Steel-rimmed wheels exhibit higher brake temperature increases. This difference is 2.1% or less at steady state and considered small in terms of brake and bearing wear, brake fade and the likelihood of fires.
   (b) The increase in average tyre temperature when using aluminium rims is, on average, 30% higher than when using steel rims.
   (c) The above increased tyre temperature is attributed to the higher thermal conductivity and cross-sectional areas of aluminium rims which enhance conduction through the rim and allows more heat to enter the tyre rather than being convected to the air.
   (d) The increase in average tyre temperature when using single wheels is, on average, 82% higher than when using dual wheels.
   (e) The above increased tyre temperature is attributed to the lower surface area of single wheel tyres which inhibits convection of heat from the tyre to the ambient air.
   (f) For $P_b = 4\ kW$ and an initial temperature of 32 $°C$, the maximum tyre temperature of the single aluminium wheel will reach approximately 133 $°C$ (tyre degredation begins at 90 $°C$ − 120 $°C$) in contrast to 79.6 $°C$ for the dual, steel wheel.
   (g) Wheel configuration has the greatest impact on tyre temperature. The increase in tyre temperature when using single versus dual wheels is further amplified when using aluminium versus steel rims. The increase in average temperature of the single, aluminium wheel tyre is therefore 135% higher than the dual, steel wheel tyre.
   (h) Under alpine braking conditions, because the tyres fitted to single wheel assemblies run hotter than the tyres fitted to dual wheel assemblies, single wheels are at a greater risk of tyre blowout. Similarly, under alpine braking conditions, because the tyres fitted to aluminium rims run hotter than the tyres fitted to steel rims, aluminium-rimmed wheels are at a greater risk of tyre blowout.
4. The lumped mass models for the single and dual wheel assemblies were adapted to investigate the temperature responses of conceptual CFRP rims to 2.5 kW of continuous braking. Conclusions drawn from these results are as follows:

(a) The brakes fitted to CFRP rims run at high temperatures; $67.7\ °C - 70.1\ °C$ hotter than when using steel or aluminium rims.

(b) The brakes fitted to CFRP rims run hotter because of the relatively low thermal conductivity of the CFRP which insulates the brakes and thus causes an average of 42% more heat to be convected directly from the brake to the air.

(c) It is more likely that brake overheating will occur when using CFRP rims; leading to premature brake fade, accelerated wear or bearing fires.

(d) The CFRP will likely be exposed to temperatures above the allowable limits of the epoxy matrix, thereby causing degradation of the rim.

(e) CFRP rims inhibit conduction of heat into the tyres, leading to average tyre temperatures up to $24\ °C$ (60%) or 69% ($14.6\ °C$) lower for alpine braking conditions.

(f) CFRP rims are not feasible for heavy vehicle applications unless measures are taken to improve brake cooling and insulate the rims from exposure to excessive temperatures. Further research is needed to determine for which wheel assemblies and braking mechanisms CFRP rims are suitable.

References

[1] M. J. Sprung, L. X. Nguyen, M. Chambers, J. Goworowska, C. Rick, J. Sedor, J. Berg, C. Ford, M. Liu, A. Mallik, D. Menegus, B. Pandey, D. Smallen, W. H. Moore, and A. Wingfield, "Freight Facts and Figures," Bureau of Transportation Statistics, United States Department of Transportation, Washington, Tech. Rep., 2017. [Online]. Available: https://www.bts.gov/sites/bts.dot.gov/files/docs/FFF_2017.pdf

[2] Statistics South Africa, "Statistical Release P7162 Land Transport Survey (Preliminary)," Pretoria, Tech. Rep. April, 2018. [Online]. Available: http://www.statssa.gov.za/publications/P7162/P7162March2017.pdf

[3] N. Viljoen, U. Joubert, J. Havenga, Z. Simpson, D. Kumar, I. Hans, S. Gertenbach, C. Rossouw, W. Steyn, P. Nordengen, R. Luke, and G. Heyns, "10th Annual State of Logistics Survey for South Africa," Council for Scientific and Industrial Research (CSIR), Pretoria, Tech. Rep., 2013. [Online]. Available: https://www.csir.co.za/sites/default/files/Documents/10th_SoL_Bold_Steps_Forward_web.pdf

[4] Road Traffic Management Corporation, "RTMC commends Mpumalanga for impounding un-roadworthy trucks," Pretoria, pp. 1–3, 2016.

[5] ——, "Truck accidents claim 24 lives and 69 injuries in 24-hour period The," Pretoria, pp. 1–2, 2017.

[6] P. M. Hart, "A review of truck fire causation," in *12th International Symposium on Heavy Vehicle Transportation Technology*, Stockholm, 2012.

[7] R. Benoit, L. Lafrance, D. Malo, and J. Baron, "Heavy vehicles tire blowout and explosion," ASTE and IRST, Montréal, Tech. Rep. March, 2009.

[8] L. Henderson and D. Cebon, "Full-scale testing of a novel slip control braking system for heavy vehicles," *Proceedings of the Institution of Mechanical Engineers, Part D: Journal of Automobile Engineering*, vol. 230, no. 9, pp. 1221–1238, 2016.

[9] Y. Malzahn and F. Kienhöfer, "The effect of wheel configuration on vehicle component temperatures," in *13th International Symposium on Heavy Vehicle Transport Technology*, San Luis, 2014.

[10] Y. Zhao, L. quan Ren, X. Tong, H. Zhou, and L. Chen, "Frictional wear and thermal fatigue behaviours of biomimetic coupling materials for brake drums," *Journal of Bionic Engineering*, vol. 5, no. SUPPL., pp. 20–27, 2008.

[11] S. L. Sokolov, "Analysis of the heat state of pneumatic tires by the finite element method," *Journal of Machinery Manufacture and Reliability*, vol. 38, no. 3, pp. 310–314, 2009.

[12] R. K. Luo, W. J. Mortel, and X. P. Wu, "Investigation on rubber failure due to heat generation under dynamic loading," *Proceedings of the Institution of Mechanical Engineers, Part L: Journal of Materials: Design and Applications*, vol. 229, no. 1, pp. 77–87, 2015.

[13] J. R. Welty, G. L. Rorrer, and D. G. Foster, *Fundamentals of Momentum, Heat and Mass Transfer*, 6th ed. Singapore: John Wiley & Sons, 2015.

[14] J. R. Cho, H. W. Lee, W. B. Jeong, K. M. Jeong, and K. W. Kim, "Numerical estimation of rolling resistance and temperature distribution of 3-D periodic patterned tire," *International Journal of Solids and Structures*, vol. 50, no. 1, pp. 86–96, 2013.

[15] J. Subel and F. Kienhöfer, "On tyre blowouts and overheating brakes towards safer trucks," in *1st SAIMechE PG Student Conference*, Johannesburg, 2017.

[16] A. Day, *Braking of Road Vehicles*. Oxford: Elsevier, 2014.

[17] R. Limpert, *Brake Design and Safety*, 3rd ed. Warrendale: SAE International, 2011.

[18] A. A. Yevtushenko, A. Adamowicz, and P. Grzes, "Three-dimensional FE model for the calculation of temperature of a disc brake at temperature-dependent coefficients of friction," *International Communications in Heat and Mass Transfer*, vol. 42, pp. 18–24, 2013.

[19] A. Belhocine and M. Bouchetara, "Thermal analysis of a solid brake disc," *Applied Thermal Engineering*, vol. 32, no. 1, pp. 59–67, 2012.

[20] A. A. Alnaqi, D. C. Barton, and P. C. Brooks, "Reduced scale thermal characterization of automotive disc brake," *Applied Thermal Engineering*, vol. 75, pp. 658–668, 2015.

[21] P. Grześ, "Numerical analysis of temperature field in a disc brake at different cover angle of the pad," *Acta Mechanica et Automatica*, vol. 8, no. 4, pp. 185–188, 2014.

[22] A. A. Yevtushenko and P. Grzes, "Mutual influence of the sliding velocity and temperature in frictional heating of the thermally nonlinear disc brake," *International Journal of Thermal Sciences*, vol. 102, pp. 254–262, 2016.

[23] A. Yevtushenko and P. Grzes, "Maximum temperature in a three-disc thermally nonlinear braking system," *International Communications in Heat and Mass Transfer*, vol. 68, pp. 291–298, 2015.

[24] A. Adamowicz and P. Grzes, "Influence of convective cooling on a disc brake temperature distribution during repetitive braking," *Applied Thermal Engineering*, vol. 31, no. 14-15, pp. 2177–2185, 2011.

[25] A. Yevtushenko and P. Grzes, "Effect of dimensions of pad and disk on the temperature and duration of braking," *Journal of Friction and Wear*, vol. 36, no. 4, pp. 280–285, 2015.

[26] P. Grzes, "Determination of the maximum temperature at single braking from the FE solution of heat dynamics of friction and wear system of equations," *Numerical Heat Transfer, Part A: Applications*, vol. 71, no. 7, pp. 737–753, 2017.

[27] A. Adamowicz and P. Grześ, "Convective cooling of a disc brake during single braking," *Acta Mechanica et Automatica*, vol. 6, no. 2, pp. 5–10, 2012.

[28] A. A. Yevtushenko and P. Grzes, "Axisymmetric FEA of temperature in a pad/disc brake system at temperature-dependent coefficients of friction and wear," *International Communications in Heat and Mass Transfer*, vol. 39, no. 8, pp. 1045–1053, 2012.

[29] A. Adamowicz and P. Grzes, "Analysis of disc brake temperature distribution during single braking under non-axisymmetric load," *Applied Thermal Engineering*, vol. 31, no. 6-7, pp. 1003–1012, 2011.

[30] M. R. Kim, B. J. Ahn, J. M. Lee, and Y. K. Jung, "Numerical investigation of thermal behavior in brake assembly during the ALPINE braking mode," *SAE Technical Paper Series*, vol. 2007, no. 724, 2007.

[31] Y. J. Lin and S. J. Hwang, "Temperature prediction of rolling tires by computer simulation," *Mathematics and Computers in Simulation*, vol. 67, no. 3, pp. 235–249, 2004.

[32] H. Golbakhshi and M. Namjoo, "Investigating temperature effects on mechanical behavior of rubber compounds embedded in composite structure of pneumatic tires," *International Journal of Advanced Design and Manufacturing Technology*, vol. 7, no. 4, 2014.

[33] W. Z. W. Zepeng, "Finite element analysis of mechanical and temperature field for a rolling tire," in *International Conference on Measuring Technology and Mechatronics Automation*, Changsha, 2010, pp. 278–283.

[34] Y. Li, W. Y. Liu, and S. Frimpong, "Effect of ambient temperature on stress, deformation and temperature of dump truck tire," *Engineering Failure Analysis*, vol. 23, pp. 55–62, 2012.

[35] F. Farroni, A. Sakhnevych, and F. Timpone, "An Evolved Version of Thermo Racing Tyre for Real Time Applications," in *World Congress on Engineering*, vol. II, London, 2015.

[36] R. C. Fisher, "Transient thermal response of single and dual wheel drum brakes," University of the Witwatersrand, Johannesburg, Tech. Rep., 2014.

[37] F. Meng, J. McKechnie, and S. J. Pickering, "An assessment of financial viability of recycled carbon fibre in automotive applications," *Composites Part A: Applied Science and Manufacturing*, vol. 109, no. November 2017, pp. 207–220, 2018.

[38] R. Stewart, "Rebounding automotive industry welcome news for FRP," *Reinforced Plastics*, vol. 55, no. 1, pp. 38–44, 2011.

[39] "Carbon composites and cars technology watch 2012," *Reinforced Plastics*, vol. 57, no. 1, pp. 39–42, 2013.

[40] A. Jacob, "Carbon fibre and cars 2013 in review," *Reinforced Plastics*, vol. 58, no. 1, pp. 18–19, 2014.

[41] M. Giger and P. Ermanni, "Development of CFRP racing motorcycle rims using a heuristic evolutionary algorithm approach," *Structural and Multidisciplinary Optimization*, vol. 30, no. 1, pp. 54–65, 2005.

[42] L. Nickels, "Composites driving the auto industry," *Reinforced Plastics*, vol. 62, no. 1, pp. 38–39, 2017.

[43] J. J. Gou, Y. J. Dai, S. Li, and W. Q. Tao, "Numerical study of effective thermal conductivities of plain woven composites by unit cells of different sizes," *International Journal of Heat and Mass Transfer*, vol. 91, pp. 829–840, 2015.

[44] K. Dong, K. Liu, Q. Zhang, B. Gu, and B. Sun, "Experimental and numerical analyses on the thermal conductive behaviors of carbon fiber/epoxy plain woven composites," *International Journal of Heat and Mass Transfer*, vol. 102, pp. 501–517, 2016.

[45] R. S. Burns, "8 - State-space methods for control system design," in *Advanced Control Engineering*, R. S. Burns and R. S. Burns, Eds. Oxford: Butterworth-Heinemann, 2001, pp. 232–271.

[46] Speedline Truck, "Sl 830 - Sl 905 - Dual wheel Al," Bolzano.

[47] ——, "SL 1463 - Single wheel Al," Bolzano.

[48] Festo, "Search LFR-1/4-D-MINI-A, VPPM-6L-L-1-G18-0L6H-V1P-C1," 2016. [Online]. Available: https://www.festo.com/net/en-za_za/SupportPortal/InternetSearch.aspx

[49] Y. Malzahn, "The effect of wheel configuration on truck brake temperatures," University of the Witwatersrand, Johannesburg, Tech. Rep., 2013.

[50] P. Veerasamy, "Vibrational response analysis of single and dual truck tires," University of the Witwatersrand, Johannesburg, Tech. Rep., 2014.

[51] ——, "Vibrational Input Features to a Rolling Road Rig," University of the Witwatersrand, Johannesburg, Tech. Rep., 2014.

[52] Siemens, "Search S7-1200 CPU 1212C AC/DC/RLY, CSM 1277, SM 1232, WP231," 2016. [Online]. Available: https://www.automation.siemens.com/bilddb/search.aspx

[53] D. S. Johnson, C. R. Aragon, L. A. McGeoch, and C. Schevon, "Optimization by simulated annealing : An experimental evaluation ; Part I , graph partitioning," *Operations Research*, vol. 37, no. 6, pp. 865–892, 1989.

[54] Bergische Achsen Kommanditgesellsch (BPW), "Commercial Vehicle Catalogue," 2009. [Online]. Available: http://www.bpw.co.za/downloads/prospectus/BPW-NFZ-1168901.pdf

[55] T. Tang, D. Johnson, R. E. Smith, and S. D. Felicelli, "Numerical evaluation of the temperature field of steady-state rolling tires," *Applied Mathematical Modelling*, vol. 38, no. 5-6, pp. 1622–1637, 2014.

[56] D. Gay, *Composite Materials Design and Applications*, 3rd ed. Boca Raton: CRC Press, 2014.

A Individual Modelling Plots and Evaluation

The temperature response of the four wheel configurations for $P_b \approx 1\ kW - 4\ kW$ were calculated and plotted with experimental data in Figure A.1 to Figure A.16.

The percentage $RMSE$s and absolute maximum percentage errors for each curve were determined and listed in Table A.1 to Table A.8. The modelled temperatures for the axle beam, rims and tyres agree closely with experimental measurements across different braking powers. The $RMSE$s for the individual tests are higher than for the power-averaged results as averaging mitigates the impact of experimental error.

The model under-predicts brake shoe temperature for lower braking powers and over-predicts brake shoe temperature for higher braking powers. This is a consequence of radiative cooling which is non-linear but was modelled to be linear. The model will tend to prematurely indicate that the brakes have reached unsafe temperatures, and will therefore give a conservative indication of safe operating conditions.

Table A.1: Model Percentage $RMSE$ (Dual, Steel).

P_b	$RMSE$ (%)				
(kW)	Axle Beam	Brake Shoe	Rim	Tyre	Maximum
1	0.51	6.3	10	13	13
2	0.94	6.0	6.0	6.1	6.1
3	1.1	7.3	4.3	3.4	7.3
4	1.8	9.2	8.0	9.6	9.6
Maximum	1.8	9.2	10	13	13

Table A.2: Model Maximum Percentage Error (Dual, Steel).

P_b	Maximum Error (%)				
(kW)	Axle Beam	Brake Shoe	Rim	Tyre	Maximum
1	0.99	15	17	17	17
2	1.6	22	14	9.9	22
3	1.7	32	12	7.8	32
4	3.0	34	13	15	34
Maximum	3.0	34	17	17	34

Table A.3: Model Percentage $RMSE$ (Dual, Aluminium).

P_b	$RMSE$ (%)				
(kW)	Axle Beam	Brake Shoe	Rim	Tyre	Maximum
1	2.2	12	2.4	2.6	12
2	1.0	7.1	3.0	4.5	7.1
3	1.4	7.3	2.4	3.4	7.3
4	4.0	11	5.0	2.2	11
Maximum	4.0	12	5.0	4.5	12

Table A.4: Model Maximum Percentage Error (Dual, Aluminium).

P_b	Maximum Error (%)				
(kW)	Axle Beam	Brake Shoe	Rim	Tyre	Maximum
1	2.9	14	5.6	4.2	14
2	1.9	16	6.0	6.7	16
3	2.3	27	4.8	7.4	27
4	8.4	34	8.6	4.5	34
Maximum	8.4	34	8.6	7.4	34

Table A.5: Model Percentage $RMSE$ (Single, Steel).

P_b	$RMSE$ (%)				
(kW)	Axle Beam	Brake Shoe	Rim	Tyre	Maximum
1	1.8	13	5.3	8.3	13
2	2.3	9.7	4.3	3.0	9.7
3	1.5	7.2	6.7	2.2	7.2
4	2.7	12	6.2	3.9	12
Maximum	2.7	13	6.7	8.3	13

Table A.6: Model Maximum Percentage Error (Single, Steel).

P_b	Maximum Error (%)				
(kW)	Axle Beam	Brake Shoe	Rim	Tyre	Maximum
1	2.3	15	9.4	12	15
2	3.1	18	8.7	6.1	18
3	3.2	32	18	5.6	32
4	5.9	41	16	8.7	41
Maximum	5.9	41	18	12	41

Table A.7: Model Percentage $RMSE$ (Single, Aluminium).

P_b	$RMSE$ (%)				
(kW)	Axle Beam	Brake Shoe	Rim	Tyre	Maximum
1	0.50	0.73	1.3	2.4	2.4
2	9.3	7.9	6.8	10	10
3	2.7	2.5	2.1	3.0	3.0
4	1.1	3.4	6.1	6.9	6.9
Maximum	9.3	7.9	6.8	10	10

Table A.8: Model Maximum Percentage Error (Single, Aluminium).

P_b	Maximum Error (%)				
(kW)	Axle Beam	Brake Shoe	Rim	Tyre	Maximum
1	0.87	11	6.3	3.3	11
2	1.3	18	5.3	7.0	18
3	2.9	28	4.5	12	28
4	5.5	40	7.9	12	40
Maximum	5.5	40	7.9	12	40

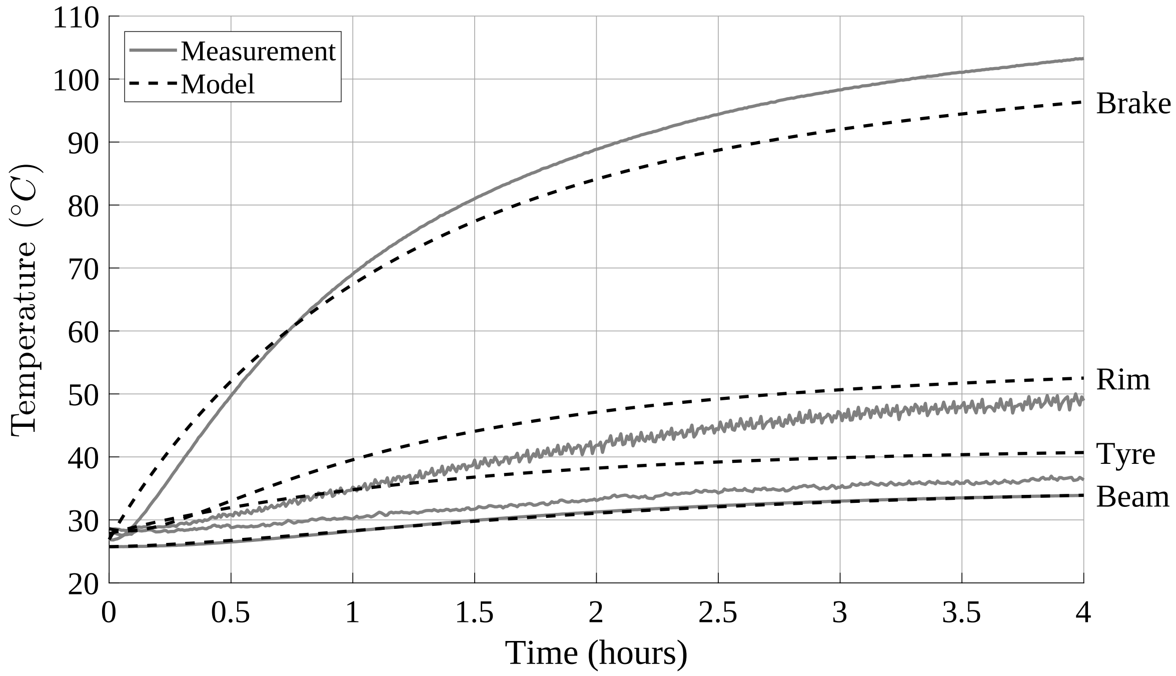

(a) Temperature Response.

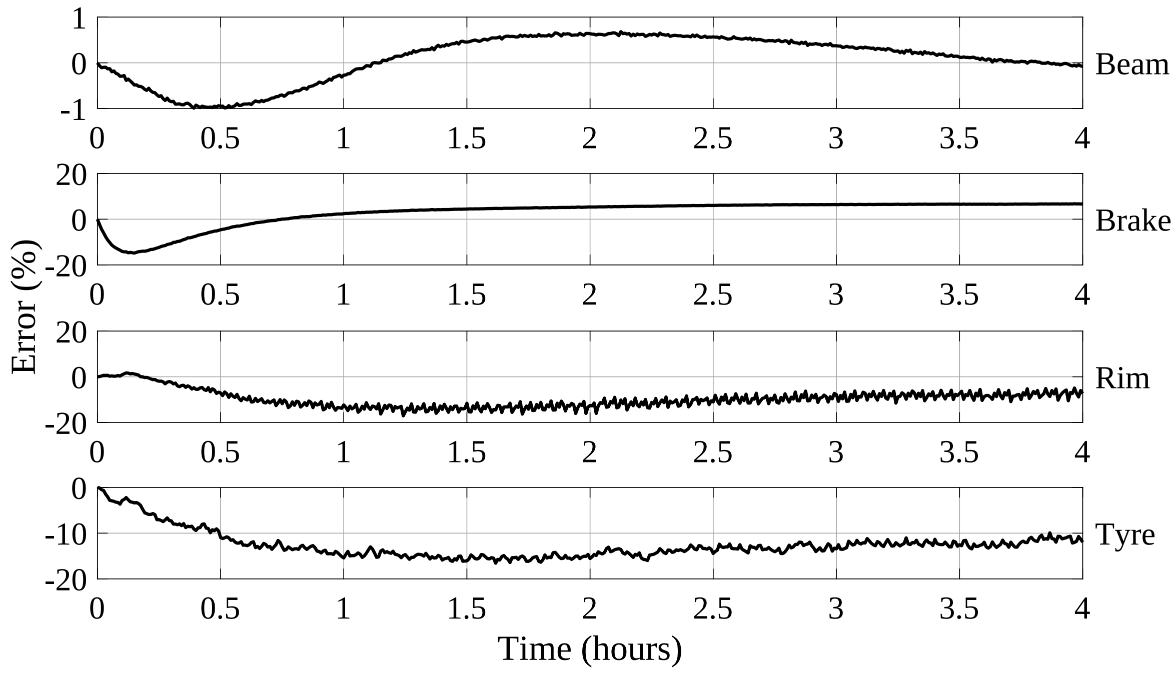

(b) Model Errors.

Figure A.1: Modelling Results (Dual, Steel, $P_b \approx 1\ kW$).

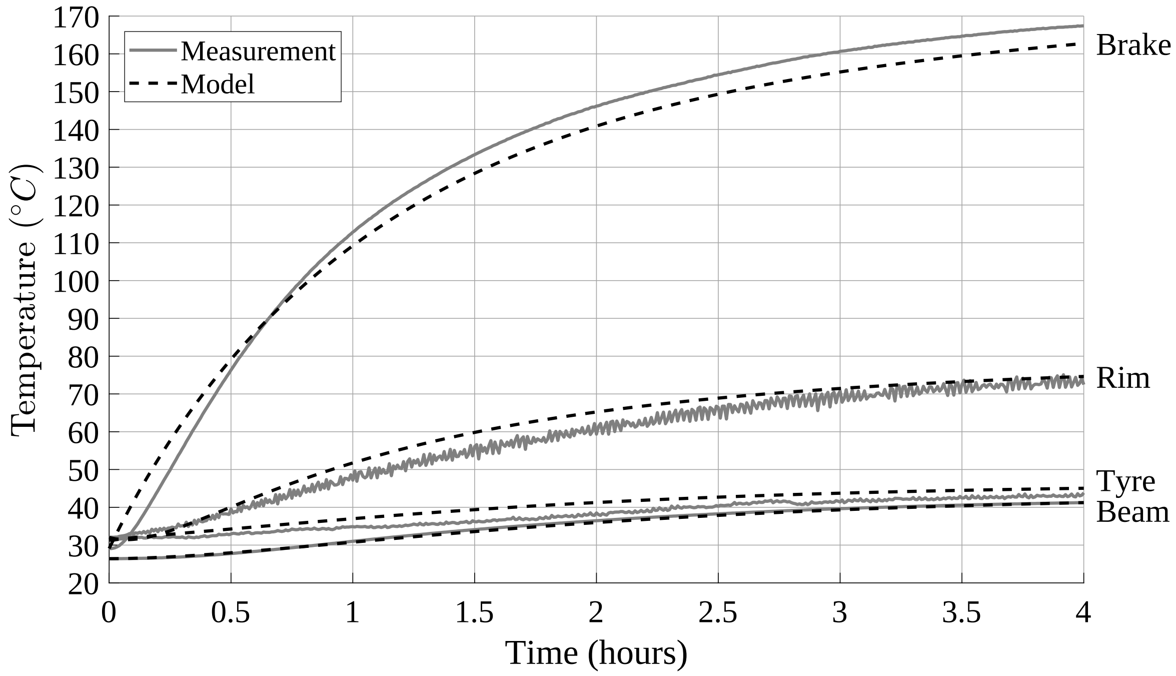

(a) Temperature Response.

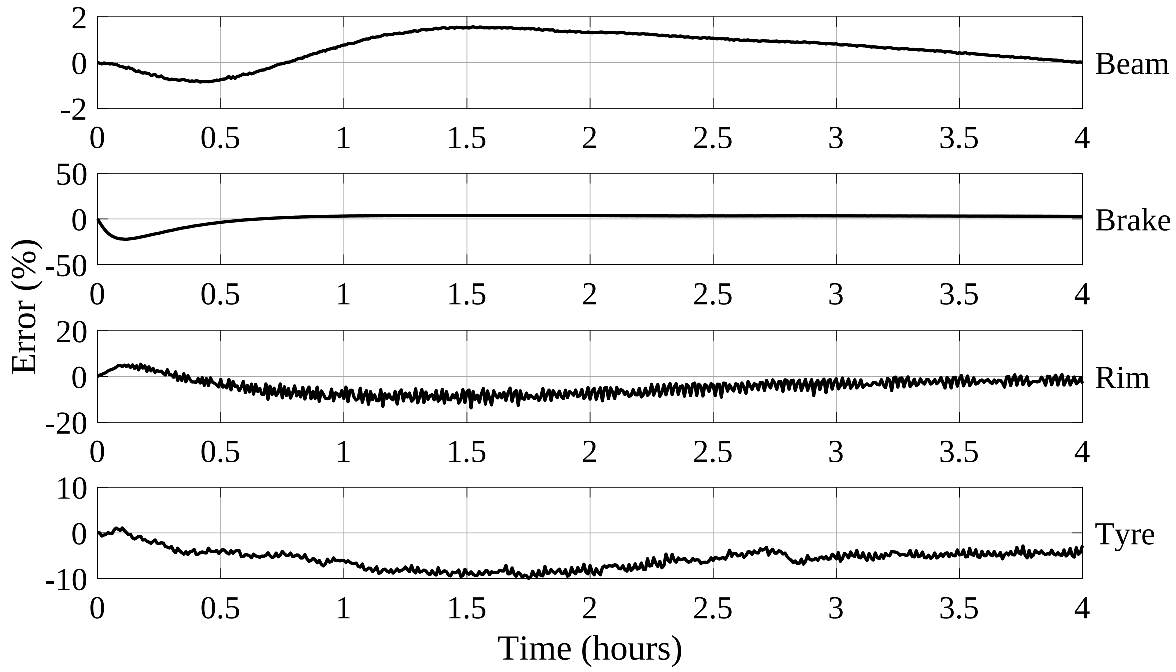

(b) Model Errors.

Figure A.2: Modelling Results (Dual, Steel, $P_b \approx 2\ kW$).

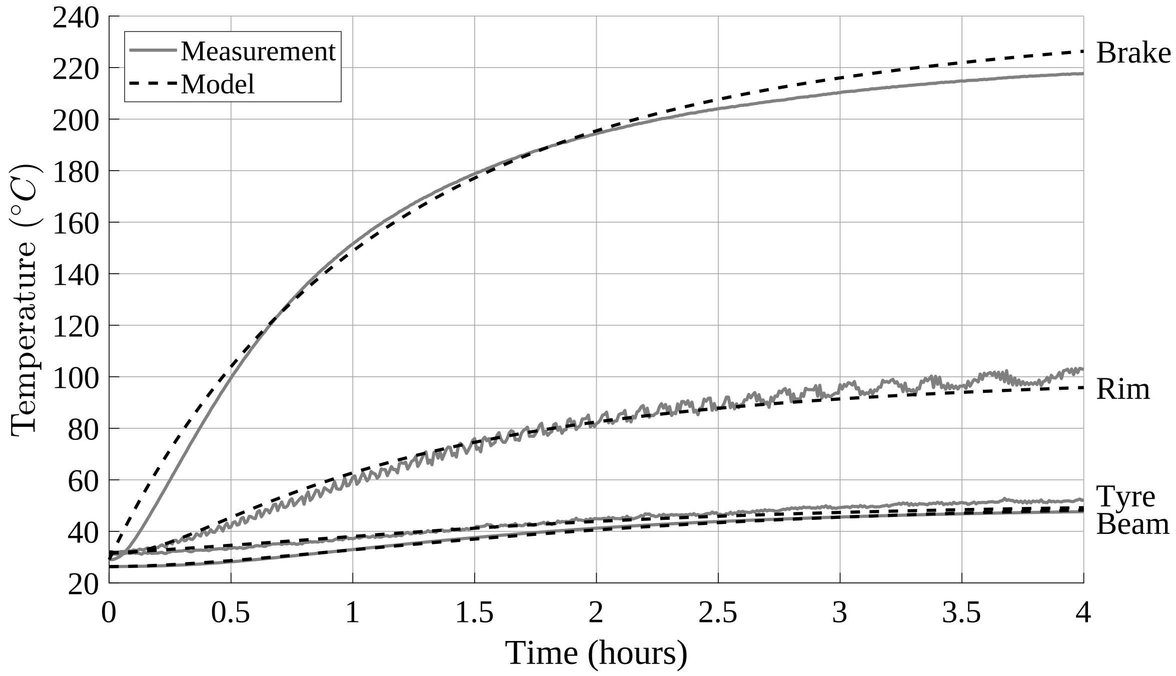

(a) Temperature Response.

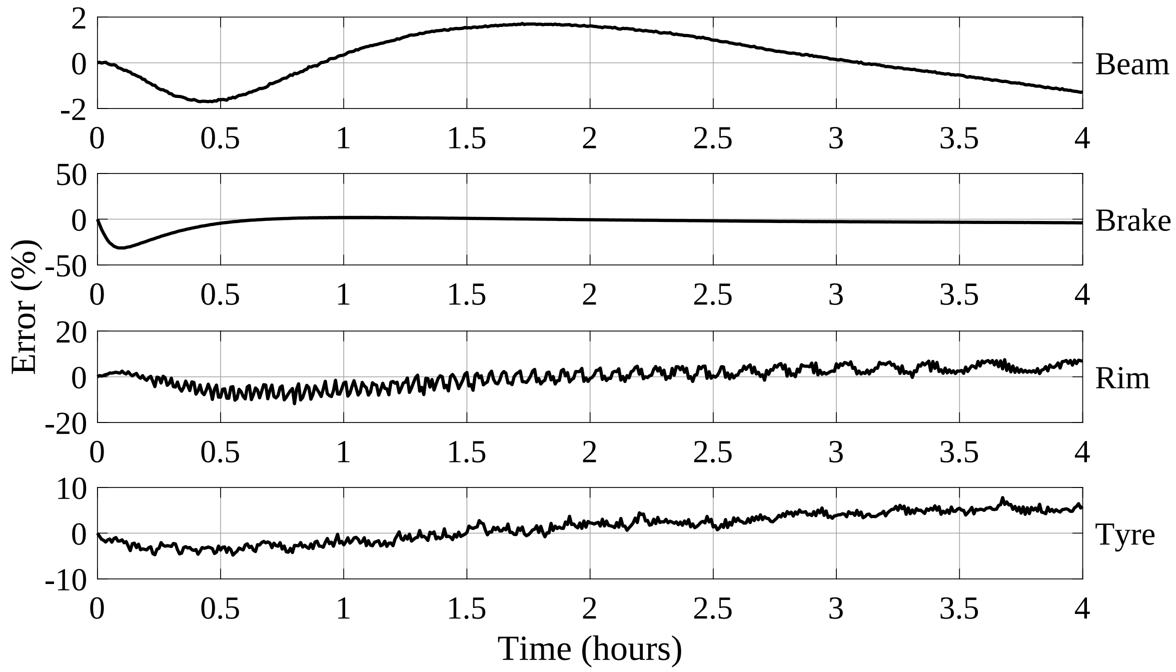

(b) Model Errors.

Figure A.3: Modelling Results (Dual, Steel, $P_b \approx 3\ kW$).

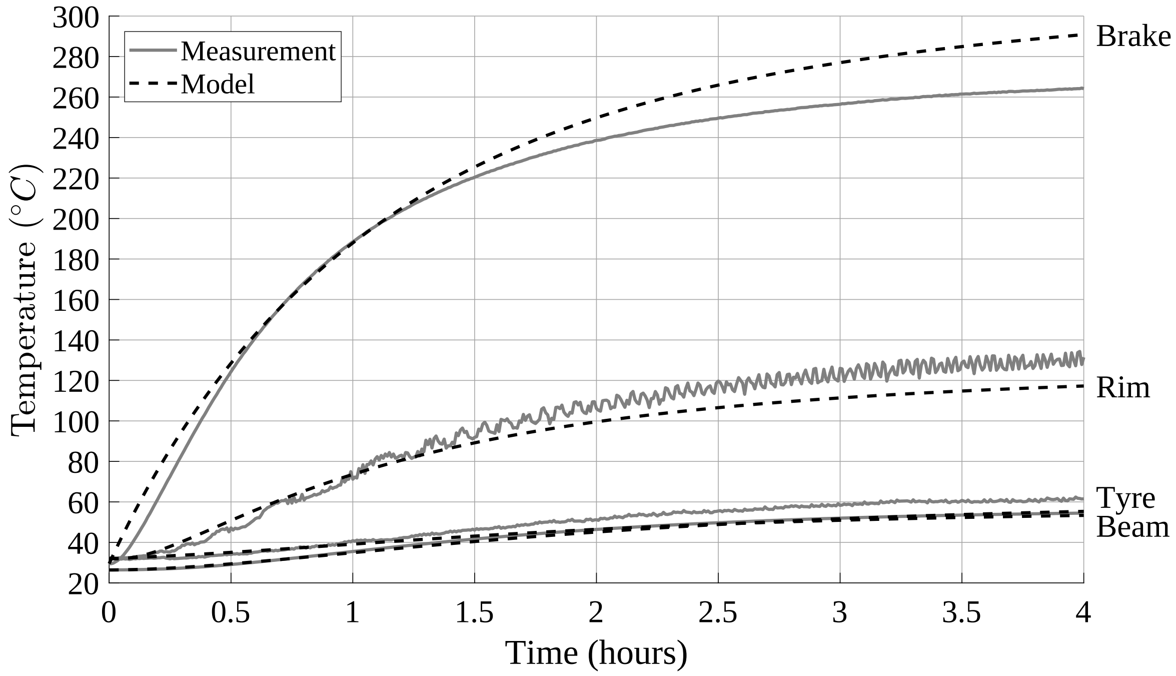

(a) Temperature Response.

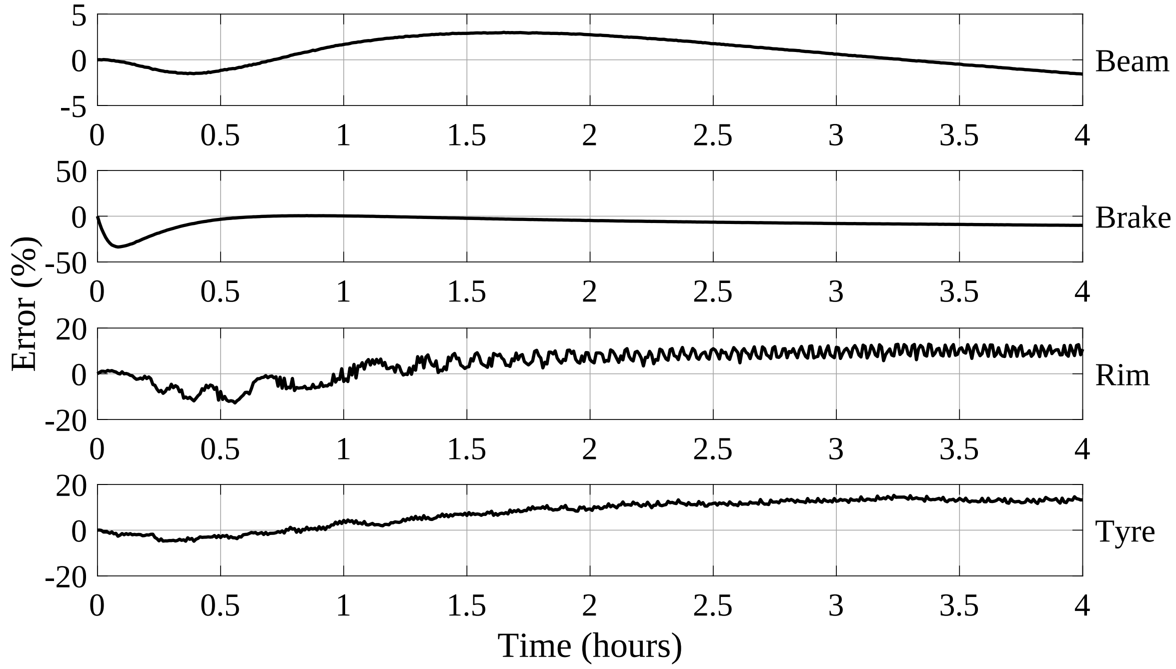

(b) Model Errors.

Figure A.4: Modelling Results (Dual, Steel, $P_b \approx 4\ kW$).

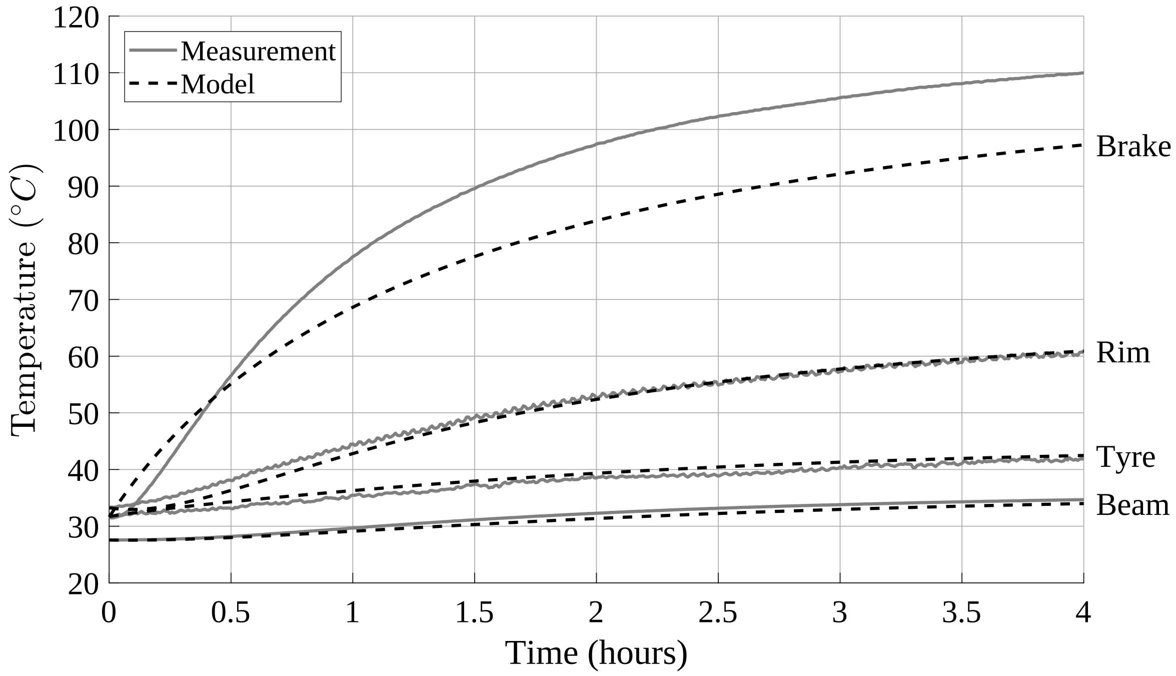

(a) Temperature Response.

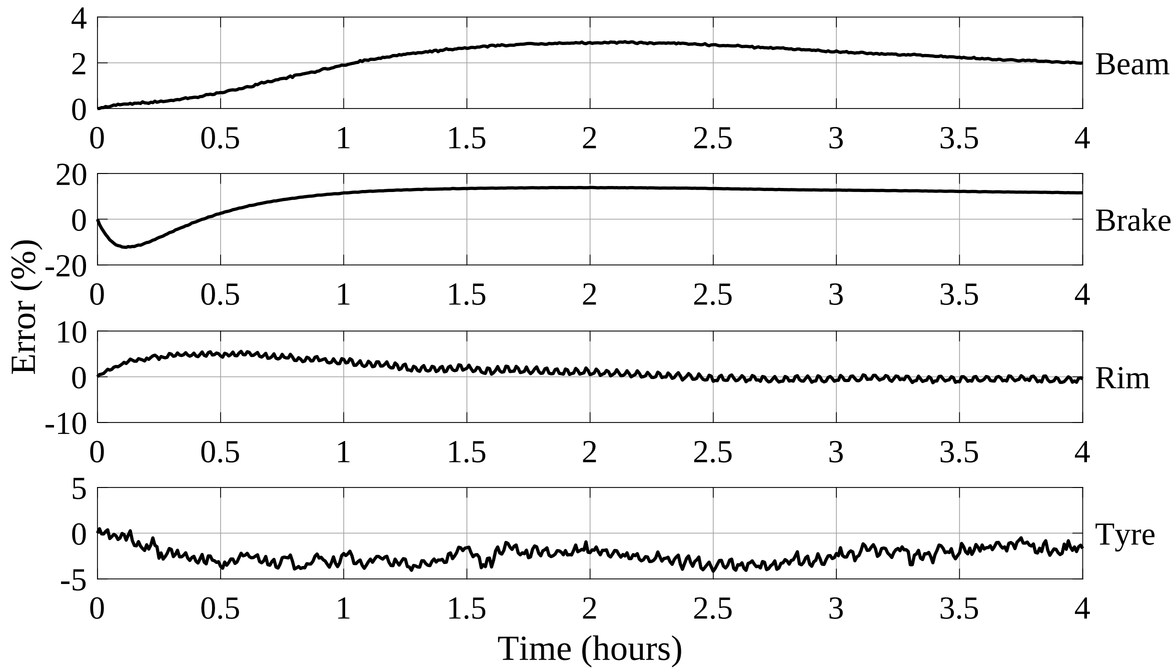

(b) Model Errors.

Figure A.5: Modelling Results (Dual, Aluminium, $P_b \approx 1\ kW$).

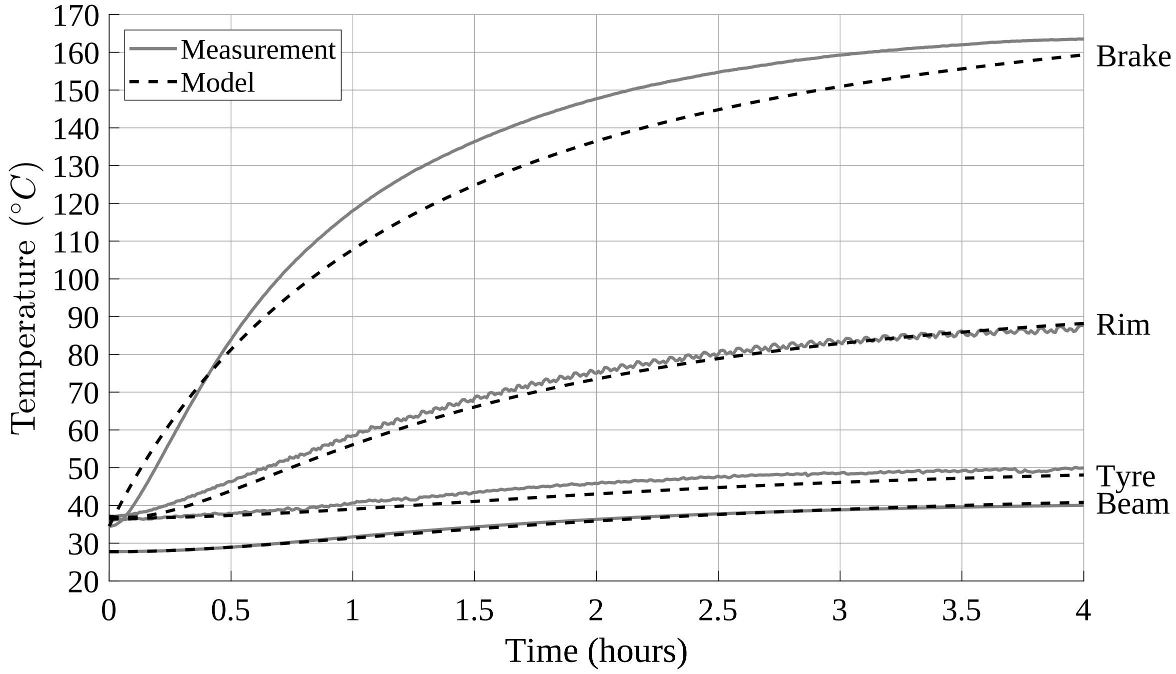

(a) Temperature Response.

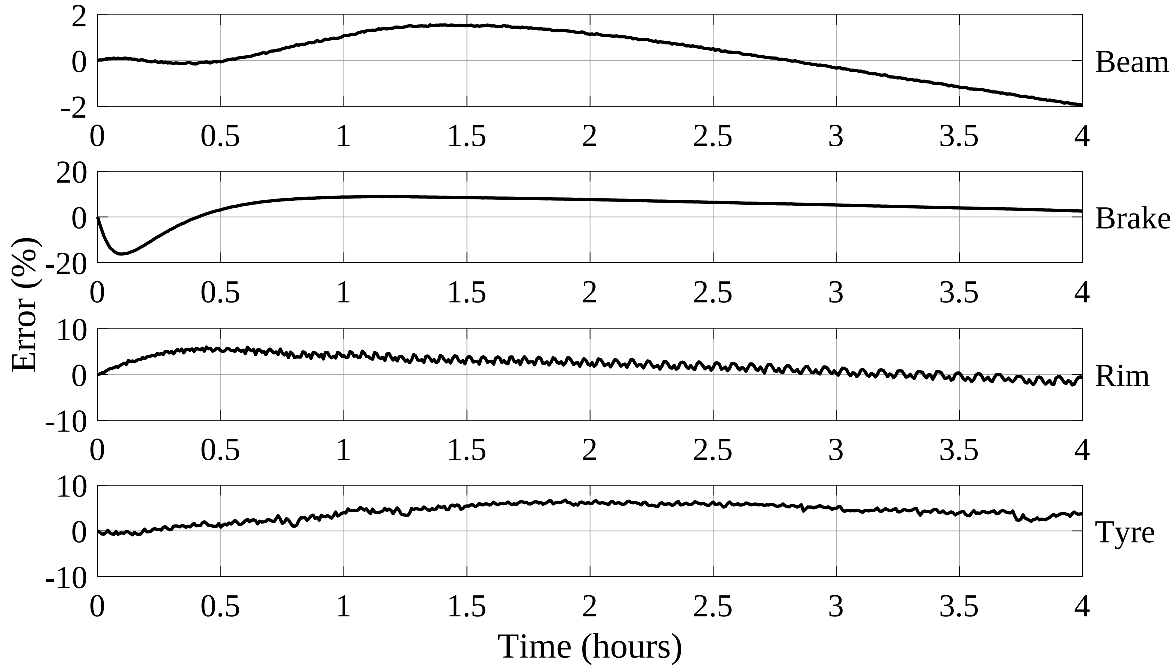

(b) Model Errors.

Figure A.6: Modelling Results (Dual, Aluminium, $P_b \approx 2\ kW$).

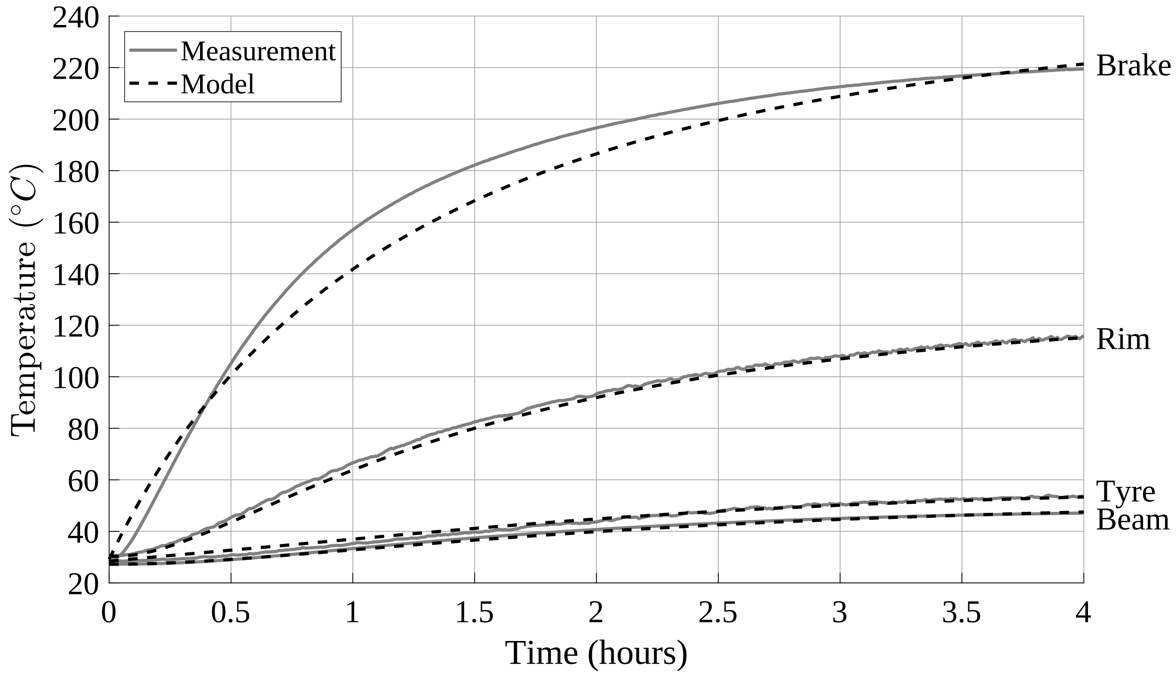

(a) Temperature Response.

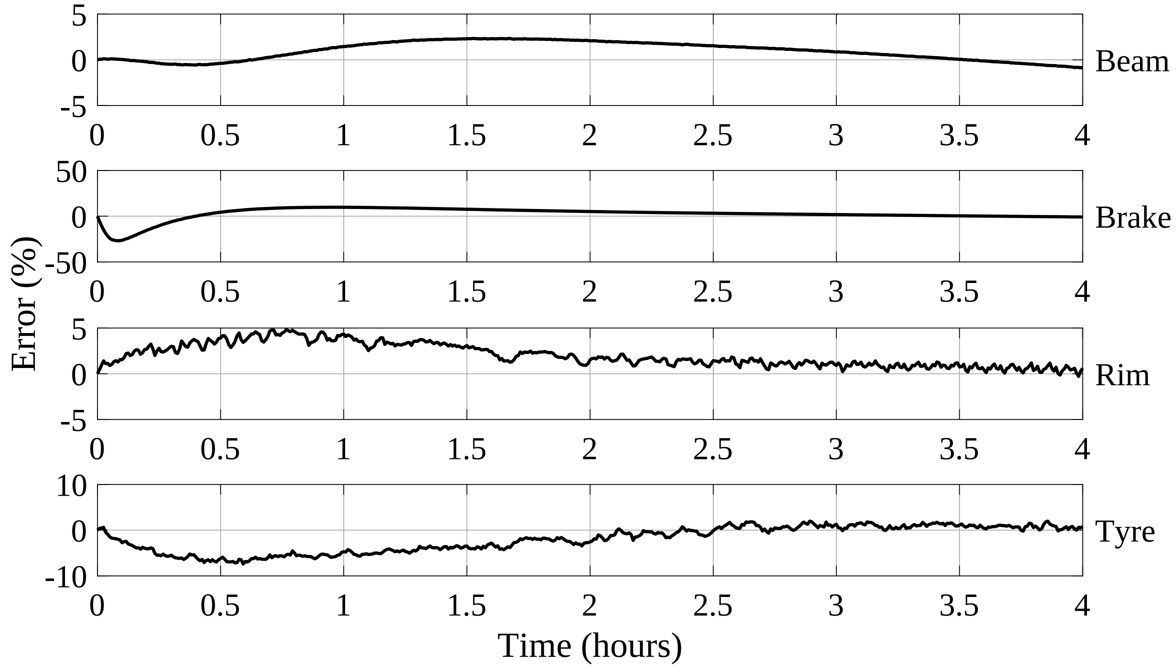

(b) Model Errors.

Figure A.7: Modelling Results (Dual, Aluminium, $P_b \approx 3\ kW$).

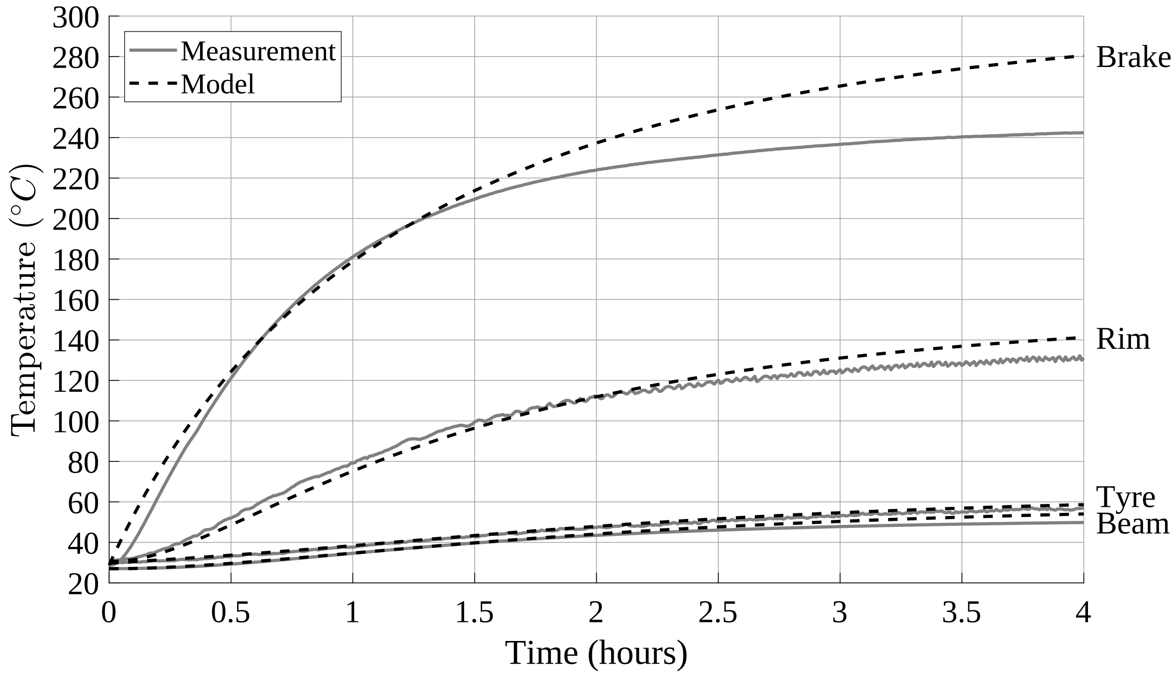

(a) Temperature Response.

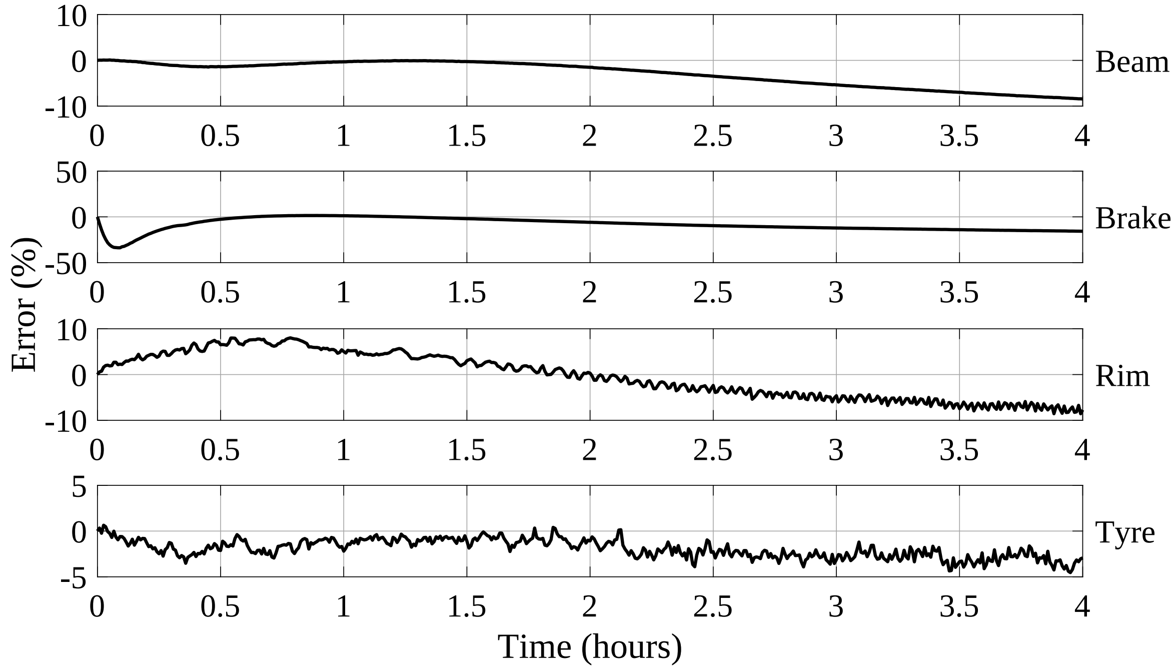

(b) Model Errors.

Figure A.8: Modelling Results (Dual, Aluminium, $P_b \approx 4\ kW$).

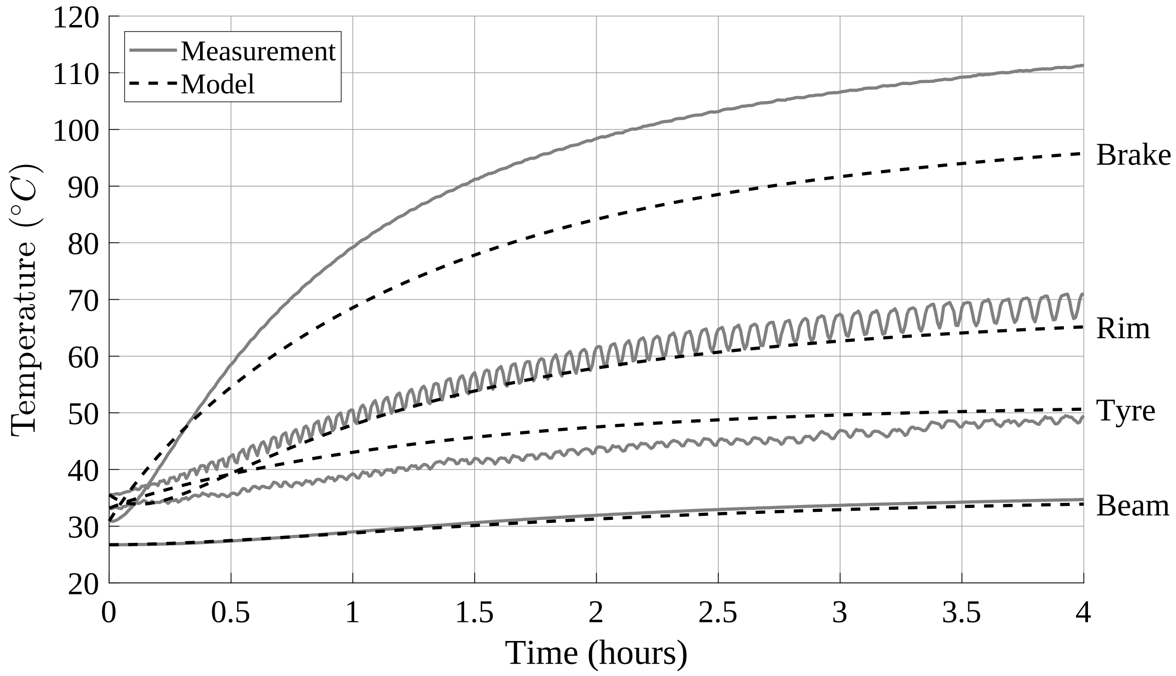

(a) Temperature Response.

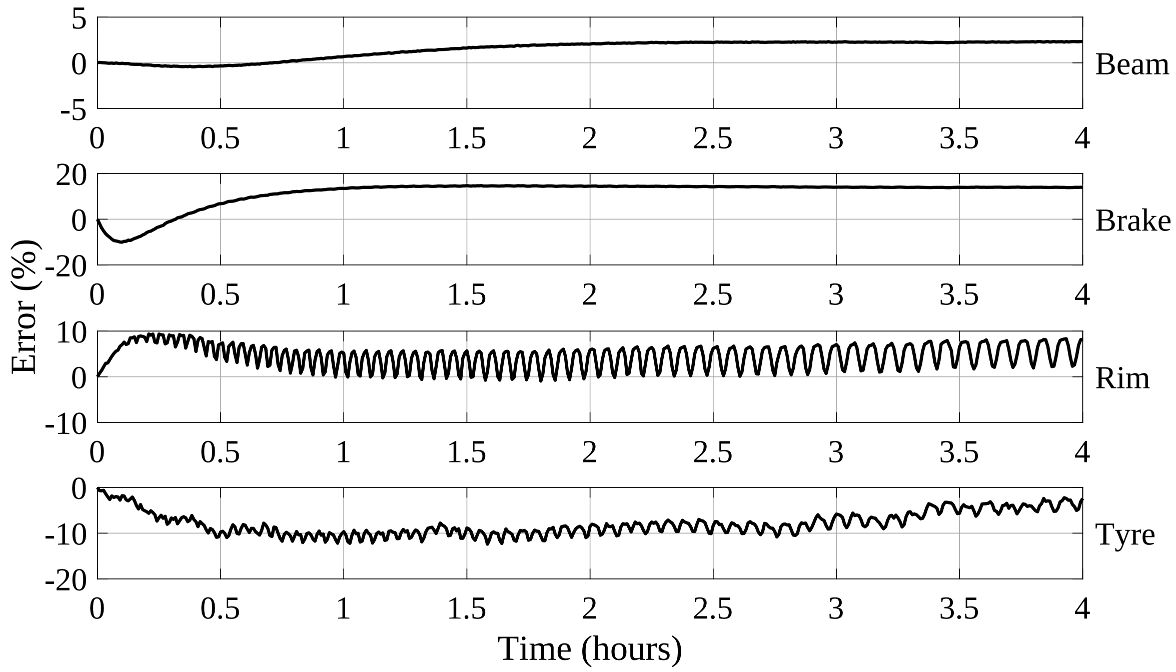

(b) Model Errors.

Figure A.9: Modelling Results (Single, Steel, $P_b \approx 1\ kW$).

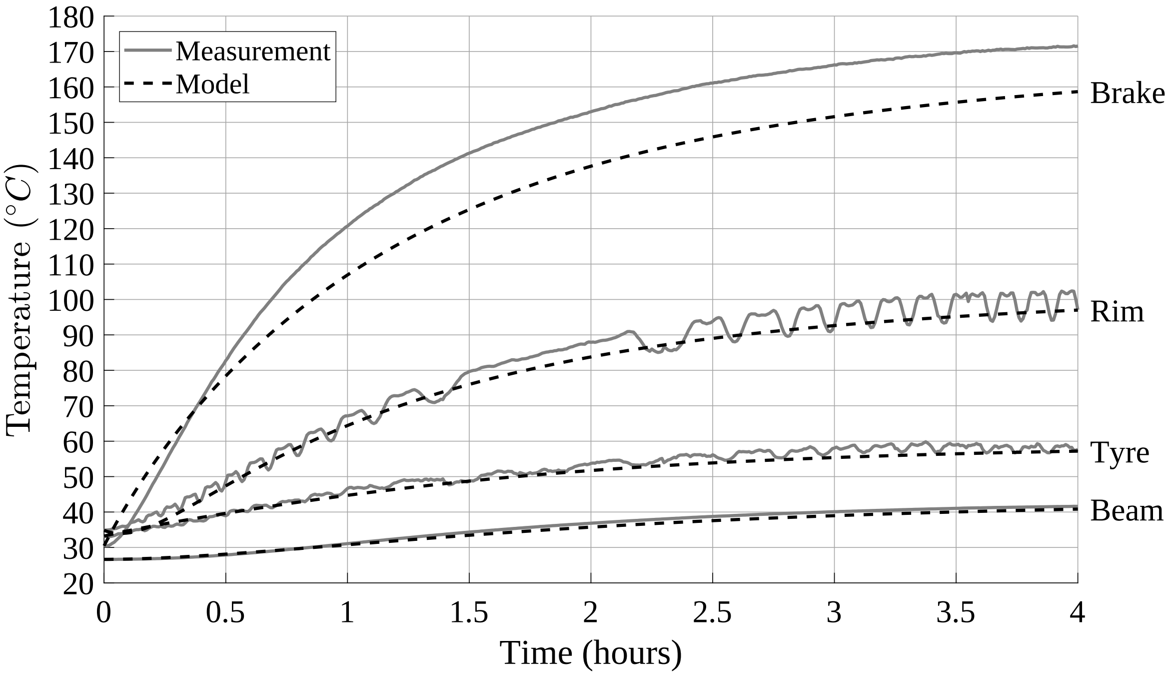

(a) Temperature Response.

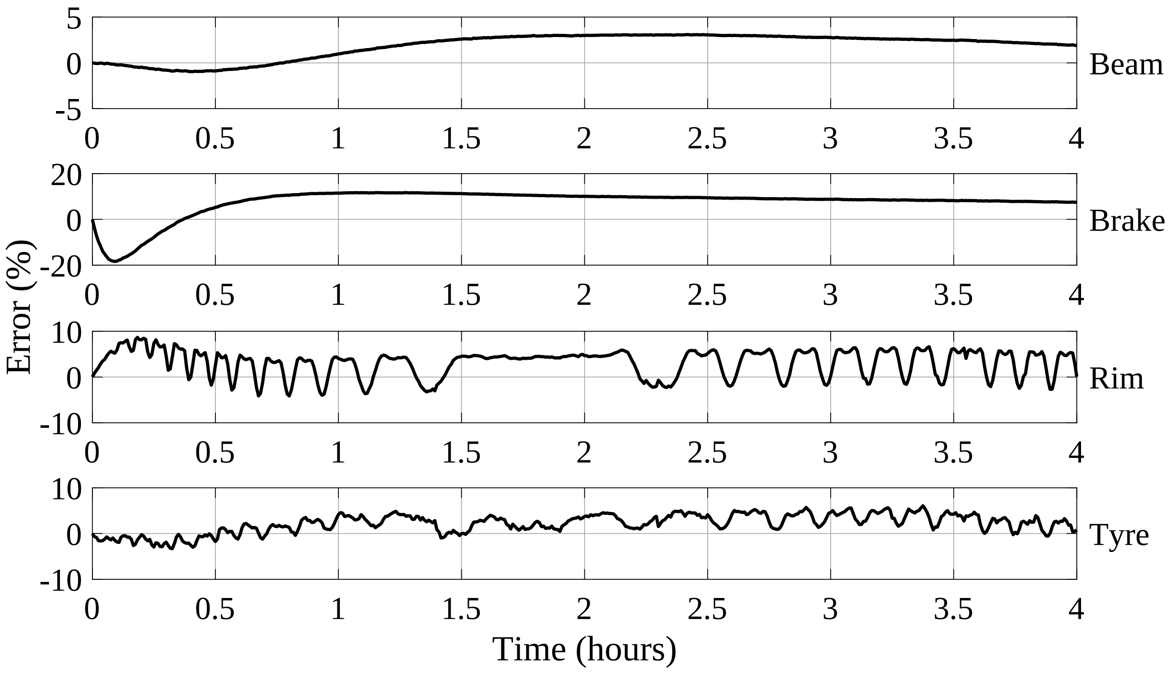

(b) Model Errors.

Figure A.10: Modelling Results (Single, Steel, $P_b \approx 2\ kW$).

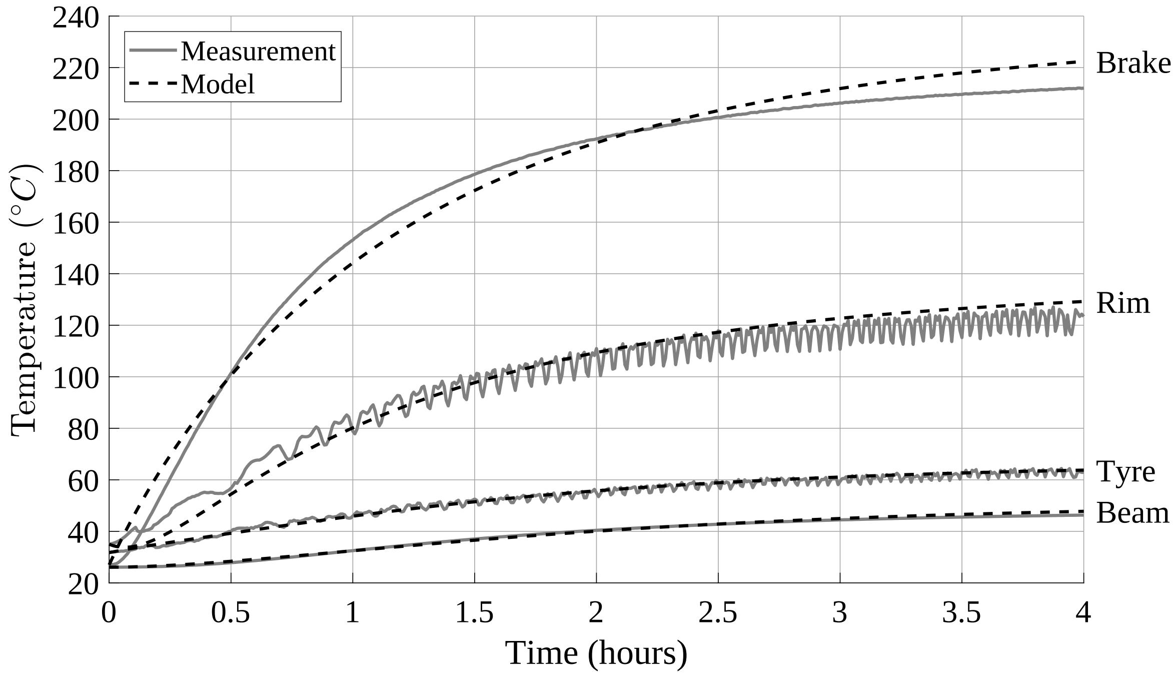

(a) Temperature Response.

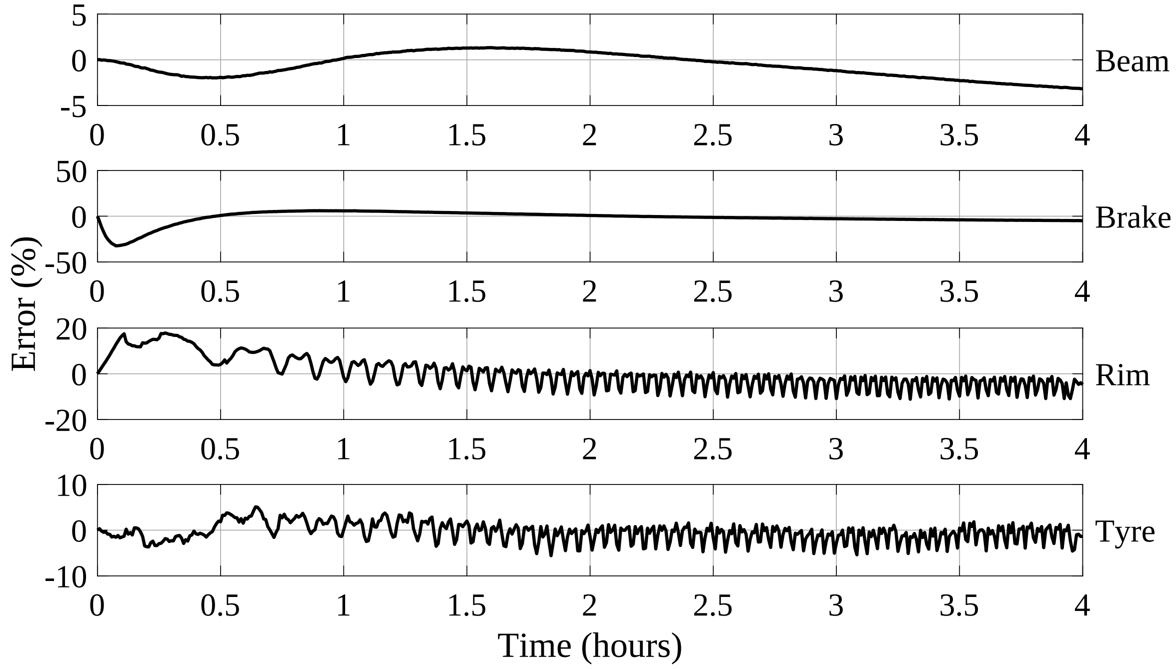

(b) Model Errors.

Figure A.11: Modelling Results (Single, Steel, $P_b \approx 3\ kW$).

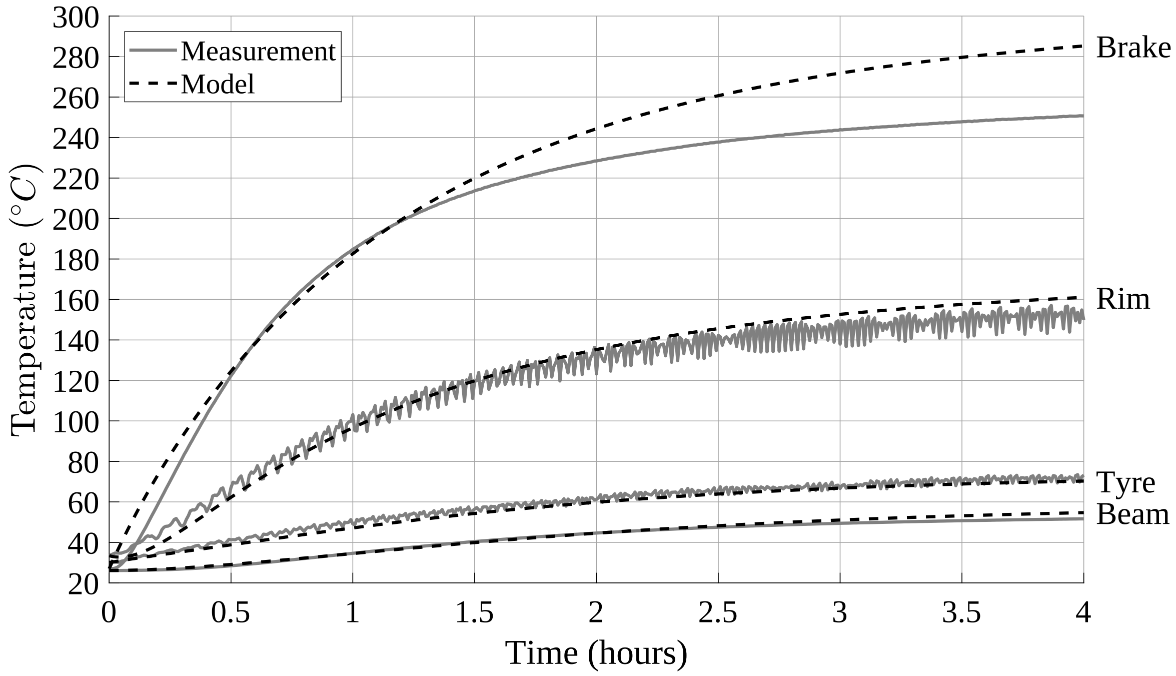

(a) Temperature Response.

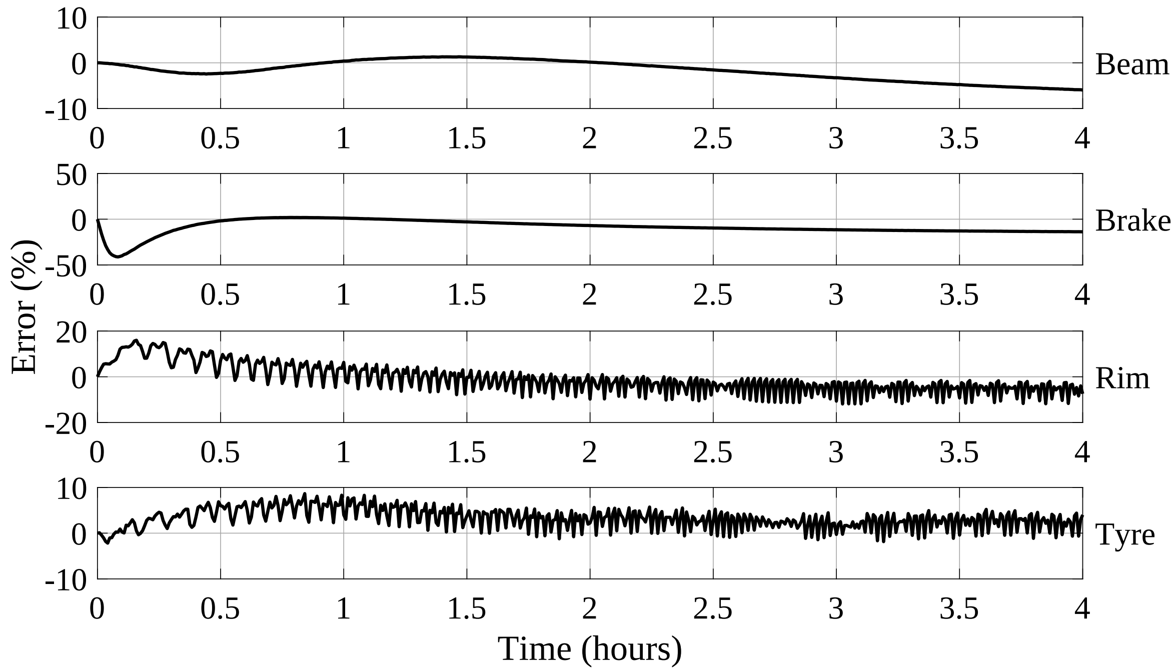

(b) Model Errors.

Figure A.12: Modelling Results (Single, Steel, $P_b \approx 4\ kW$).

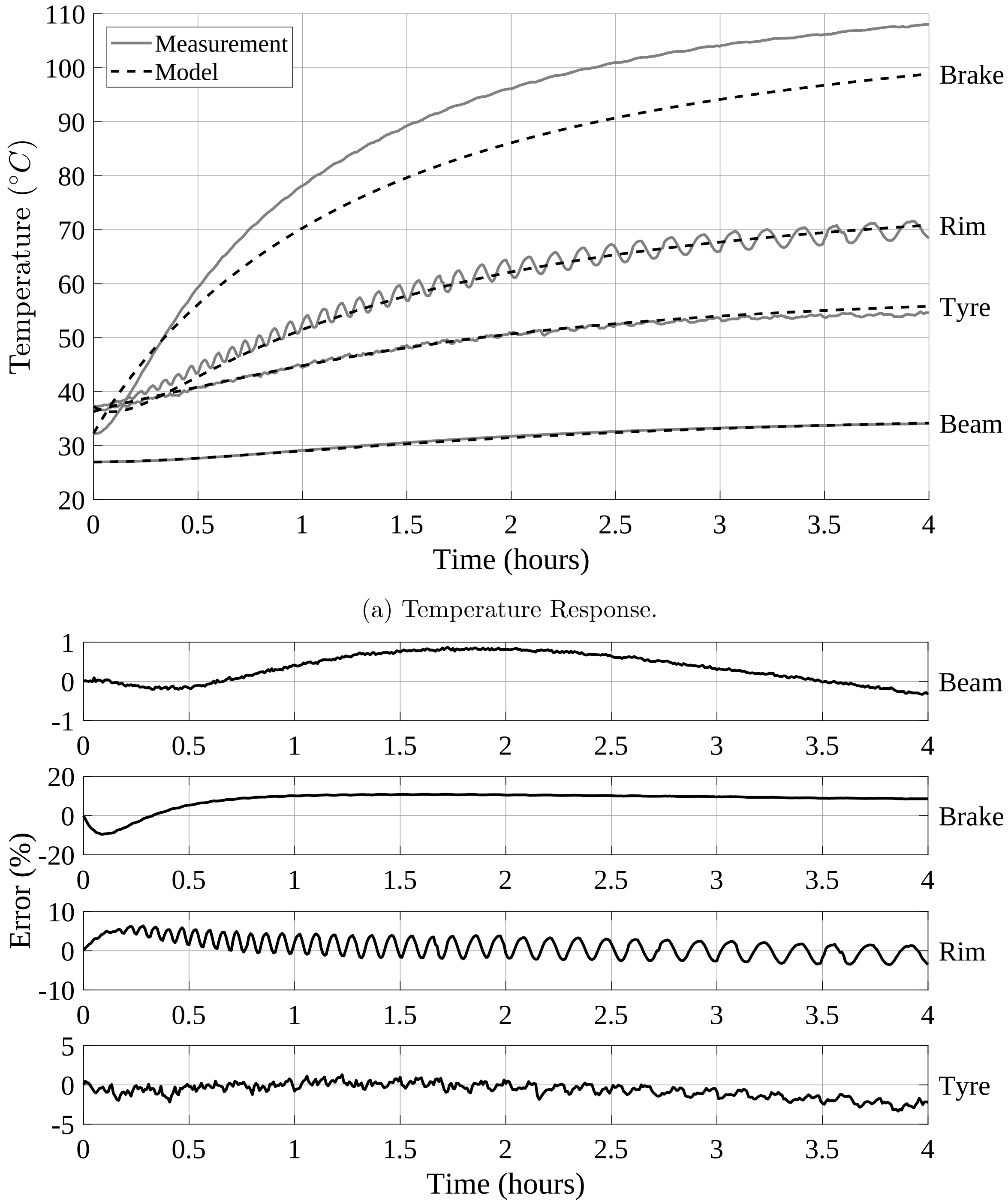

(a) Temperature Response.

(b) Model Errors.

Figure A.13: Modelling Results (Single, Aluminium, $P_b \approx 1\ kW$).

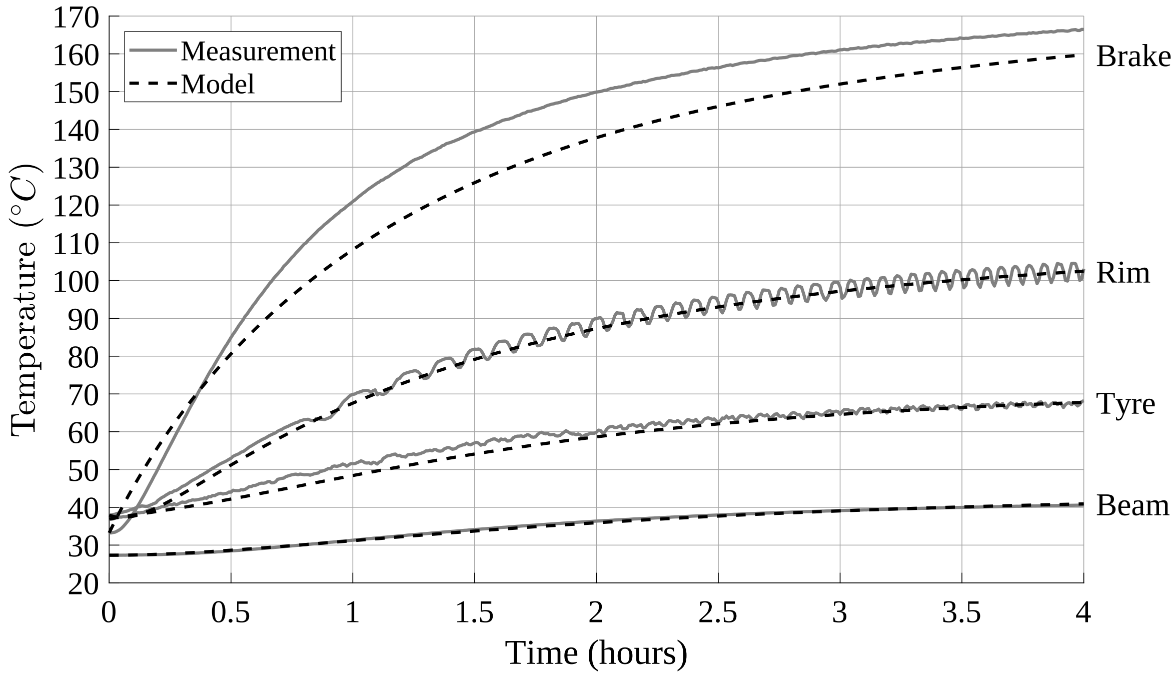

(a) Temperature Response.

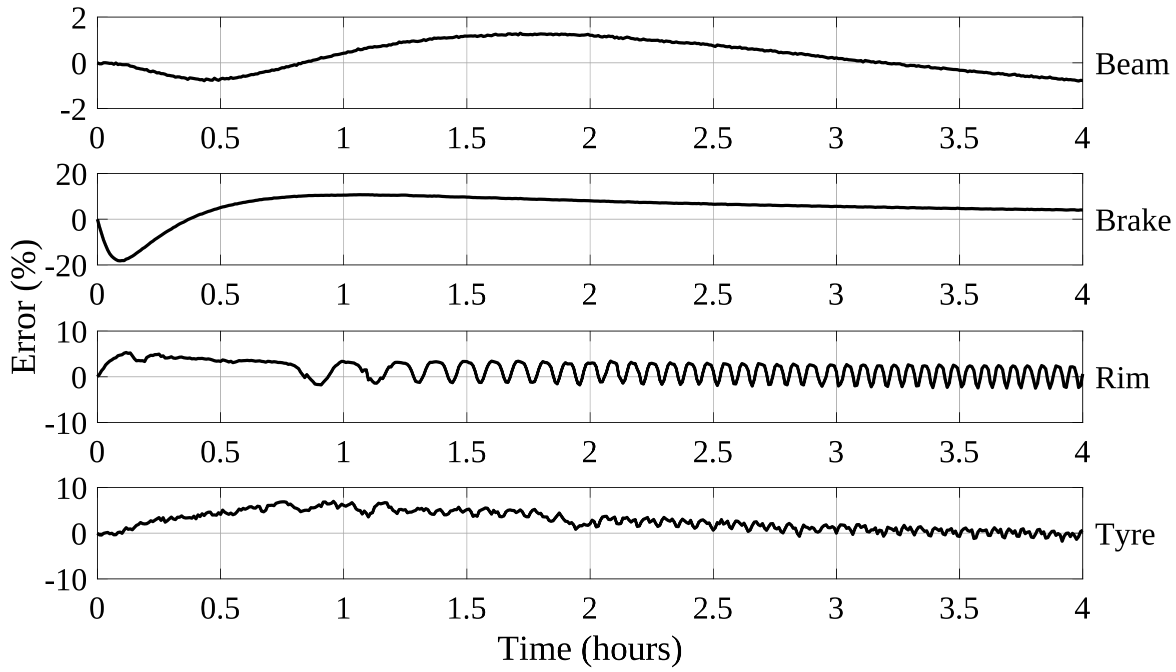

(b) Model Errors.

Figure A.14: Modelling Results (Single, Aluminium, $P_b \approx 2\ kW$).

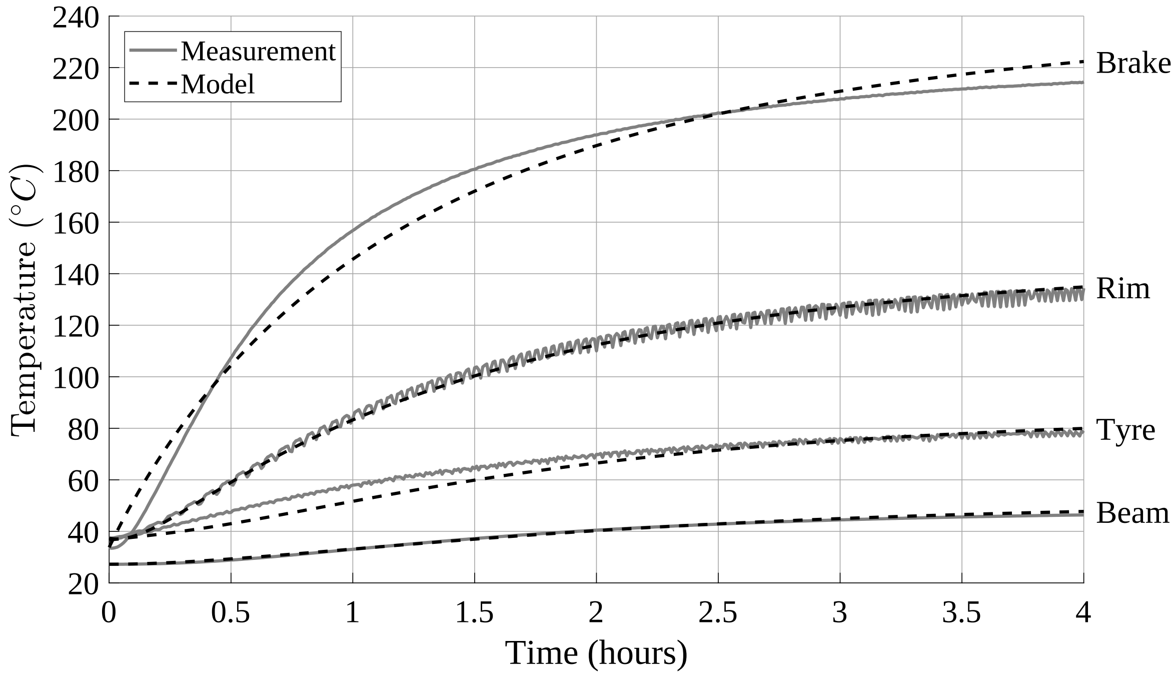

(a) Temperature Response.

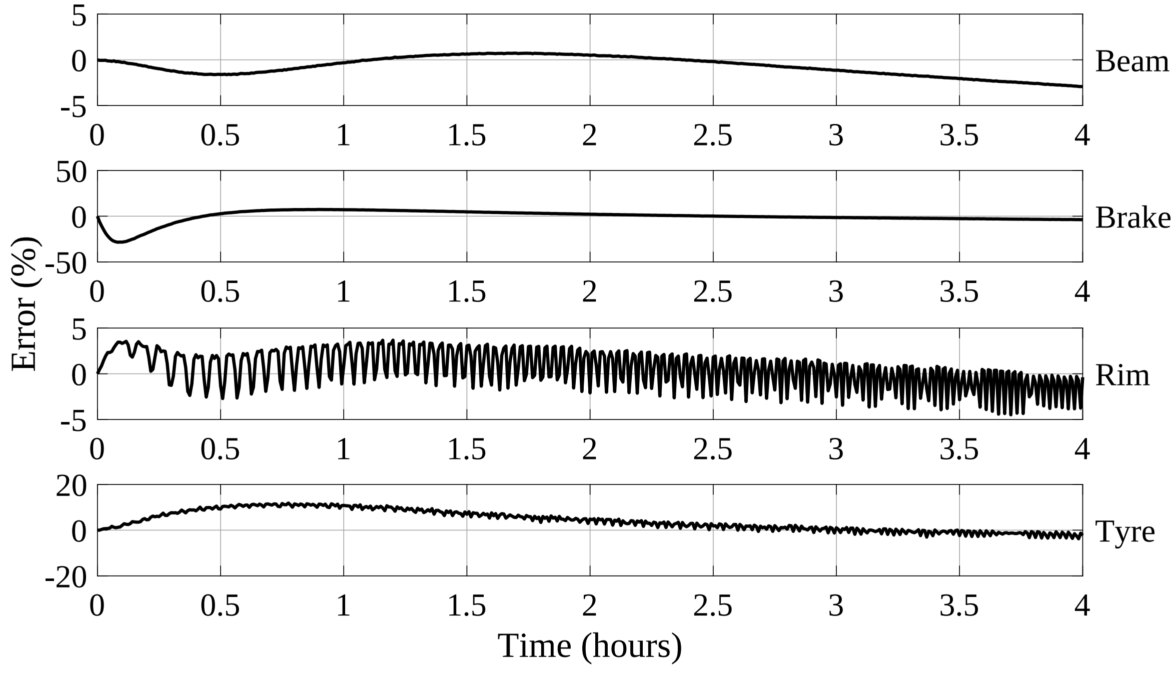

(b) Model Errors.

Figure A.15: Modelling Results (Single, Aluminium, $P_b \approx 3\ kW$).

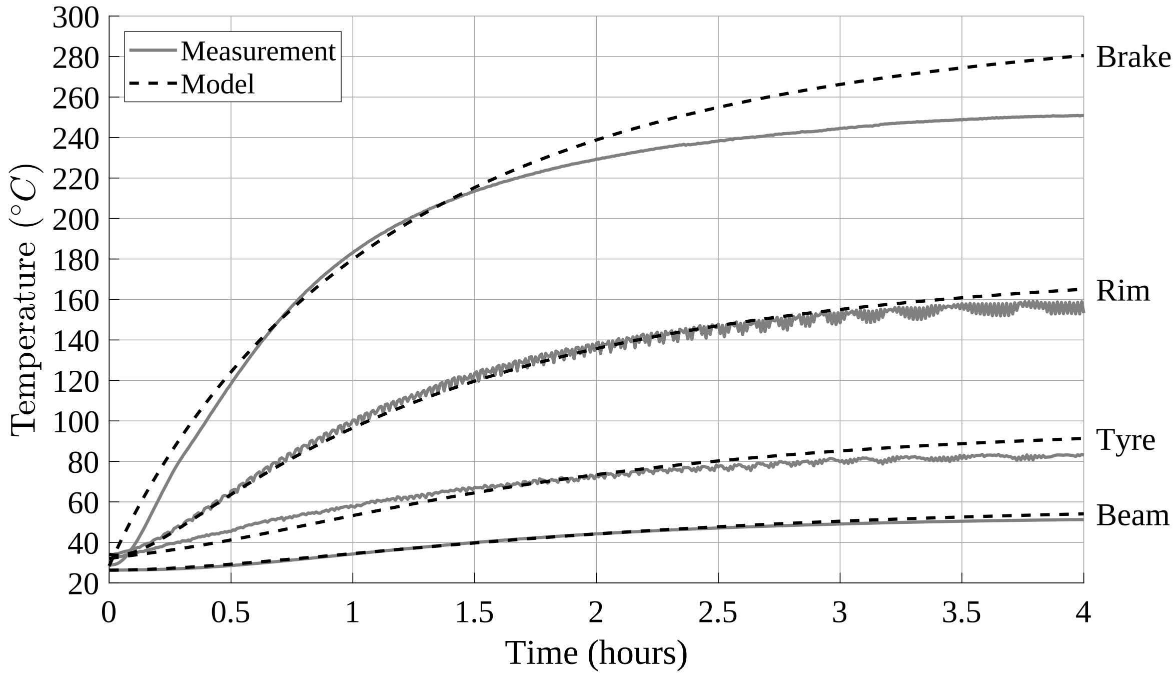

(a) Temperature Response.

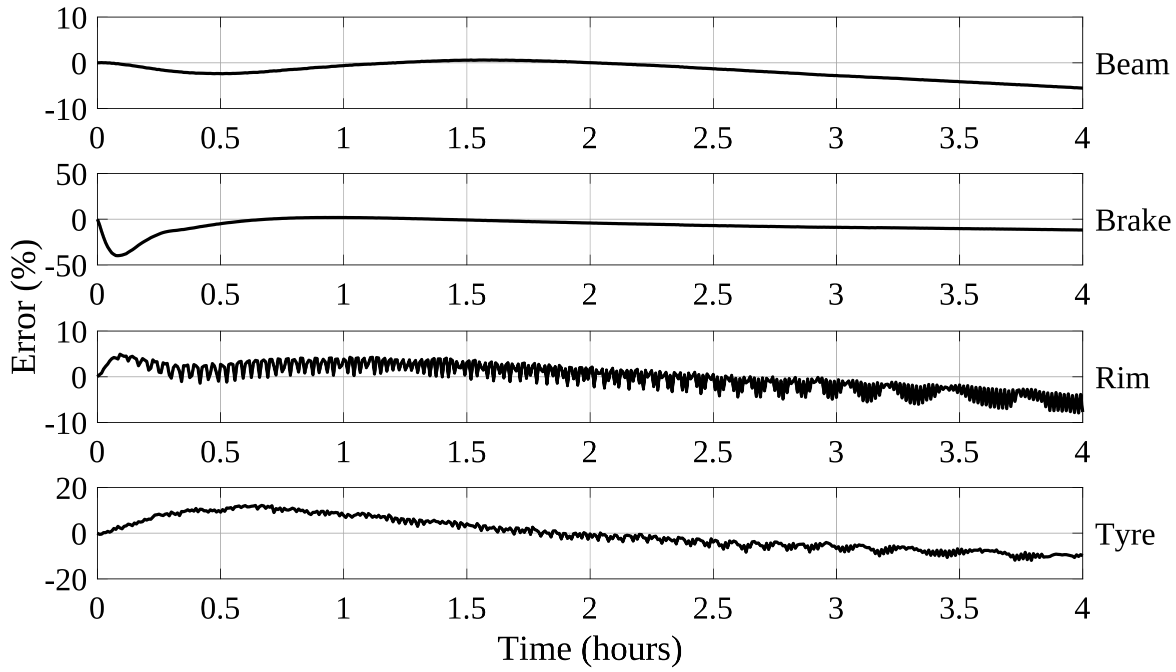

(b) Model Errors.

Figure A.16: Modelling Results (Single, Aluminium, $P_b \approx 4\ kW$).

B Five Degree-of-Freedom Model Evaluation

The temperature at the brake shoe thermocouple, T_s, was taken to be representative of the shoe and drum and neglected the delay of heat propagating from the friction surface, through the thickness of the brake shoe before being measured by the thermocouple. This assumed first-order behaviour resulted in large errors during the initial transient portion of the response. The lumped mass model was modified by adding a virtual sensor which measured the brake temperature at the heat source. The resulting system is described using Equation B.1.

$$\mathbf{B_v} \cdot \dot{\mathbf{T}}_\mathbf{v}(t) + \mathbf{A_v} \cdot \mathbf{T_v}(t) = \mathbf{C_v}(t) \tag{B.1}$$

Where:

$$\mathbf{A_v} = \begin{bmatrix} U_{ba} + U_{sb} & -U_{sb} & 0 & 0 & 0 \\ -U_{sb} & U_{sb} + U_{vs} + U_{sa} & -U_{vs} & 0 & 0 \\ 0 & -U_{vs} & U_{vs} + U_{vr} + U_{va} & -U_{vr} & 0 \\ 0 & 0 & -U_{vr} & U_{vr} + U_{ra} + U_{rt} & -U_{rt} \\ 0 & 0 & 0 & -U_{rt} & U_{rt} + U_{ta} \end{bmatrix}$$

$$\mathbf{B_v} = \begin{bmatrix} (m \cdot C_p)_b & 0 & 0 & 0 & 0 \\ 0 & (m \cdot C_p)_s & 0 & 0 & 0 \\ 0 & 0 & (m \cdot C_p)_v & 0 & 0 \\ 0 & 0 & 0 & (m \cdot C_p)_r & 0 \\ 0 & 0 & 0 & 0 & (m \cdot C_p)_t \end{bmatrix}$$

$$\mathbf{C_v}(t) = \begin{bmatrix} T_\infty \cdot U_{ba} + Q_{friction} \\ T_\infty \cdot U_{sa} \\ T_\infty \cdot U_{va} + P_b(t) \\ T_\infty \cdot U_{ra} \\ T_\infty \cdot U_{ta} + Q_{hysteresis} \end{bmatrix}, \quad \dot{\mathbf{T}}_\mathbf{v}(t) = \begin{bmatrix} \dot{T}_b(t) \\ \dot{T}_s(t) \\ \dot{T}_v(t) \\ \dot{T}_r(t) \\ \dot{T}_t(t) \end{bmatrix}, \quad \mathbf{T_v}(t) = \begin{bmatrix} T_b(t) \\ T_s(t) \\ T_v(t) \\ T_r(t) \\ T_t(t) \end{bmatrix}$$

The power-averaged temperature responses of the four wheels were recalculated and plotted in Figure B.1a - Figure B.4a. Adding a fifth DoF produced the delayed first-order temperature response at the brake shoe which better modelled the dynamics of the measured temperatures. The five DoF model improved the agreement between the model and experimental brake shoe measurements in the initial, transient region. However, the temperatures of this component during this initial transient phase was not critically compared so it was decided to keep with the simpler four DoF model.

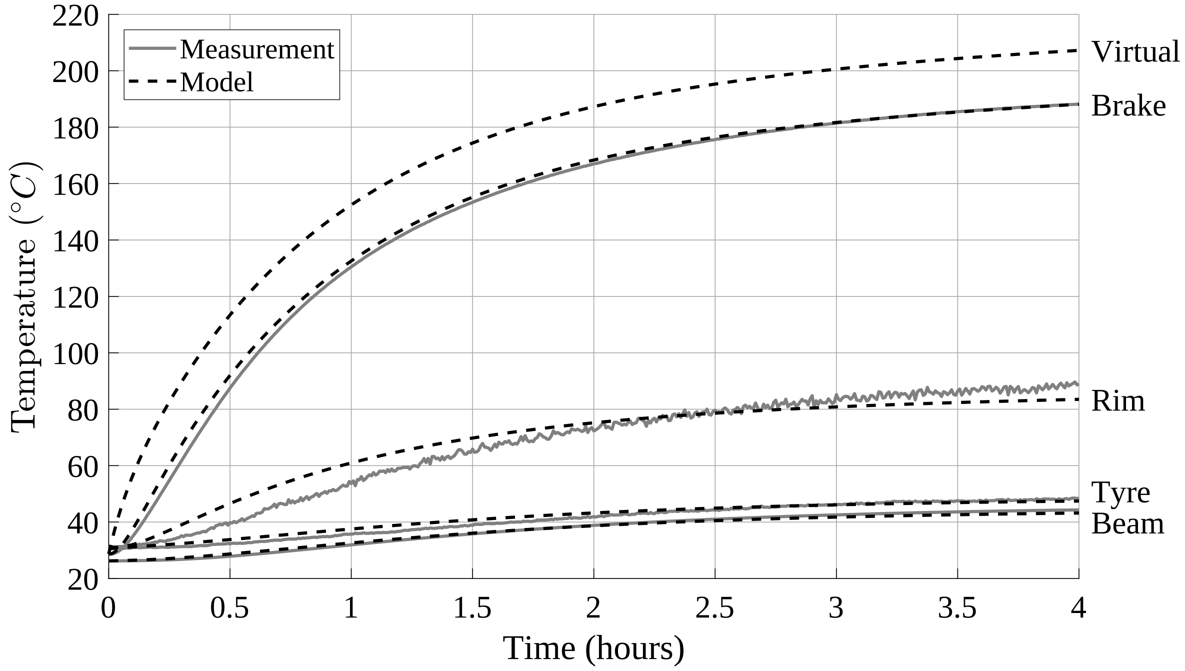

(a) Temperature Response.

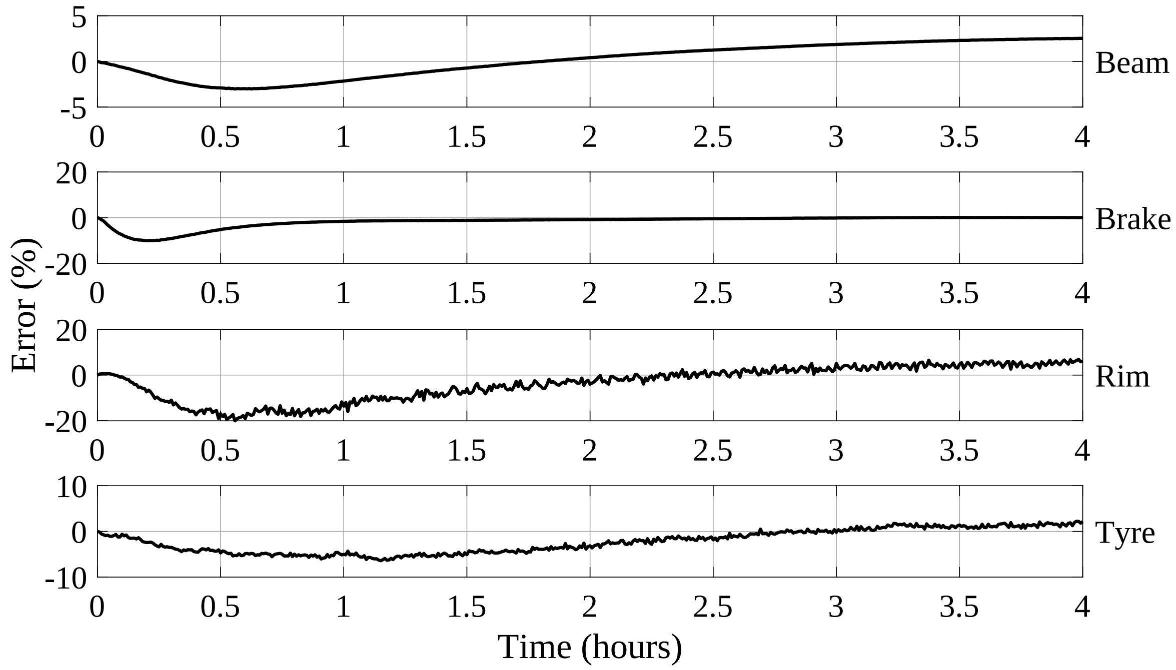

(b) Model Errors.

Figure B.1: Five DoF Modelling Results (Averaged, Dual, Steel, $P_b \approx 2.5\ kW$).

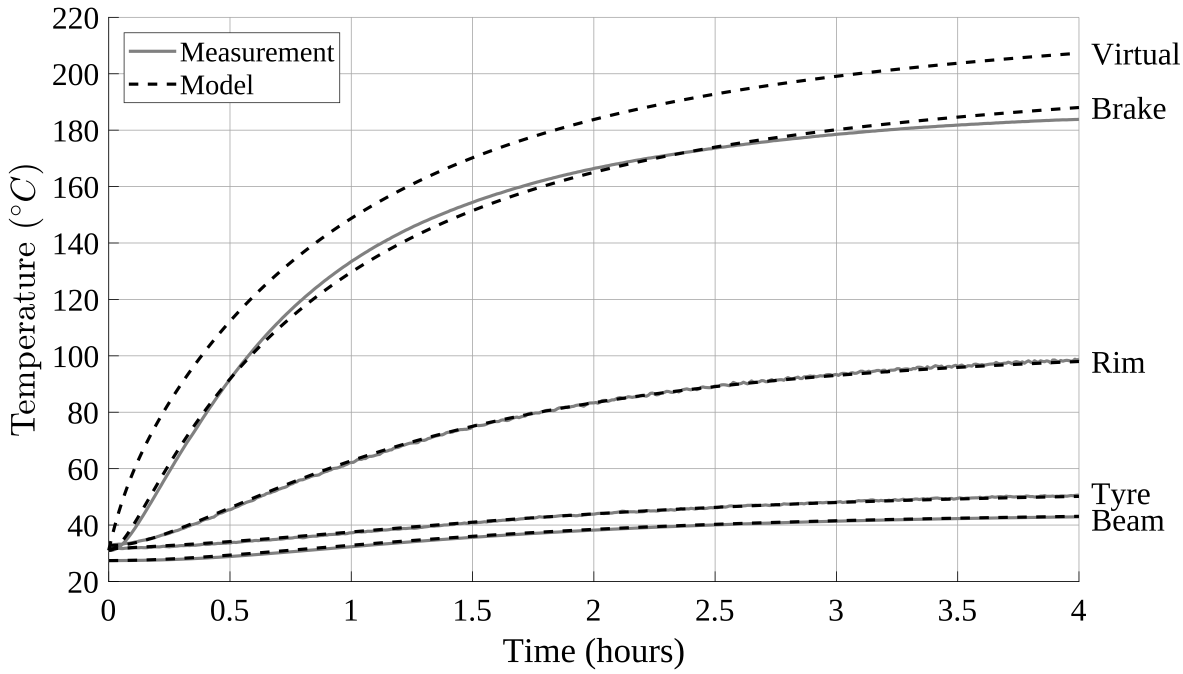

(a) Temperature Response.

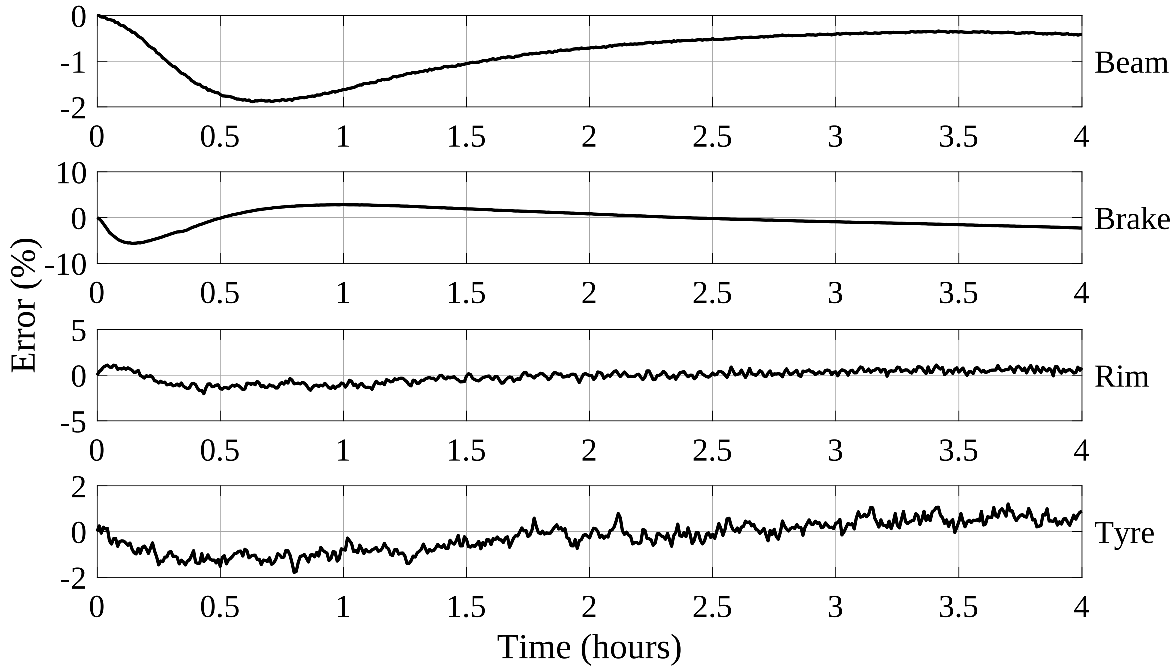

(b) Model Errors.

Figure B.2: Five DoF Modelling Results (Averaged, Dual, Aluminium, $P_b \approx 2.5\ kW$).

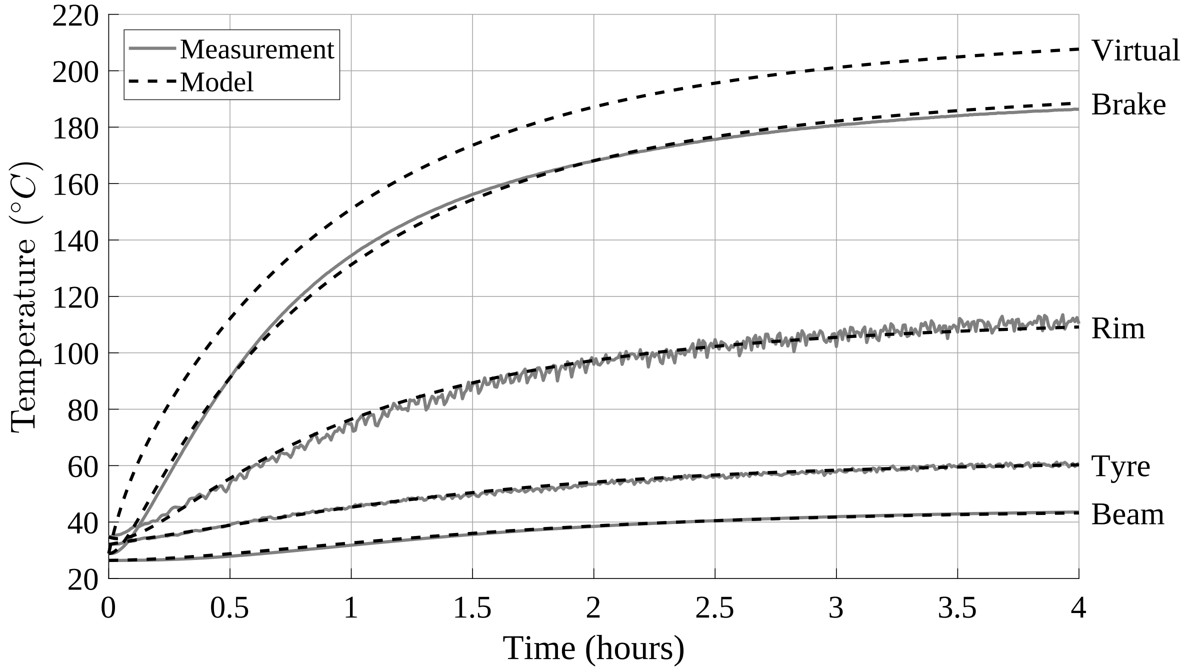

(a) Temperature Response.

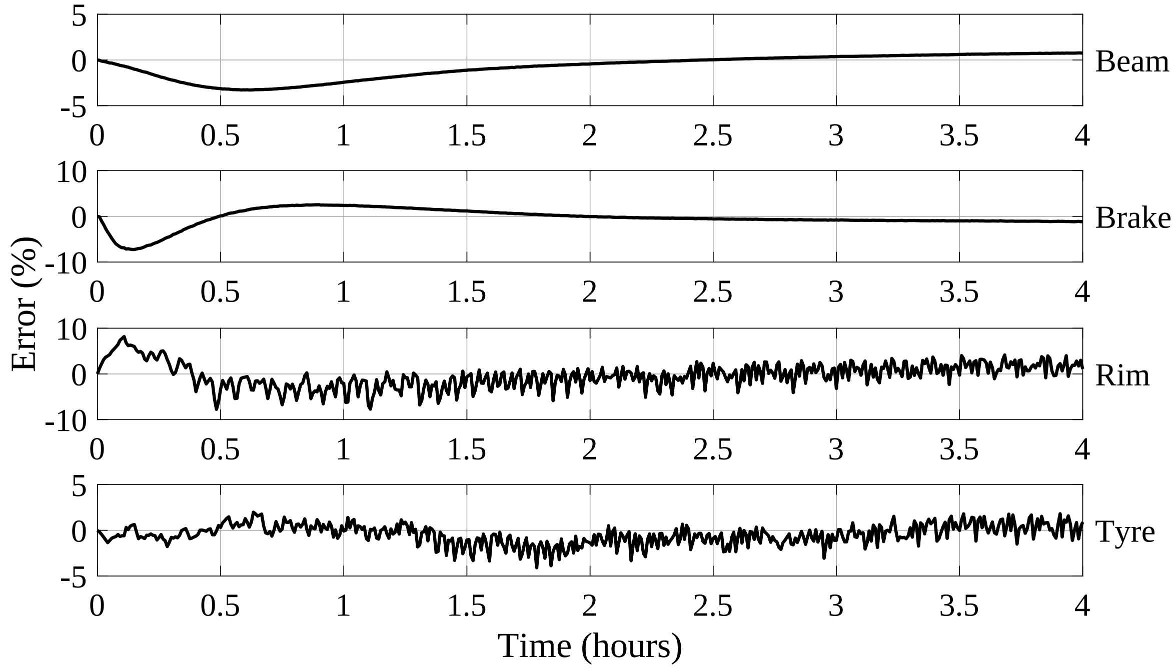

(b) Model Errors.

Figure B.3: Five DoF Modelling Results (Averaged, Single, Steel, $P_b \approx 2.5\ kW$).

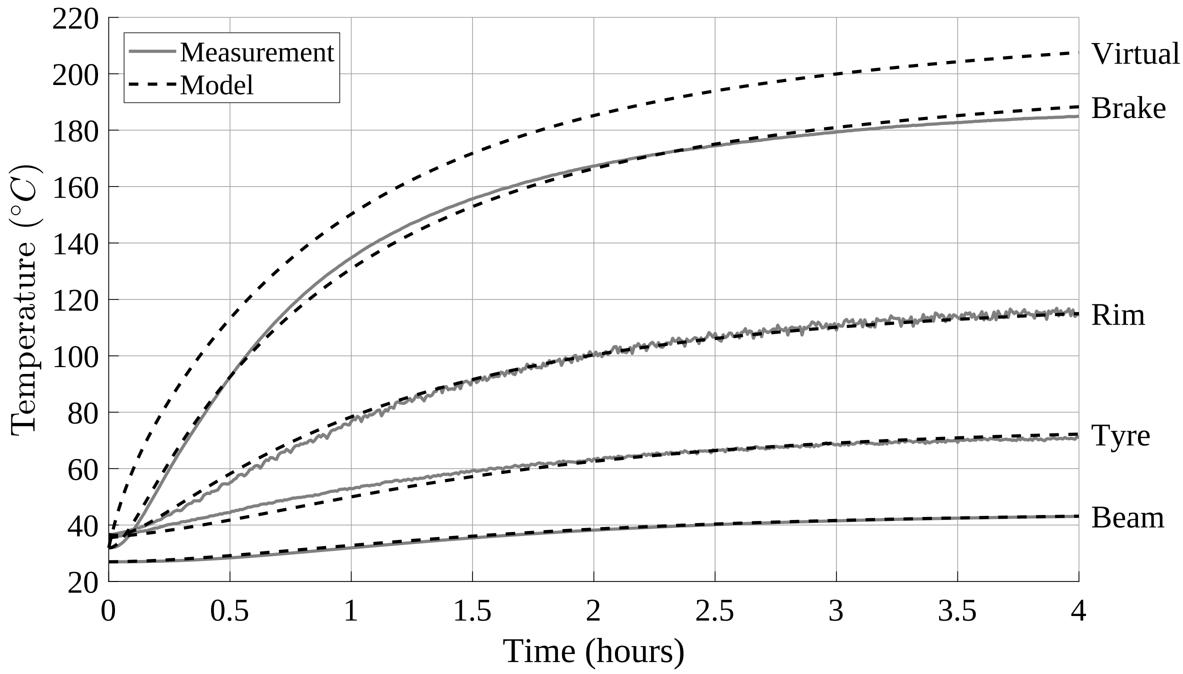

(a) Temperature Response.

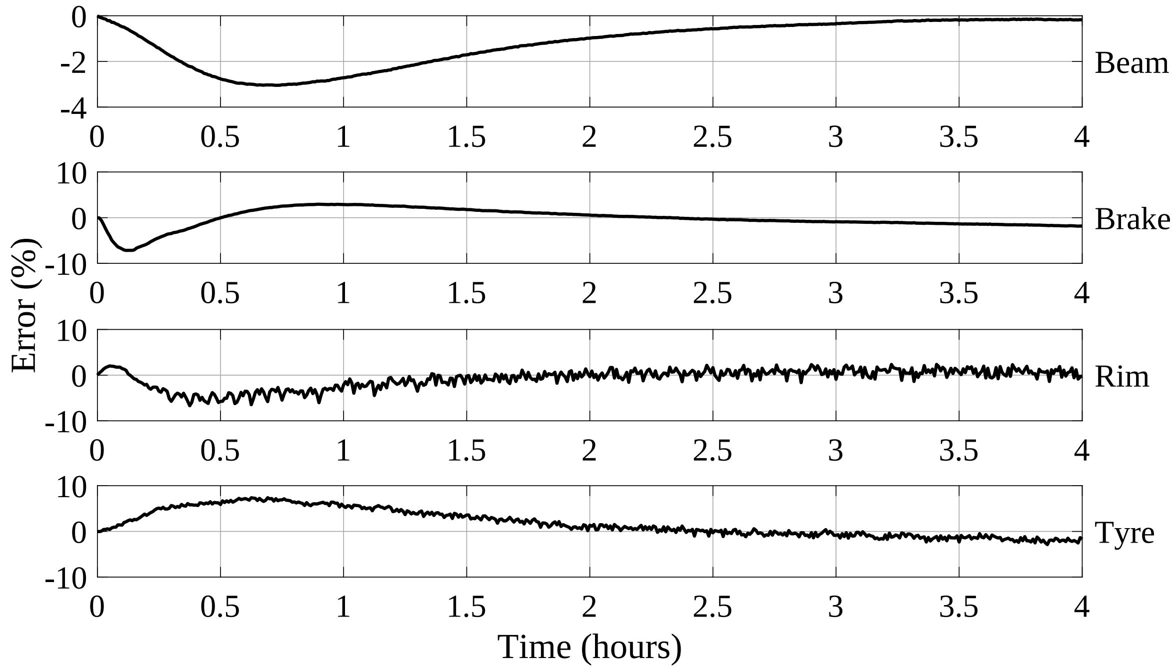

(b) Model Errors.

Figure B.4: Five DoF Modelling Results (Averaged, Single, Aluminium, $P_b \approx 2.5\ kW$).

C Maximum Tyre Temperature Modelling

Moderate average tyre temperatures can be accompanied by extremely high maximum tyre temperatures when the wheel is subjected to alpine braking. It is therefore important to model maximum tyre temperature as a function of braking power to compare the likelihood of blowout for different wheel configurations. The maximum tyre temperature was defined as the average temperature in region A_1 in Figure 3.10b and plotted versus time for each test in Figure C.1 to Figure C.4.

The maximum tyre temperature response, $\Delta T(t)$ $(°C)$, to a braking input, P_b (W), exhibits the characteristics of an overdamped, second-order system. For zero initial conditions, i.e. $\Delta T(0) = 0$, $\Delta \dot{T}(0) = 0$, such a system can be modelled using Equation C.1.

$$\Delta T(t) = \frac{P_b}{K}\left(\frac{S_2}{S_1 - S_2}e^{S_1 t} - \frac{S_1}{S_1 - S_2}e^{S_2 t} + 1\right) \tag{C.1}$$

Where $S_1 = -{}^1/_{\tau_1}$ and $S_2 = -{}^1/_{\tau_2}$. τ_1 and τ_2 have units (s) and are known as the time constants of the system. These values determine the rate at which transient effects decay. The stiffness of the system, K $({}^W/_{°C})$, relates the magnitudes of $\Delta T(t)$ $(°C)$ and P_b (W). MATLAB was used to fit Equation C.1 to each temperature curve and averaged for each wheel to give the model parameters listed in Table C.1.

Table C.1: Maximum Tyre Temperature Change Model Parameters.

Parameter	Unit	Dual, Steel	Dual, Aluminium	Single, Steel	Single, Aluminium
τ_1	S	3297	3120	5140	4582
τ_1	S	3297	3120	211.9	257.6
K	${}^W/_{°C}$	78.49	69.58	43.86	37.89
$RMSE$	$°C$	0.3984	0.05064	1.294	0.9808
$Adjusted\ R^2$	–	0.9985	1.000	0.9932	0.9972

There are no constant terms in Equation C.1 since the output is defined as temperature increase instead of absolute temperature. This ensures additivity and homogeneity of the system. The maximum tyre temperature increases were therefore averaged and normalised per unit braking power to give the curves in Figure 6.8. Maximum tyre temperature was calculated by multiplying the normalised curves by the magnitude of

P_b and adding the initial temperature. This is accurate up to approximately 135 $°C$ which is the range in which this model has been validated.

The maximum tyre temperature increases for $P_b \approx 1\ kW - 4\ kW$ were calculated for each wheel and plotted with experimental data in Figure C.1 to Figure C.4. The percentage *RMSE* and maximum percentage error for each curve was calculated and listed in Table C.2 and Table C.3 respectively. The highest *RMSE* and maximum percentage errors are 5.1% and 12% respectively for the single, steel wheel under $P_b \approx 3\ kW$. This indicates that the averaged parameters accurately describe the temperature responses across a range of braking powers.

Table C.2: Maximum Tyre Temperature Model Percentage $RMSE$.

P_b (kW)	$RMSE$, (%)				
	Dual, Steel	Dual, Aluminium	Single, Steel	Single, Aluminium	Maximum
1	0.89	1.6	4.2	2.9	4.2
2	3.5	1.5	4.9	2.4	4.9
3	1.8	3.5	5.1	2.4	5.1
4	4.1	2.4	4.4	3.3	4.4
Maximum	4.1	3.5	5.1	3.3	5.1

Table C.3: Maximum Tyre Temperature Model Maximum Percentage Errors.

P_b (kW)	Maximum Error (%)				
	Dual, Steel	Dual, Aluminium	Single, Steel	Single, Aluminium	Maximum
1	3.2	4.2	9.6	5.9	9.6
2	7.6	4.1	9.2	5.0	9.2
3	4.3	6.9	12	5.2	12
4	7.9	6.1	11	8.9	11
Maximum	7.9	6.9	12	8.9	12

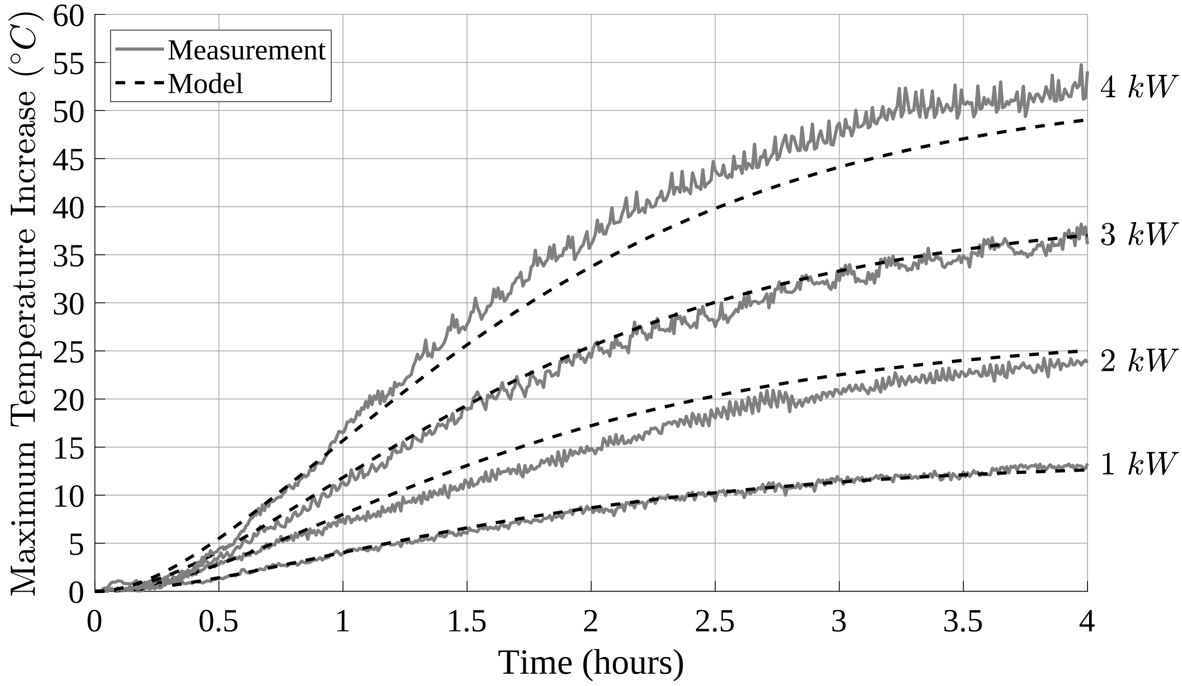

Figure C.1: Maximum Tyre Temperature Increase (Dual, Steel, $\overline{T}_i = 30\ °C$).

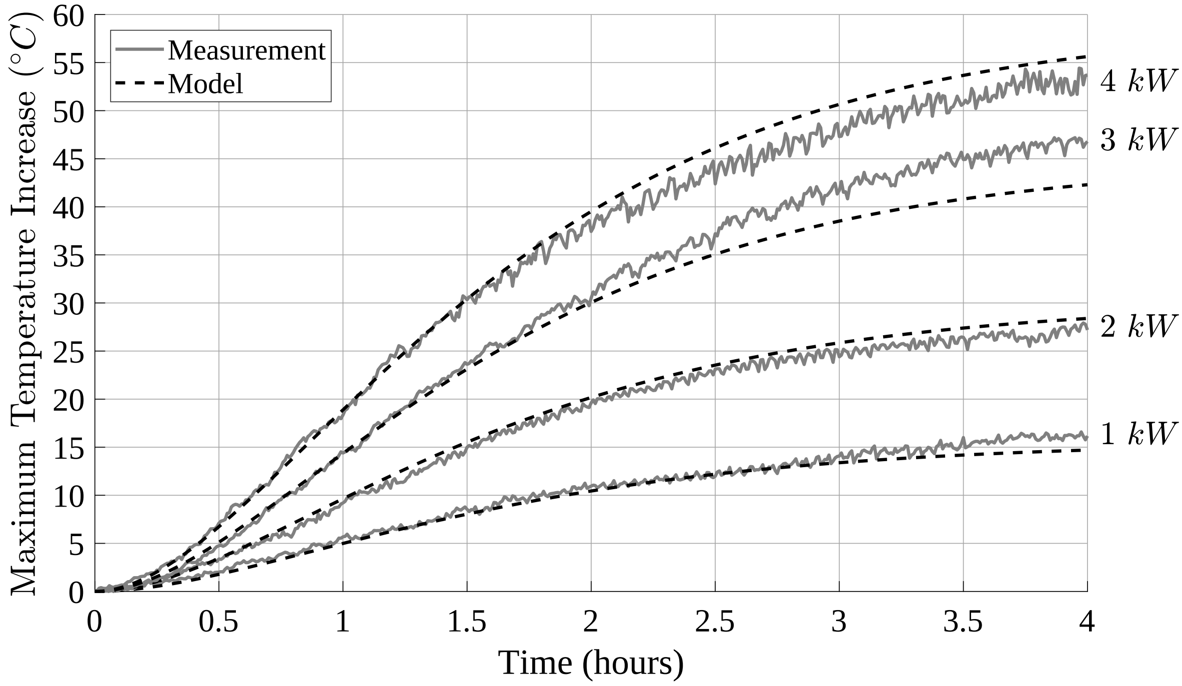

Figure C.2: Maximum Tyre Temperature Increase (Dual, Aluminium, $\overline{T}_i = 31\ °C$).

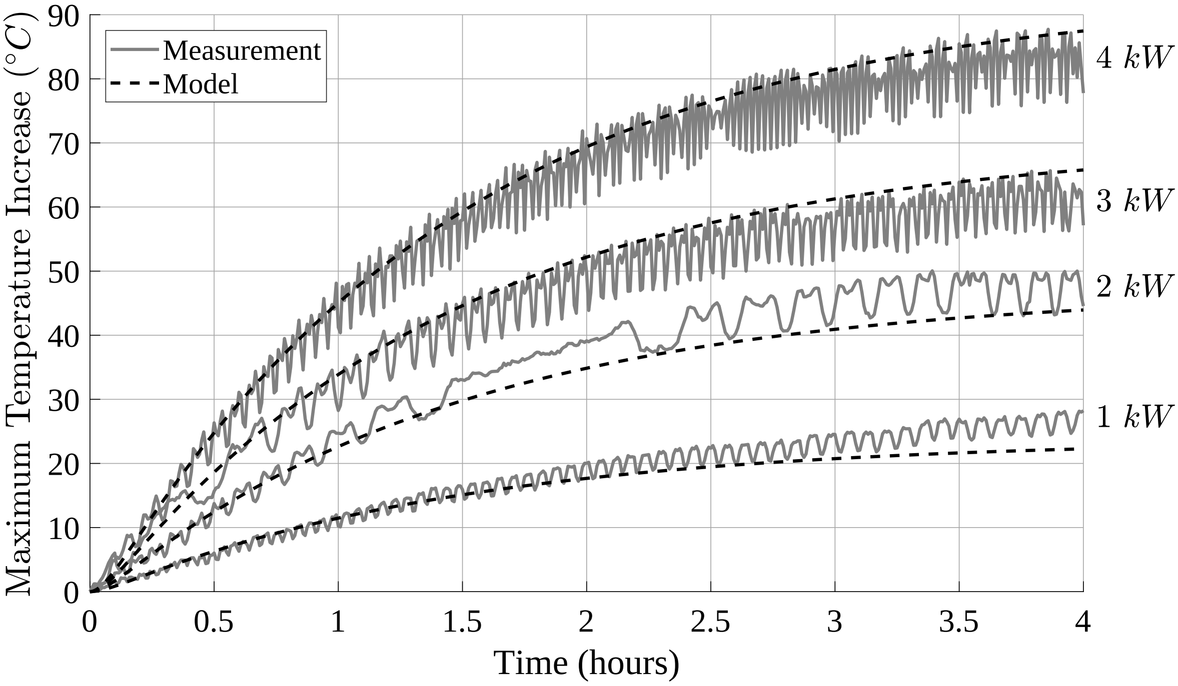

Figure C.3: Maximum Tyre Temperature Increase (Single, Steel, $\overline{T}_i = 33\ °C$).

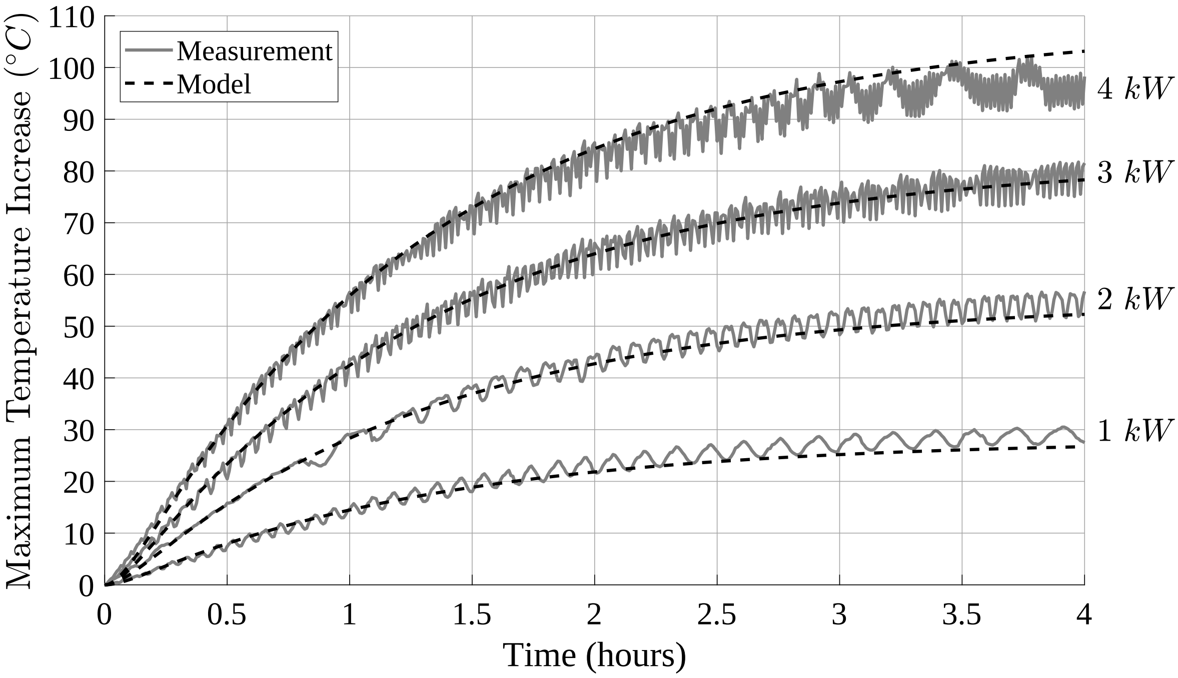

Figure C.4: Maximum Tyre Temperature Increase (Single, Aluminium, $\overline{T}_i = 35\ °C$).